1993

High-spin [gamma]-ray spectroscopy in 198Bi, superdeformation in 191Au, and multi-photon resonances in low energy e+e- scattering

Duc Ta Vo
Iowa State University

INFORMATION TO USERS

This manuscript has been reproduced from the microfilm master. UMI films the text directly from the original or copy submitted. Thus, some thesis and dissertation copies are in typewriter face, while others may be from any type of computer printer.

The quality of this reproduction is dependent upon the quality of the copy submitted. Broken or indistinct print, colored or poor quality illustrations and photographs, print bleedthrough, substandard margins, and improper alignment can adversely affect reproduction.

In the unlikely event that the author did not send UMI a complete manuscript and there are missing pages, these will be noted. Also, if unauthorized copyright material had to be removed, a note will indicate the deletion.

Oversize materials (e.g., maps, drawings, charts) are reproduced by sectioning the original, beginning at the upper left-hand corner and continuing from left to right in equal sections with small overlaps. Each original is also photographed in one exposure and is included in reduced form at the back of the book.

Photographs included in the original manuscript have been reproduced xerographically in this copy. Higher quality 6" x 9" black and white photographic prints are available for any photographs or illustrations appearing in this copy for an additional charge. Contact UMI directly to order.

U·M·I

University Microfilms International
A Bell & Howell Information Company
300 North Zeeb Road, Ann Arbor, MI 48106-1346 USA
313/761-4700 800/521-0600

Order Number 9414031

High-spin γ-ray spectroscopy in ^{198}Bi, superdeformation in ^{191}Au, and multi-photon resonances in low energy e^+e^- scattering

Vo, Duc Ta, Ph.D.

Iowa State University, 1993

U·M·I
300 N. Zeeb Rd.
Ann Arbor, MI 48106

High-spin γ-ray spectroscopy in ^{198}Bi, superdeformation in ^{191}Au, and multi-photon resonances in low energy e^+e^- scattering

by

Duc Ta Vo

A Dissertation Submitted to the

Graduate Faculty in Partial Fulfillment of the

Requirements for the Degree of

DOCTOR OF PHILOSOPHY

Department: Physics and Astronomy
Major: Nuclear Physics

Approved:

Signature was redacted for privacy.

In Charge of Major Work

Signature was redacted for privacy.

For the Major Department

Signature was redacted for privacy.

For the Graduate College

Members of the Committee:

Signature was redacted for privacy.

Iowa State University
Ames, Iowa
1993

TABLE OF CONTENTS

LIST OF TABLES

LIST OF FIGURES

CHAPTER 1. INTRODUCTION

There are many reasons for studying the physics involving the nuclear forces. One reason for these studies is to determine the properties of nuclei. Of course, no single experiment can provide all the answers about a nucleus. Experiments of the type reported here are meant to provide information about the level properties, specifically the energies and intensities of γ transitions connecting these levels, and to study the nuclear structures of the levels of both low and high spin of nuclei in the mass A $\approx$ 190 region.

Another reason for studying nuclear forces is to investigate and to explain one of the phenomena observed in collisions of heavy ions such as Uranium and Thorium. When U and Th collided at center-of-mass energy near the Coulomb barrier, sharp peaks in coincident e^+e^- pair spectra were observed. Many theories and experiments have been constructed to explain this phenomenon, which is believed to come from a neutral object interacting with a third body. The goal of the research reported here on this phenomenon is to confirm (or set the upper limits for) the existence of such neutral low-mass particles.

1.1 Previous studies of ^{198}Bi

Very little experimental work has been done on the lighter mass odd-odd Bi nuclei, especially at high spin. Most of the previous studies on odd-odd Bi nuclei with mass 202 or lower were from β^+ decay of Po nuclei, α decay of At nuclei, or low-spin reactions. The reason for this is there are only a few feasible nuclear reactions that can create light neutron-deficient Bi isotopes. Also, at high spin, the formation of light Bi isotopes is dwarfed by the competing fission process which makes the analysis of the Bi nuclei extremely difficult and, at the same time, adds to the neutron damage of the γ-ray detectors.

Prior to this work, almost nothing was known about ^{198}Bi. From the reaction ^{191}Ir(^{12}C,5n) at bombardment energy E = 81 MeV and ^{181}Ta(^{22}Ne,5n) at E = 120 MeV, Hagemann *et al* [1] found one transition from the 248.5(5)-keV level with $J^\pi=10^-$ to the 7^+ ground level with the half-life of $T_{1/2}$=7.7(5) s. The spins of these states were determined from the analogy with similar levels in ^{200}Bi [1]. One more known state in the level scheme is the 5^+ state at 95(3) keV, which decays by an E2 transition to the 7^+ ground state. This 5^+ level was observed in α decay studies [2, 3, 4] and is not yet satisfactorily confirmed.

Bismuth nuclei have 83 protons, thus it might be naively expected that the low-energy properties of odd-odd Bi nuclei could be described as a single proton (outside the closed shell of 82 protons) coupled to the odd neutron between the N=82 and N=126 closed shells. The analysis might be done in a manner analogous to that for the known levels of ^{200}Bi. For high-energy and high-spin states of odd-odd nuclei, the prediction of their level structures is quite difficult. One way to analyse their structures is to compare the high-spin states in odd-odd Bi nuclei to those known

high-spin states in neighboring nuclei (Pb, Tl, Hg...). Such an analysis is done in this work.

1.2 Bands in ^{191}Au

The search for new superdeformed (SD) bands is important in many respects. Perhaps most obvious, SD bands are a critical test of the ability to predict nuclear properties. A SD nucleus is a nucleus that has been greatly deformed. It has the shape of a prolate ellipsoid with the major axis almost twice the length of the two minor axes. Multiple bands in a given nucleus could give information about the orbitals involved at large deformations, which may be quite different than those in normally deformed nuclei. Superdeformed bands are often identical to others in neighboring nuclei and new examples often provide clues that will help to understand this puzzling phenomenon. "Identical" SD bands, usually in different nuclei, refer to rotational bands that have not only the same moment of inertia, but also identical or "equivalent" transition energies. The "equivalent" transition energies correspond to half-points or quarter-points between two consecutive transition energies in the identical bands. Since each transition carries two units of angular momentum, this means that any additional single-particle contribution to the angular momentum must be half-integer or integer. This is not expected in the "traditional" models and may lead to the development of new concepts and reveal new symmetries.

In the mass A = 190 region, at the time of this investigation, superdeformed nuclei were known only for the Hg, Tl and Pb isotopes[5], although they are predicted[6, 7] for both higher and lower atomic numbers, Z. In the SD candidate nuclei with Z > 82, it is very difficult to find new superdeformed bands because of higher fission

competition. Prior to this work, no SD bands had been found in this region for Z $<$ 80. These relatively neutron-rich nuclei can only be populated at high angular momentum with very light neutron-rich projectiles. The first SD band found in a gold (Z = 79) nucleus, ^{191}Au is reported in this work. This SD band is the first experimental evidence that this region of superdeformation extends below Z = 80. In this odd-Z nucleus, it is found that the SD band is "identical" to quarter-point energies of the SD band in "doubly magic" ^{192}Hg and to an excited band in ^{191}Hg, an odd-neutron nucleus. This is different from the behavior of the Tl nuclei (the other odd-Z SD nuclei in this region), where the extra odd proton does not produce a SD band identical to that in ^{192}Hg.

1.3 e^+e^- Resonances

Sharp peaks have been observed in coincident e^+e^- pair spectra obtained by the EPOS [8, 9] and, independently by the ORANGE [10] experimental groups, both at Gesellschaft für Schwerionenforschung (GSI). These peaks are observed when two heavy ions such as U and Th collide at center-of-mass (CM) energies near the Coulomb barrier and when a large-angle scattering of the two heavy ions is detected. Under such conditions, an effective charge of greater than 160 might be obtained for a short time period localized within a radius of about 20 fm from the CM. These sharp peaks are suggestive of a long-lived neutral object (system or particle created in the collision process) that decays to an e^+e^- pair. Both experimental groups at GSI have reported that there is some evidence that the e^+e^- decays may occur from a neutral object interacting with a third body. The e^+e^- peaks observed at GSI have provided a major theoretical challenge [11].

Motivated by these results, numerous searches for resonance phenomena in e^+e^- (Bhabha) scattering, $e^+e^- \rightarrow X \rightarrow e^+e^-$, have been performed and the results are conflicting. Some experiments [12, 13, 14, 15] claim to see a weak resonance while other experiments [16, 17, 18, 19, 20, 21] claim to exclude these signals. Since the observed signals are, at best, rather weak, present evidence for e^+e^- resonances produced directly in Bhabha scattering is inconclusive. It is interesting to note that the experiments claiming positive results generally used a thick high-Z target (which would provide a large electric field near the nucleus) and/or wide angular acceptance detectors (which would make them more sensitive to processes that deviate from strict two-body kinematics). The experiment was designed to include both of these characteristics, a thick high-Z target and wide angular acceptance detectors.

Additional searches have been conducted for evidence of resonances in the processes $e^+e^- \rightarrow X \rightarrow 2\gamma$ and $e^+e^- \rightarrow X \rightarrow 3\gamma$ by other investigators with little success. In these experiments, the e^- targets are bombarded with e^+ from a β^+ emitter or accelerator. The reported 2γ searches are negative [22, 23, 24, 25, 26, 27, 28]. However, a recent 3γ search by Skalsey and Kolata [29] found an energy-sum peak at 1455 keV whose area is 2.9σ above background, and a 2.2σ energy-sum peak at 1648 keV. (The quoted energy is the sum of the energies of 3 γ rays in triple coincidence, and σ is the normal standard deviation.) In their experiment, a Be foil target is bombarded by a collimated beam of e^+ from a 100 μCi ^{68}Ge/^{68}Ga β^+ source. An array of five detectors coplanar with the source was used to detect the γ rays emitted from the Be target. Their total counting time was 222 hours. They concluded from a Dalitz analysis of the 1022-keV and 1455-keV peaks that momentum is conserved in the 3γ decay of the 1022-keV peak from orthopositronium (as expected) but not

in the 3γ decay of the 1455-keV peak. This finding was consistent with an interpretation of the 1455-keV peak as either a random fluctuation in a widely distributed Dalitz plot or a decaying particle coupled to a massive partner such as the Be target [29]. Skalsey and Kolata thus concluded that there is no evidence for a new stopped unbound neutral particle in their data set.

This accumulated set of puzzling and seemingly conflicting experimental results was a motivation in the search for resonances in coincident multi-photon final states from e^+e^- scattering in the vicinity of strong fields. The experiment was also motivated by recent calculations [30] of states in a proposed neutral e^+e^- compound called photonium. (For brevity, in the rest of this work, the terms photonium and X will be used interchangeably.) The calculations were carried out in the $J^\pi=0^+$, L=1, S=1 channel using relativistic two-body wave equations that are based on QED. Some of these calculated states lie near the energies of peaks observed in the GSI experiments. The free-space widths of these states are zero in the calculations, but neglected QED processes may be expected to add a finite contribution. Other experiments [16, 21] indicated that if these states exist their free-space decay widths are exceedingly small. The current upper limits of the partial width for $e^+e^- \rightarrow X \rightarrow e^+e^-$ are 1.3×10^{-2} meV for spin-0 and 6.5×10^{-3} meV for spin-1 resonances at 1.83 MeV [21]. For the process $e^+e^- \rightarrow X \rightarrow n\gamma$, the upper limits are 2.7 meV for spin-0 [27] and 5 meV for spin-1 resonances at 1.83 MeV [28], corresponding to half-lives of 2.4×10^{-13} s and 1.3×10^{-13} s, respectively. A scenario that has not been excluded experimentally is that the e^+e^- peaks arise from the production and stimulated decay of photonium in high fields. Production rates for photonium from e^+e^- collisions in high-Z target materials have been studied [31, 32] theoretically.

CHAPTER 2. ELECTRONICS

All the experiments reported in this work were done using the High Energy-Resolution Array (HERA) facility at the Lawrence Berkeley Laboratory (LBL). For the two online experiments that studied ^{198}Bi and ^{191}Au nuclei produced in the collisions of ions and targets, the ion beams were provided by the 88-Inch Cyclotron at LBL. The cyclotron could produce various ion beams at various energies and intensities. The capability of the 88-Inch Cyclotron includes such beams as a proton beam with an energy up to 50 MeV/u and an intensity of 100 μA, a ^{129}Xe beam with an energy up to 6 MeV/u and an intensity of 270 nA, and a ^{238}U beam with an energy up to 2.2 MeV/u and an intensity of 30 nA. The other experiment, e^+e^- resonances, did not need the beam. It was done whenever the HERA facility was not being used for the online experiments. The HERA facility was shut down in December 1992 in preparation for the construction of its replacement facility, Gammasphere.

2.1 The High Energy-Resolution Array (HERA)

HERA was a detector system consisting of 21 high-resolution γ-ray detectors and 40 low-resolution γ-ray detectors which composed the "central ball". Each high-resolution γ-ray detector consisted of a Ge detector of about 20% efficiency surrounded by a coaxial Bismuth Germanate (BGO) scintillator which served as a

Compton suppressor. The front of the BGO scintillator was extended by a NaI scintillator, which was a separate unit that suppressed the γ rays backscattered by the Ge detector. Fig. 2.1 shows schematically the configuration of half of the HERA detectors.

The 21 detectors were assembled as three horizontal rings of seven each. Each detector was supported in its individual holder which was positioned in the system via two horizontal steel rings. The steel rings were mounted on vertical steel posts. The detectors' distance to the target and their angle to the horizontal plane could be changed by moving the relative height of the two horizontal rings. In addition, their distance to the target could also be changed by slides that screw on the holders' base. The distance from the front face of the Ge detectors to the target was 15 cm for the experiments reported in these studies. The Ge detectors viewed the target through a conical hole in the central ball detectors. For these experiments, the detector facing the beam-line was removed to let the beam pass through to the Faraday collection cup at the end of the beam line.

Each of the the 21 high-resolution Ge detectors had its own individual high-voltage supply, preamplifier, and high-resolution amplifier. All the high-voltage supplies and high-resolution amplifiers were specifically made at LBL to use with HERA detectors. The high-voltage supplies were identical and interchangeable. However, the high voltages set on the various Ge detectors were not identical. The high-resolution amplifiers were not interchangeable; each one was adjusted individually for each detector, and therefore attached to that particular detector. Also, the power supply for each detector preamplifier came from its amplifier. The detectors were kept permanently at liquid nitrogen (LN) temperature. Each detector had its own

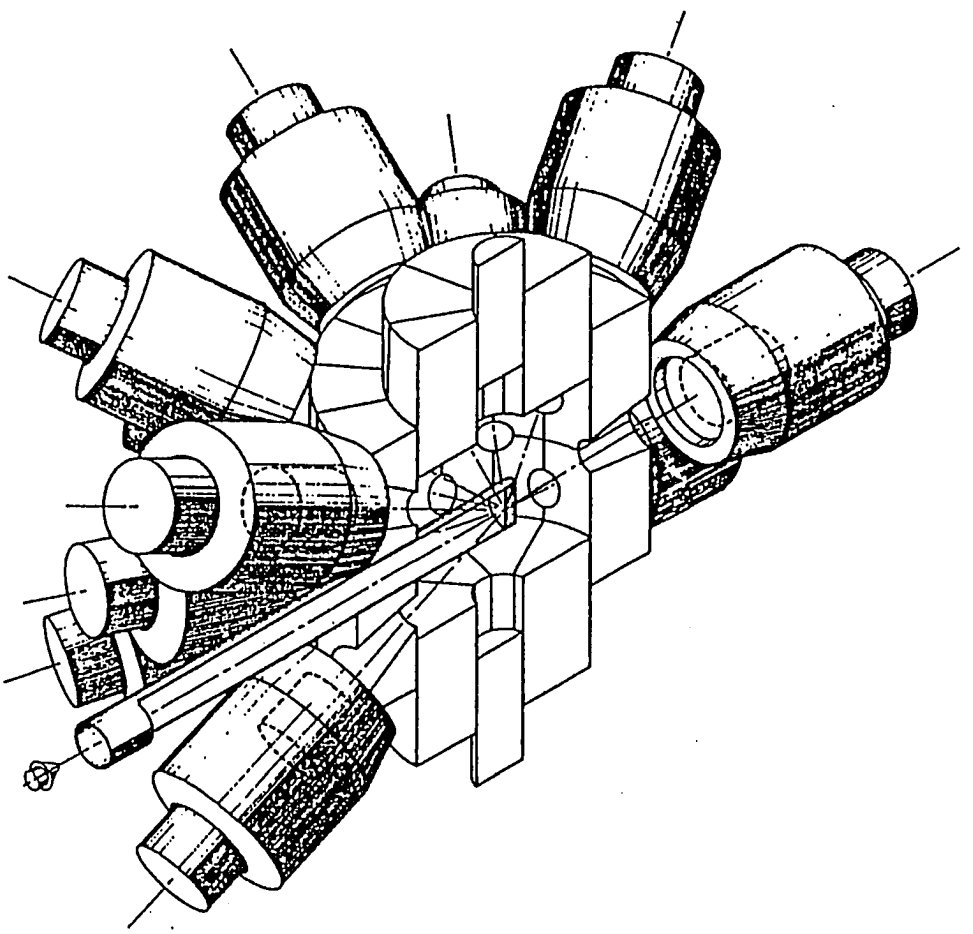

Figure 2.1: Drawing of HERA, showing half the detectors

1.5-liter Dewar filled with LN. The filling of these Dewars was automatic and was controlled from a dedicated personal computer (PC 286). If a Ge detector accidentally warmed up due to a failure of the LN filling system, the bias shutdown of the preamplifier sent a signal to turn off the high voltage of that detector and to sound the alarm to alert the cyclotron operator that a detector had been warmed up.

The 40-element central ball was located between the target and the high-resolution detectors. It had a high granularity (40 elements) and a high solid angle ($\approx$85% of 4π steradians) in order to provide a reliable total γ-ray multiplicity and total γ-ray energy for the nuclear reaction studied. It had a cylindrical symmetry and consisted of three concentric upper rings (14, 5, and 1 elements), and three lower rings (also 14, 5, and 1 elements) symmetrically placed with respect to the horizontal plane containing the beam. The support structure consisted of steel rods attached to aluminum plates which were fixed on the floor and ceiling. The detector was centered by moving these plates in all three directions. The two outer 14-element rings of the central ball were fixed and held via two aluminum support rings attached to the rods. The middle and inner detector rings could move up and down together. There were recesses on the outer-ring BGO detectors so that the high-resolution Ge detectors could be brought closer to the target. This central ball detector also served as an active shield for the BGO and NaI suppressors and as a collimator for the Ge detectors.

The BGO detectors and the NaI detectors obtained their high voltage from a single 256-channel supply unit (model LeCroy 1440). Each BGO suppressor was composed of six electrically independent sectors and each sector was connected to a high-voltage channel. Each BGO central-ball detector and each NaI detector was also connected to a high-voltage channel. The high voltage of the detectors could be

changed individually or turned on or off through the control unit of the high-voltage supply or through the data acquisition computer system (VAX 3100 work station).

2.2 Data acquisition

HERA was located in cave 5A of Building 88 at LBL. The high-voltage supplies for the BGO and NaI Compton suppressors were inside the cave. The high-voltage supplies for the Ge detectors and the power supplies for the Ge pre-amplifiers were fed from the "data collecting area" outside of the cave. The signals from the Ge, shield, and central-ball detectors were sent back out of the cave to the bins in a rack in the "data collecting area" through coaxial cables whose lengths were approximately 15 meters.

Due to the complication of the electronics involved, the data acquisition system was divided into 4 major areas: Ge spectroscopy; Ball spectroscopy; Master gate (MG); and Timing spectroscopy. The connections between these areas and FERA Driver (model LeCroy 4301) are shown in Fig. 2.2. FERA is an acronym which stands for Fast Encoding and Readout ADC, which is a multiple high-speed charge-integrating analog-to-digital converter (ADC). Each module contains 16 independent fast ADCs. The FERA Driver is a module which controls FERAs and other independent ADCs. It also accepts the signals from the FERAs and the ADCs, formats them, and sends them to the data acquisition system.

Except for some minor changes in the "e^+e^- resonances" experiment, the first three areas were the same for all experiments in this work. The fourth area (the timing) was different for each experiment and is described separately in detail in this chapter for each experiment.

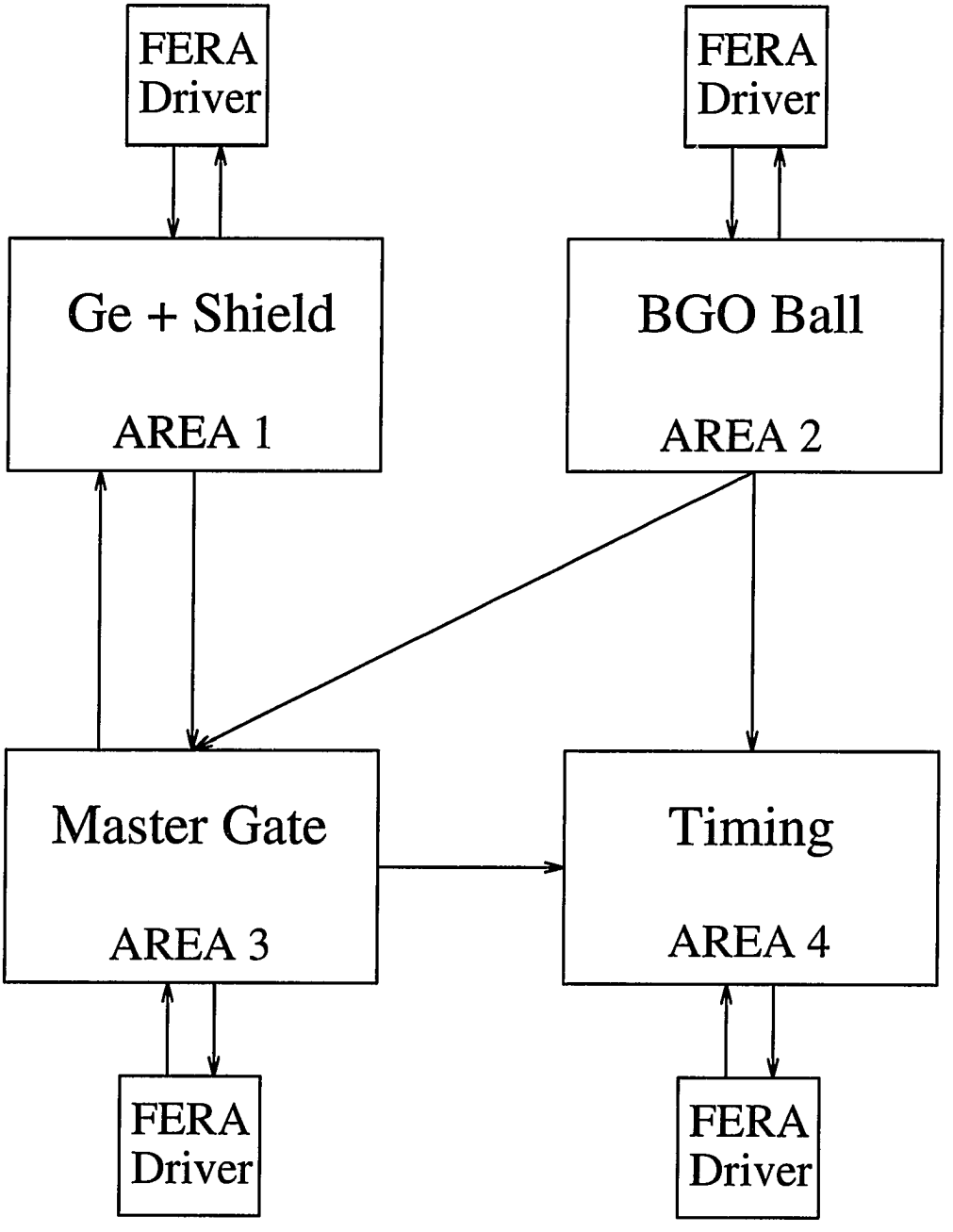

Figure 2.2: Block diagram of HERA electronics

2.2.1 "Ge + Shield" electronics

Because of the high counting rate of the Ge detectors and the slow processing time of the amplifiers, the amplifiers would saturate and have large deadtimes if all the Ge pulses were processed thoroughly. Since the Compton suppressors were highly efficient, the number of pulses processed by the linear amplifiers was reduced greatly by only amplifying the signals that were anticoincident with the shield signals. It was estimated that only about one third of the Ge pulses were not in coincident with the Compton suppressors. Furthermore, when the true Ge-Ge coincident condition and BGO ball selective condition were used to set the gate on the amplifiers, the number of thoroughly processed pulses was reduced much further. Therefore, special home-made amplifiers (Gated Integral Amplifier with SCA) were built to use in this system.

The block diagram of the Ge spectroscopy is shown in Fig. 2.3. In the "Ge + Shield" (LBL-made) module, the Ge and shield signals were summed, shaped, and sent to a FERA (model LeCroy 4300). Each ADC in a FERA unit has 1024 channels, and the calibration was set at 5 keV/ch. The pedestal cut-off levels for these "Ge + shield" summed signals (and for the BGO ball signals in area 2) were set relatively high to avoid electronic noise. They were set to 275 keV for the ^{198}Bi experiment and to 250 keV for the ^{191}Au and e^+e^- experiments. The outputs from FERA were sent to the FERA Driver and finally to the data acquisition system. The bypassed signal went to the coincident circuit. The Ge pulse was then quickly amplified and shaped by the timing filter circuit in the "Gated-Int-Amp w/SCA" (LBL-made) module and sent to the CFD (Constant-Fraction Discriminator, Quad CFD, model Ortec CF4000). The logic output from this CFD was the primary signal for the

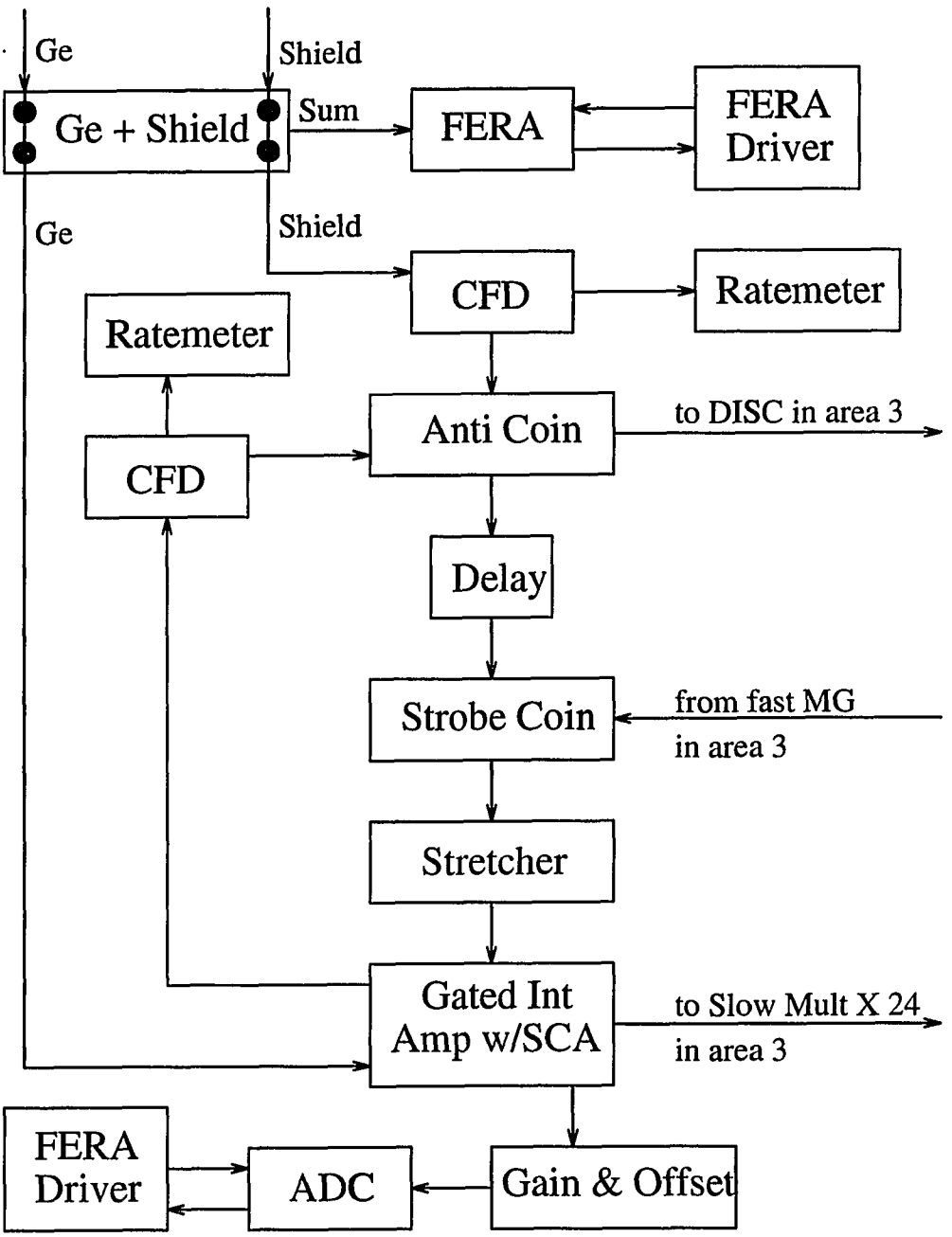

Figure 2.3: Block diagram of area 1 of HERA electronics

anticoincidence module. The logic gate signal was from another CFD which processed the Compton suppressor's pulse. One of the outputs from the anticoincidence unit was sent to the pulse-shaper in area 3 where, together with other similar signals from other Ge detectors and information from the BGO ball, a fast MG (Master Gate) logic signal was generated when the requirements for doubles and triples (and/or singles) were met. This fast MG signal was in turn fed back to the coincident circuit in the form of a logic gate signal which gave the Gated-Int-Amp the permission to fully process the original Ge pulse.

This type of circuit shown in Fig. 2.3 reduced the number of pulses processed by the linear amplifier to a small fraction. Depending on the reaction and the type of experiment, a typical counting rate of a Ge detector was about 15 kHz while the fully processing rate of the Gated-Int-Amp was only about 300 Hz. The discriminated logic signal from the Gated-Int-Amp was then sent to the Slow-Multiplicity (LBL-made) unit, and, together with other similar signals, formed a slow MG signal. The amplified output from the Gated-Int-Amp was then sent to the Gain & Offset module. From here, the pulse height was adjusted to match the calibration (controled by the online computer) before it was sent to the ADC and then to the FERA Driver. Since these ADCs have 8064 channels, with the online calibration of 0.5 keV/ch, the maximum energy that could be measured is about 4 MeV. To measure higher-energy γ rays, the Gain & Offset units could be changed (e.g. to 0.75 keV/ch) as in some other experiments to accommodate the 8064-channel ADC range. Of course, the energy resolution was reduced for the larger energy range.

2.2.2 BGO ball electronics

Fig. 2.4 shows the block diagram of the BGO ball spectroscopy. The branch that goes to FERA is the same as the "Ge + shield" sum signal branch in Fig. 2.3. For the other branch, each octal discriminator (model Ortec CF 8000) received the pulses from 8 BGO ball detectors. (There were 5 such modules to accommodate a total of 40 BGO ball detectors.) The octal discriminator has: an OR logic output, a multiplicity (M) output which provided a voltage proportional to the number of input pulses, and an analog sum (Σ) output which provided an attenuated summation of all inputs. The OR outputs from 5 octal discriminators were then combined in the Logic-Fan-In unit and the final OR signal was used as the stop signal for the timing in area 4.

The multiplicity (M) outputs from 5 octal discriminators were fed into another octal discriminator where all the signals are summed up and sent to the amplifier through the analog sum (Σ) output. The height of this output was proportional to the total input signals from the ball. This pulse was then amplified and sent to the discriminator which had the threshold set up to cut off the low multiplicity events. For the ^{198}Bi and ^{191}Au experiments, the minimum ball multiplicity was set to a value of six. For the e^+e^- experiment, this ball-multiplicity branch was not used.

2.2.3 Master gate electronics

Fig. 2.5 shows the block diagram of the master gate circuit. Three octal discriminators (LeCroy model 623B) accepted the Ge logic pulses (from the anticoincidence modules in Fig. 2.3), shaped the pulses, and sent the output signals to the Multiplicity-Logic-Unit (MLU, model LeCroy 380A) and Logic-Fan-Ins (LoFI, model

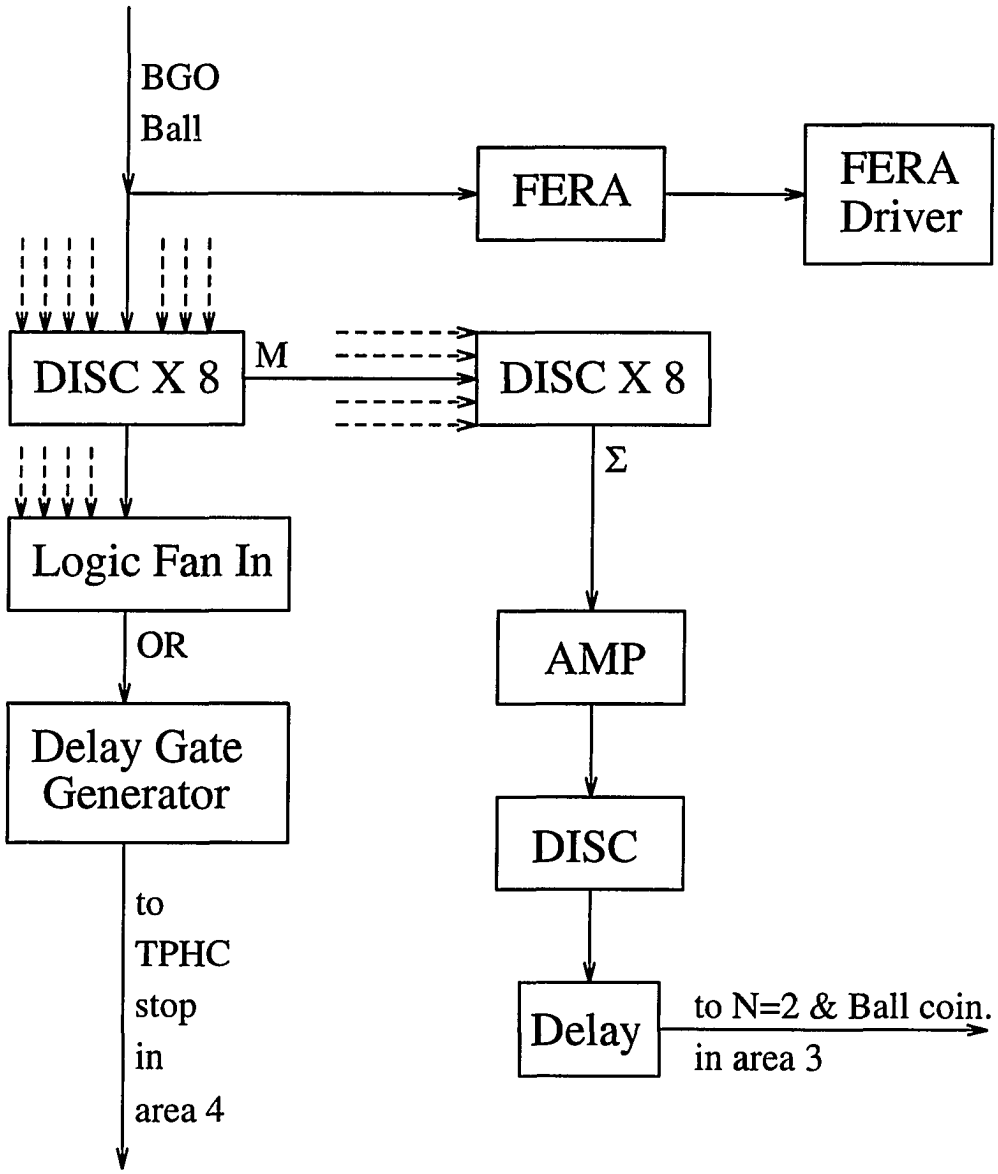

Figure 2.4: Block diagram of area 2 of HERA electronics

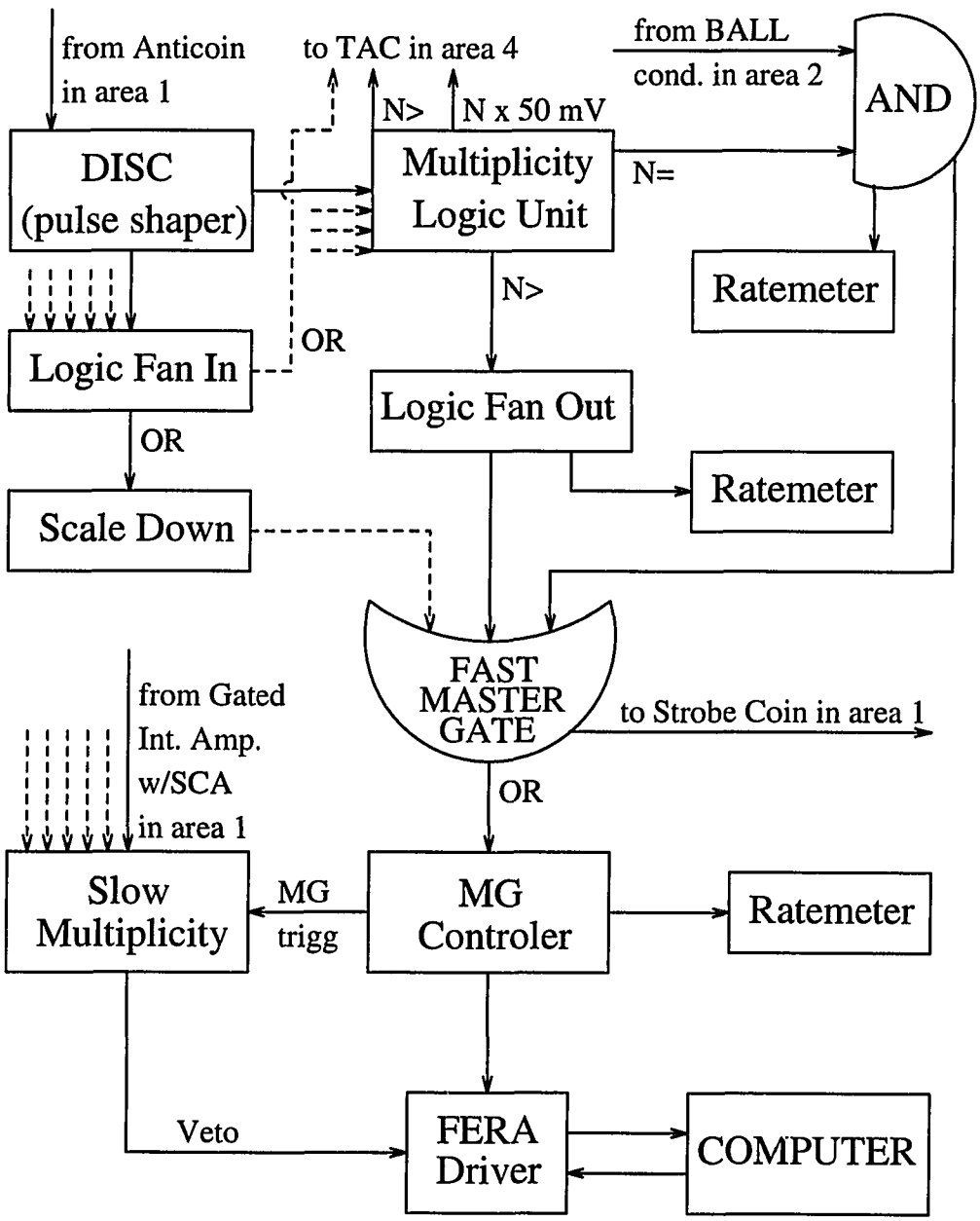

Figure 2.5: Block diagram of area 3 of HERA electronics

LeCroy 429A). This LeCroy 429A unit can actually be used as either a Logic-Fan-Ins (LoFI) or a Logic-Fan-Outs (LoFO). The MLU, which accepted the inputs of Ge pulses from 20 pulse-shapers, had a multiplicity-control knob and could be set to send out the outputs depending on the multiplicity of the event. (For the ^{198}Bi and ^{191}Au experiments, the multiplicity M for this unit was set at M = 2; for the e^+e^- experiment, it was set at M = 1.) The "N×50mV" and "N " output signals were sent to the timing circuit in Area 4. Another N output was sent to the master gate (MG, an LoFI unit, model LeCroy 429A). The "N=" output was combined with the ball signal (from Fig. 2.4) in the coincidence unit and its outputs were sent to the MG and the timing circuit. The dashed arrow pointing to the MG (Fig. 2.5) was from the single Ge circuit. It was used whenever single spectra were needed, such as when doing γ-ray energy calibration using a weak source. One of the outputs of the MG was sent back to the Strobe-Coincidence (LBL-made) unit (Fig. 2.3). The other output was combined with the Slow-Multiplicity output at the FERA Driver unit which controlled the ADC reading of FERA.

2.2.4 Timing electronics

The basic timing circuit for all experiments reported in this work was very similar. The start signal was always coming from one of the Ge detectors and the stop signal coming from another Ge detector or from the BGO ball. However, in order to achieve the best results for each different experiment, the electronic modules were set up somewhat different for each experiment. The reason for using the BGO ball signals as the stop signals in the ^{198}Bi and the ^{191}Au experiments, even though the BGO ball pulses were much faster than those of Ge, was because the counting rate

of the ball was much larger (hundreds of times larger) than the double (or triple) Ge coincident counting rate. The time-to-amplitude conversion process began when a start signal was accepted. An output signal was generated only if a stop signal was received within a selected time range after the initiation of the start signal. Therefore, using the slow count-rate signals of the Ge as the start signals reduced the working time and prevented paralysis of the TPHC (Time-to-Pulse-Height Converter) unit due to high input count rate of the ball.

^{198}Bi timing In the ^{198}Bi experiment, the time differences between the first coincident BGO ball detector and the second, third (for triple coincidences), and fourth (for quadruple coincidences) coincident Ge detectors were recorded. Fig. 2.6 shows the block diagram for the timing apparatus of this experiment. The start signals came from the "N×50mV" output of the the MLU in area 3. This "N×50mV" signal had its pulse height directly proportional to the number of γ rays in the Ge detectors (i.e., pulse height of 50 mV for single, 100 mV for double coincidence, 150 mV for triple coincidence ...). This "N×50mV" signal also had its shape directly related to the timings of the γ rays in the Ge detectors. Fig. 2.7 shows the formation of the "N×50mV" output signal from a double coincident event. The formations of triple and higher order events are also similar.

The "N×50mV" signal was fanned out at the Linear Fan Out (LiFO, LBL-made) into three. The pulses from the LiFO went to the discriminators (Ortec CF 8000) which had different thresholds set up for different fold events. The threshold of the "DISC N≥2" was about 75 mV, the "DISC N≥3" was about 125 mV, and the "DISC N≥4" was about 175 mV. The output signals from the discriminators were then sent

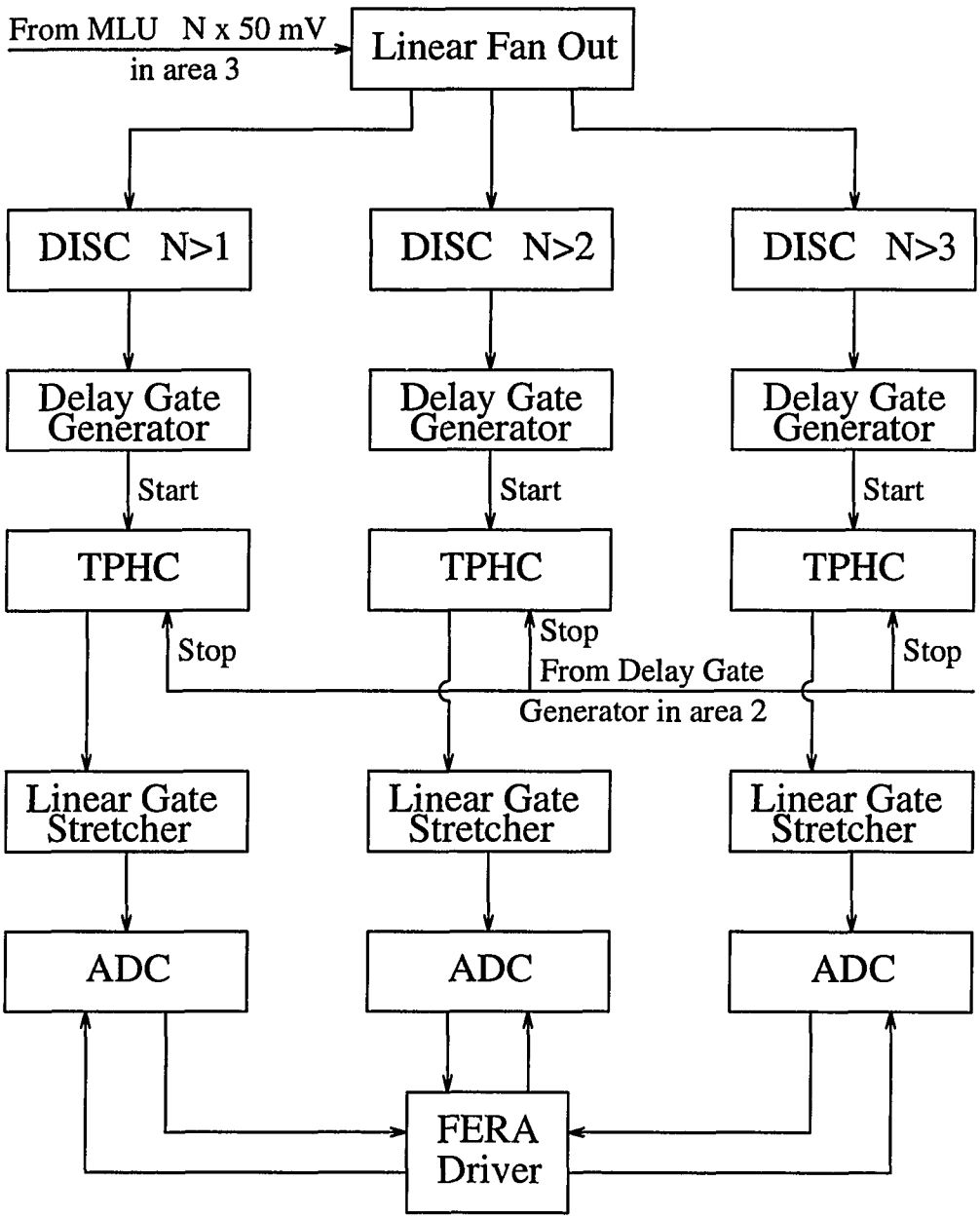

Figure 2.6: Block diagram of ^{198}Bi timing electronics

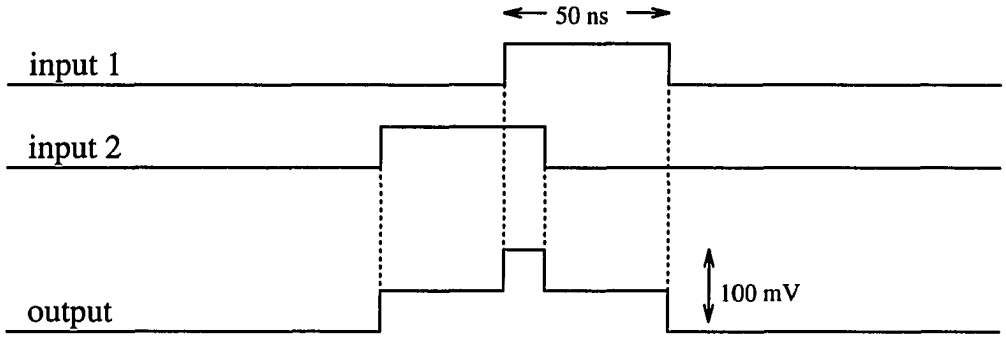

Figure 2.7: "N×50mV" output signal formation in the Multiplicity Logic Unit for a double coincident event

to the Delay & Gate Generators (Quad DGG, Ortec model CO4010) where they were shaped, delayed, and sent to the start-input of the Timing to Pulse Height Converter (TPHC, LBL-made). The stop-signal came from the DGG (Ortec model 416A) of the BGO branch in area 2. The outputs from the TPHCs were shaped and delayed by the Linear Gate Stretcher (LGS, Ortec model 542) before being sent to the ADCs.

^{191}Au timing In the ^{191}Au experiment, the time differences between the first coincident BGO ball detector and the first Ge detector were recorded. Fig. 2.8 shows the block diagram for the timing apparatus of this experiment. The start signals came from the LoFI(OR) unit, the "N>2" output of the MLU, and the AND (N=2 & BGO) in area 3. The signal from the OR unit corresponded to the timing of the first Ge γ ray. The signals from the MLU and the AND units acted as the gates for the OR signal. A start signal was generated if the event satisfied the Ge fold conditions (N > 2 or N = 2 and BGO multiplicity $\geq$ 6). The rest of the circuit was the same as that of the ^{198}Bi experiment described earlier.

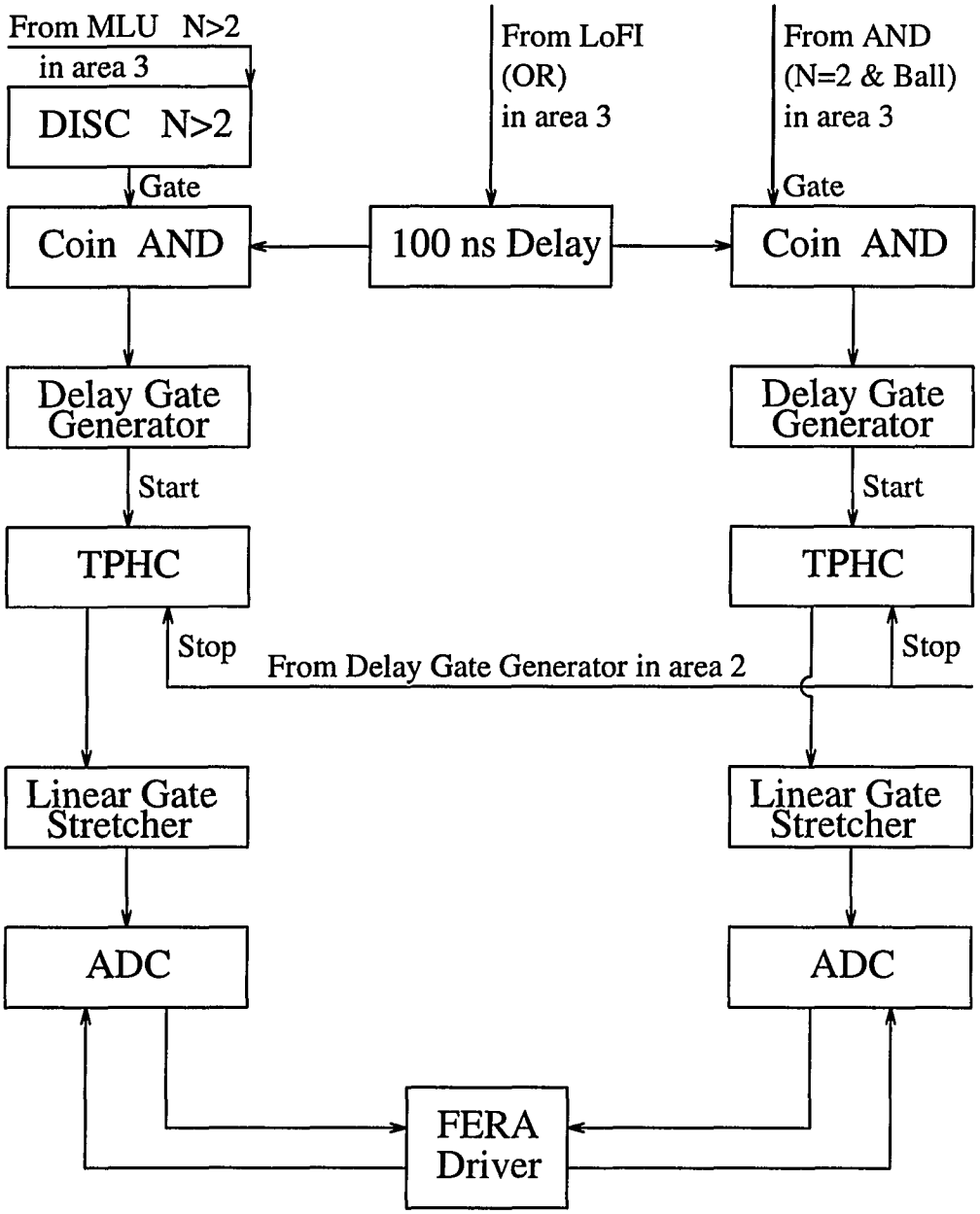

Figure 2.8: Block diagram of ^{191}Au timing electronics

e^+e^- timing of the lead target In the e^+e^- experiment using the lead ball, the time differences between the first Ge detector and the second Ge detector were recorded. Fig. 2.9 shows the block diagram for the timing apparatus of this experiment. The start signals came from the "N>1" output of the MLU in area 3. The timing of this signal corresponded to the timing of the second Ge detector. The stop signals, corresponded to the timing of the first Ge detector, came from the LoFI(OR) unit in area 3. The rest of the circuit was similar to that of the ^{198}Bi experiment.

e^+e^- timing of the copper target In the e^+e^- experiment using the copper ball, the time differences between the first Ge detector and the second or third Ge detector were recorded. Fig. 2.10 shows the block diagram for the timing apparatus of this experiment. The start signals came from the "N×50mV" output of the MLU in area 3. The discriminators' thresholds were set for double and triple coincident events. The timings of these signals corresponded to the timings of the second and third Ge detectors. The stop signals, corresponded to the timing of the first Ge detector, came from the LoFI(OR) unit in area 3. The rest of the circuit was similar to that of the ^{198}Bi experiment.

2.2.5 Data acquisition computer system

The processed data were passed to the data acquisition computer, a VAX 3100 workstation. There, the data were filtered, formatted, and stored on exa-byte tapes. The software used to handle the data from the HERA system was developed at LBL. The CDAT program was used to process and write raw data to tape. The data-format of CDAT code could not be changed. During the experiment, another

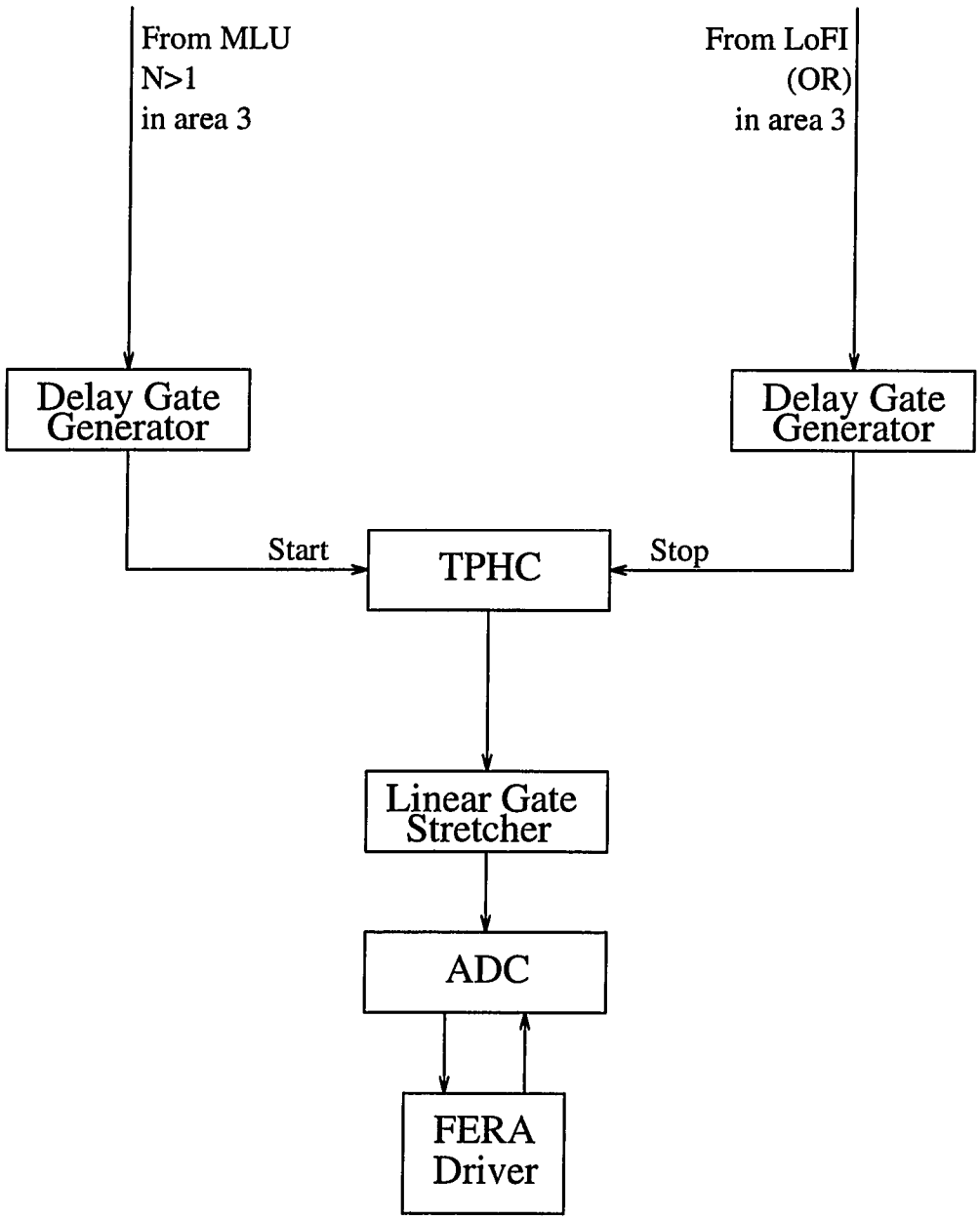

Figure 2.9: Block diagram of the timing electronics of the e^+e^- resonance using the lead ball

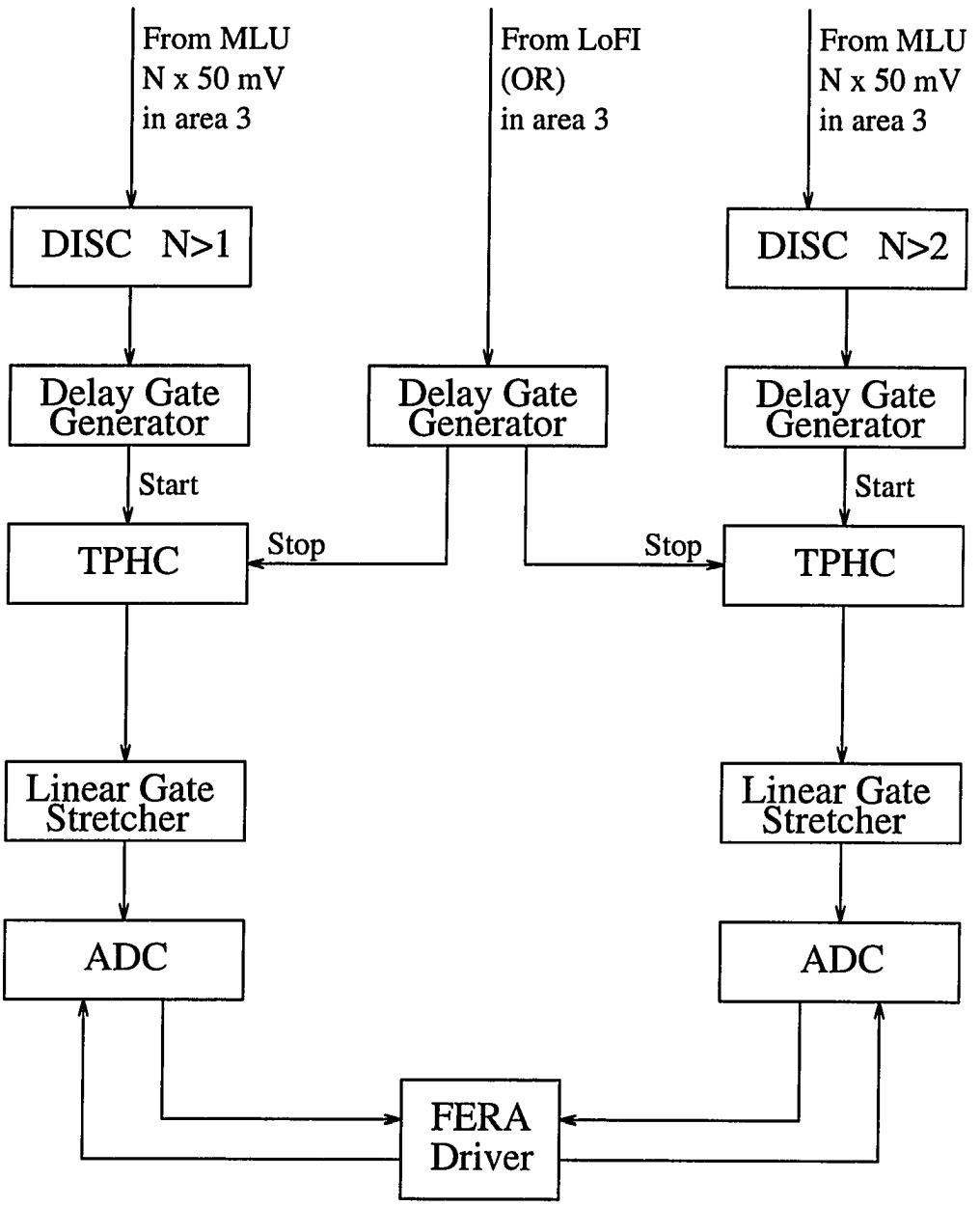

Figure 2.10: Block diagram of the timing electronics of the e^+e^- resonance using the copper ball

program named VSORT was run to further filter the data and to put the data into the desired spectra. These spectra (including matrices) could display almost any thing one wants them to present such as "count vs. energy" spectra for each different Ge, shield, or BGO ball detector, or timing spectra between the pairs of detectors, or multiplicity, etc ... These spectra were frequently viewed during the online sorting to check on the conditions of the run, etc...

The VSORT program has a subroutine code which can be modified to read the data directly from CDAT, from CDAT formatted data on tape, or from any other type of formatted data. It can even write data to tape in one's own format. This subroutine is the heart of the analytical software for use with HERA data. One was able to modify it to create the desired spectra for analysis of the data. A third program, VLOOK, was used to read and display the spectra from VSORT. It has some (even though limited) capability to analyze the data (such as slicing the matrix in the X or Y direction ...). It also has the capability to update the output spectra from VSORT and is used together with VSORT during the data-taking process to check on the run. The fourth program, LOOK, was the main program used to analyze the VSORT spectra. One could use it to manipulate the spectra in many ways and the results could be written to other files for later analysis using the same format (of VSORT) or different format such as ASCII or the format for program FITEK used by the Nuclear Physics group at Lawrence-Livermore-National Laboratory (LLNL).

A VAX 3100 (or better) workstation was needed to analyze the data using VSORT, LOOK, or FITEK. The high-spin physics groups at LBL and LLNL had many of those workstations available. At ISU, the high-energy physics (HEP) Alpha group had two VAX 3100 workstations and one of those was dedicated for the analysis

of the present work. Part of the ^{198}Bi data was analyzed at LLNL using the program VSORT and FITEK, and part of the e^+e^- resonance data was analyzed at LBL using VSORT and LOOK. All the ^{191}Au SD work was done at LBL. The remaining data was analyzed at ISU using VSORT and LOOK.

CHAPTER 3. HIGH-SPIN γ-RAY SPECTROSCOPY IN ^{198}Bi

3.1 Experimental method

The states in ^{198}Bi were populated using the ^{181}Ta(^{22}Ne, 5n) reaction at beam energies of 116 MeV and 120 MeV. The target consisted of three stacked self-supporting foils of ^{181}Ta, each foil about 560 μg/cm^2 thick. The beams were provided by the 88-Inch Cyclotron at the Lawrence Berkeley Laboratory (LBL). The γ-ray coincidences were measured with the HERA spectrometer array. All three- and higher-fold events were recorded. Two-fold events were recorded only if six or more inner BGO elements were in prompt coincidence with any two of the Ge detectors. The events were recorded together with γ-ray sum energies (H) and multiplicities (k) of the Ge detectors and BGO ball. Also, the time differences between the γ rays detected in the BGO ball and the second, third, and fourth coincident Ge detectors were recorded. There were not many quadruple events in the data; therefore, in order to reduce the work involved, only the timing of the second and third Ge detectors were used in the analysis. The main purpose of this experiment was to search for superdeformation in ^{197}Bi and ^{198}Bi. The timing information in this experiment was not intended for lifetime measurements, but was planned for the rejection of delayed γ rays and neutron-induced events from the data. The electronic setup was described in chapter 2. A total of 62×10^6 and 134×10^6 double-coincidence events and 12×10^6

and 26×10^6 triple- and higher-coincidence events were recorded for the two runs at 116-MeV and 120-MeV bombarding energies, respectively.

3.2 Data analysis

3.2.1 Identification of ^{198}Bi

The identification of the products is based on the observation of coincidences between γ rays and X rays and on the excitation functions. In the experiment, the ^{181}Ta target was bombarded with ^{22}Ne at 116 MeV and 120 MeV. At the energies used in the experiment, the strongest decays should be the 5n and 6n channels (i.e., ^{197}Bi and ^{198}Bi). The 4n, 7n, pxn, αxn... channels were about an order of magnitude or more weaker. The transitions were assigned to ^{198}Bi due to the following arguments:

a) The strongest groups of prompt γ rays from the spectra at both energies were found to be in coincidence with the X rays of bismuth, which means that these γ rays are mainly from the decays of excited states of one or two Bi isotopes, ^{197}Bi and/or ^{198}Bi.

b) Those most intense γ rays are not in coincidence with any γ ray from ^{197}Bi. The ratio of the total intensities of those intense γ rays to the ^{197}Bi γ rays are about 15 to 1 for the 116-MeV data and about 6 to 1 for the 120-MeV data. The intensities of the known γ rays of ^{197}Bi from the prompt data were somewhat weak because most of the γ transitions of ^{197}Bi decay from isomeric states ($\approx$ 200 ns half-lives). Also, the ratio of those intense γ rays produced by the 116-MeV reaction to those produced by the 120-MeV reaction is about a factor of two larger than the ratio of known ^{197}Bi γ rays in those reactions.

c) Plots of the total energy and total multiplicity of the coincident events were

obtained. The total energy of an event is the sum of all the γ-ray energies deposited in the Ge detectors, the Compton suppressors, and the elements of the BGO ball. Similarly, the total multiplicity of an event is the total number of the detector units that have γ-ray energies deposited in them. Each Ge detector and its Compton-suppressor detectors are counted as one unit. Each element (detector) of the 40-element central BGO ball is a unit. The triple- and higher-fold coincident events were sorted with the condition that at least three γ rays must be in coincidence with three gates in a set of gates. The use of the triple-gate condition insured that most of the events in each spectrum came from the right nucleus. The set of the ^{197}Bi gates consisted of all known transitions (except the 97-keV transition) below the 2385-keV state in the ^{197}Bi nucleus (a total of 10 gates). The set of the presumably ^{198}Bi gates consisted of 11 transitions of a high intensity cascade. This cascade of transitions is denoted as band C and band D in subsection 3.2.4. The total energy and total multiplicity spectra of the events that satisfied the above condition were obtained. The background spectra consisted of all the events regardless of the triple-gate condition above. The background spectra were normalized such that when they were subtracted from the triple-gated spectra obtained above, the resulting total energy spectra would have about zero counts at either very low energy ($\approx$ 1 MeV) or very high energy ($\approx$ 30 MeV) and the resulting total multiplicity spectra would have about zero counts at either multiplicity of one or multiplicity of 30. The spectra shown in Fig. 3.1 and Fig. 3.2 have the background subtracted already. From Fig. 3.1 and Fig. 3.2, it is apparent that the total γ-ray sum energy and multiplicity distributions of ^{197}Bi and of the unknown (presumably ^{198}Bi) nucleus are very different. Both the total γ-ray sum energy and the total γ-ray multiplicity distributions are expected to

peak at higher values for ^{198}Bi than for ^{197}Bi because the reactions leave ^{198}Bi with higher excitation energy. (More energy is carried off by the additional neutron when ^{197}Bi is produced.)

d) In addition to this, the correlation matrices of delayed E_γ-E_γ coincidences were obtained. A correlation E_γ-E_γ matrix is a symmetrical matrix which stores a pair of γ rays from a coincident event in both (x,y) and (y,x) positions. For a pair of coincident γ rays with energies E_1 and E_2, the matrix first adds one count to the position (E_1,E_2) and then adds another count to the position (E_2,E_1). For the triple- and higher-fold coincidences, the events were unfolded into pairs of double coincidences before putting them into the correlation matrices. Each triple-coincident event would unfold three pairs of coincident γ rays, each quadruple-coincident event would unfold into six pairs, etc...

In the experiment, the target used was thin enough to let most of the recoiling compound nuclei recoil away, so that γ rays that decayed from some long-lived isomeric states ($\gg$ 10 ns lifetime) and subsequent γ rays were not detected. However, a small fraction of the compound nuclei was stopped in the target and, together with the timing information, spectra of delayed γ rays were also obtained.

Delayed E_γ-E_γ matrices were constructed from the coincident γ rays detected by the Ge detectors about 200 ns or more after the prompt γ rays. The prominent γ rays from these matrices were the known γ rays of ^{197}Bi and ^{198}Pb. Most (or all) of the γ rays belonging to ^{198}Pb originated from the electron capture and β^+ ground-state decay of ^{198}Bi (11.8 min half-life). The γ rays from the unknown nucleus, strongly populated in the prompt coincident spectra, were not seen in true coincidence in the delayed spectra. This means that those γ rays did not decay from any long-lived

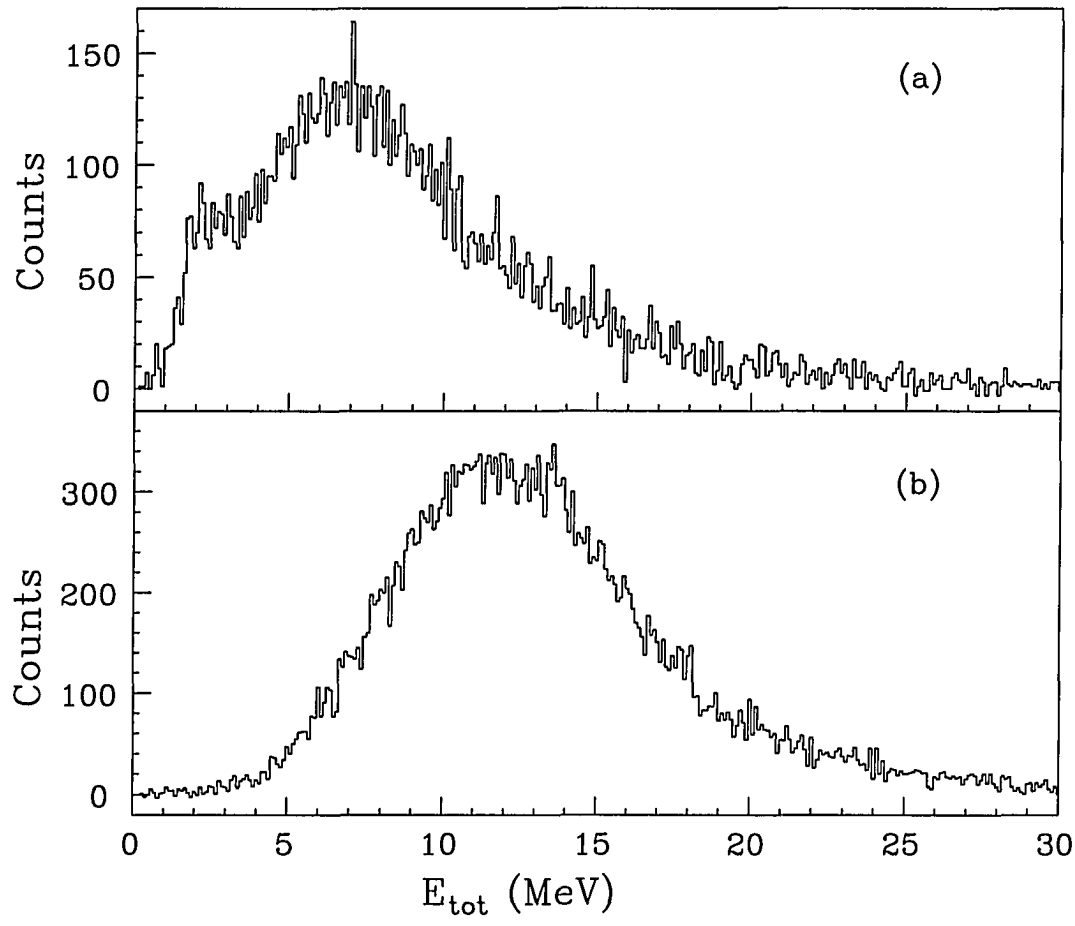

Figure 3.1: Total γ-ray sum energy distributions (a) of ^{197}Bi events and (b) of the presumed ^{198}Bi events

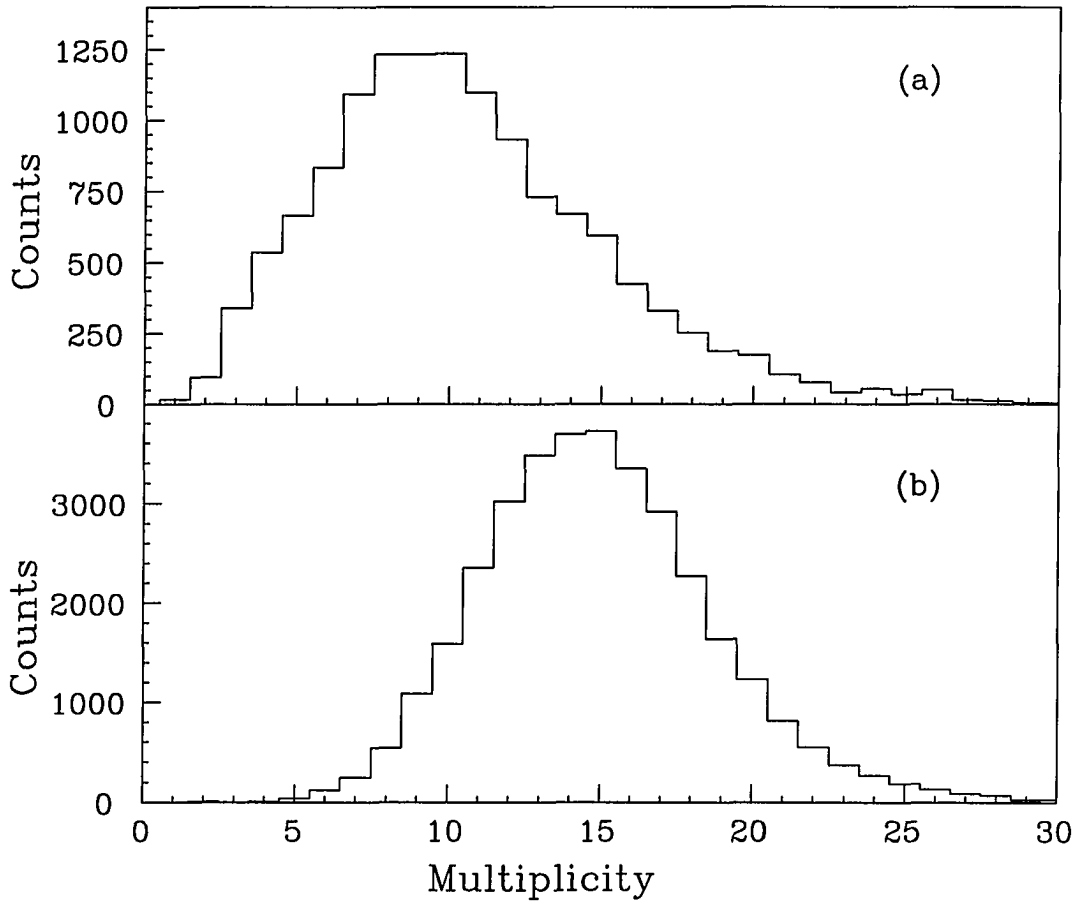

Figure 3.2: Total γ-ray multiplicity distributions (a) of ^{197}Bi and (b) of the presumed ^{198}Bi events

Table 3.1: Ratios of γ-ray intensities obtained at 116 MeV to those at 120 MeV for the γ-ray transitions from low-lying states in ^{197}Bi, ^{198}Pb, and ^{198}Bi. The transition energies of the gates and coincident peaks are shown in rows three and four

	Delayed ^{197}Bi	Prompt ^{197}Bi	Delayed ^{198}Pb	Prompt ^{198}Bi
116-MeV/120-MeV ratios	0.50(2)	0.44(2)	0.93(3)	1.01(3)
gate energies (keV)	187, 195	187, 195	197	294, 296
peak energies (keV)	405, 367	405, 367	562, 318	287, 318

isomer. From these matrices and the prompt matrices (and the spectra generated from them), the ratios of intensities obtained using the 116-MeV ^{22}Ne beam to those obtained using the 120-MeV ^{22}Ne beam of the delayed ^{198}Pb, delayed ^{197}Bi, prompt ^{197}Bi, and prompt unknown nucleus (presumably ^{198}Bi) were obtained and are given in Table 3.1.

The intensity of a nucleus was obtained by setting gates on one or two intense γ rays of that nucleus and measuring the areas of one or two intense energy peaks in coincidence with the gates. The gates for the γ rays of a nucleus are the same for both the 116-MeV and the 120-MeV data sets. The gated energies and the energies of the coincident peaks are shown in rows three and four of Table 3.1, respectively.

One can see from Table 3.1 that the γ-ray ratios for delayed ^{197}Bi and for prompt ^{197}Bi are basically the same. This is expected since the ratio of delayed intensity to prompt intensity for a given reaction product should not change significantly when the reaction is changed from one beam energy to another energy. The intensity ratios for delayed ^{198}Pb and for the prompt unknown-nucleus γ rays are also about the same, and these ratios are different from those for ^{197}Bi. Since the γ rays of ^{198}Pb are from

the electron capture and β^+ decay of ^{198}Bi, this implies that the γ rays from the unknown nucleus belong to ^{198}Bi.

Arguments a) through d), combined together, indicate that the unknown nucleus is ^{198}Bi. The energies, intensities, and level-scheme placements of the γ rays identified here as belonging to ^{198}Bi are shown in Table 3.2. The relative intensities were determined from the double coincidence spectra. Uncertainties in the least significant figures of the γ-ray energies and the relative γ-ray intensities are indicated in parentheses in column one and column two, respectively. The uncertainties of the energies shown in Table 3.2 already had the uncertainties from the energy calibration curve included. The energy calibration curve was calculated using the known γ-ray energies of ^{197}Bi and it was assumed to have the uncertainty of 0.1 keV for γ-ray energies ranging from 0 keV to 2000 keV. The relative detector efficiencies were assumed to have the uncertainties of 5% for γ-ray energies ranging from 100 keV to 4000 keV and they were included in the calculations of the γ-ray relative intensities shown in Table 3.2. For the γ rays with known multipolarities (shown in column three), their corresponding relative intensities were also corrected for the internal conversion coefficients. For the γ rays with unknown multipolarities, no corrections for the internal conversion coefficient was done. Column four shows the levels where the transitions depopulate. The values E_0, E_1, and E_2 are the linking transition energies and are not known.

Due to the large numbers of the states and of the γ rays, the level scheme deduced from the present work is separated into two parts based on the excitations of neutrons and/or protons. The first part, based on the excitations of neutrons, is further divided into six branches: low-lying level structure and five bands (A, B, C,

Table 3.2: Transitions in ^{198}Bi produced by the ^{181}Ta(^{22}Ne, 5n)^{198}Bi reaction at 116 MeV and 120 MeV bombarding energies. The confirmed multipolarities of some transitions are shown without the parentheses. The multipolarities indicated in parentheses are assumed values. The intensity values have been corrected for the Ge detector efficiency. The intensities of the transitions with the known multipolarities (confirmed or assumed) have also been corrected for the internal conversion coefficients

γ-ray energy (keV)	Relative γ-ray intensity	Inferred multipolarity	Placement (keV)
107.0(1)	860(52)	M1	1769.7
107.8(1)	190(34)	(M1)	3179.7+E_0
115.7(1)	700(41)	M1	1662.7
138.0(2)	73(21)	(M1)	2634.3+E_2
142.2(1)	39(5)		2595.4+E_1
157.3(2)	8(2)		2453.2+E_1
169.7(1)	100(12)	(M1)	2804.0+E_2
203.3(1)	99(16)	(M1)	4146.8+E_2
210.3(1)	60(10)	(M1)	3737.0+E_0
213.1(1)	180(12)	(M1)	3071.9+E_0
214.3(1)	110(10)	(M1)	3018.3+E_2
226.1(1)	110(12)	(M1)	4372.9+E_2
228.9(1)	120(12)	(M1)	3965.9+E_0
242.0(1)	340(24)	(M1)	3421.7+E_0
254.3(1)	100(11)	(M1)	4220.2+E_0
269.2(1)	110(10)	(M1)	3287.5+E_2
287.4(1)	250(15)	(M1)	1950.1+E_0
289.4(1)	110(12)	(M1)	4662.3+E_2
291.8(1)	89(8)	(M1)	4612.0+E_0
294.1(1)	210(12)	(M1)	2244.2+E_0
296.8(1)	220(13)	(M1)	2541.0+E_0
300.4(1)	25(4)		1841.4+E_1
301.9(1)	70(5)		3401.3
317.8(1)	290(18)	(M1)	2858.8+E_0
320.2(1)	100(7)		4844.6
320.7(1)	72(9)	(M1)	4932.7+E_0
320.8(1)	34(3)	(E2)	3179.7+E_0

Table 3.2: (continued)

γ-ray energy (keV)	Relative γ-ray intensity	Inferred multipolarity	Placement (keV)
325.8(1)	47(6)	(M1)	3613.3+E_2
330.2(2)	40(14)	(M1)	3943.5+E_2
330.6(1)	120(7)		3857.7
333.8(5)[a]	50(16)	(M1)	3192.6+E_0
334.1(5)[a]	50(16)	(M1)	3526.7+E_0
345.4(1)	860(60)		2115.1
346.5(1)	69(12)	(M1)	5279.2+E_0
353.3(1)	48(9)	(M1)	5632.5+E_0
363.0(1)	86(11)	(M1)	5025.3+E_2
372.1(5)[a]	320(70)	(M1)	3793.8+E_0
372.2(5)[a]	120(40)	(M1)	4545.7+E_0
379.0(1)	270(15)		3124.3
379.8(1)	200(13)	(M1)	4173.6+E_0
389.2(1)	80(7)		4246.9
401.6(1)	90(6)	(M1)	4947.3+E_0
402.8(1)	230(13)		3527.1
421.1(1)	110(9)		1397.1+E_1
426.6(1)	55(10)	(M1)	5451.9+E_2
444.4(2)	20(5)		1841.4+E_1
454.9(1)	54(7)		2296.1+E_1
468.0(1)	110(10)		1547.0
469.4(2)	37(12)	(M1)	5921.3+E_2
482.8(1)	86(9)		1458.9+E_1
483.4(1)	100(9)		3099.4
497.0(2)	30(7)	(M1)	6418.3+E_2
500.9(1)	240(15)		2616.0
515.5(3)	20(7)	(M1)	6933.8+E_2
530.8(2)	31(4)	(E2)	3971.9+E_0
546.0(2)	42(9)		4524.1
546.2(3)	34(7)	(E2)	4612.0+E_0
564.9(2)	85(10)		1540.9+E_1

[a]Unresolved transition

Table 3.2: (continued)

γ-ray energy (keV)	Relative γ-ray intensity	Inferred multipolarity	Placement (keV)
576.8(5)[b]	75(30)		3978.1
581.5(3)	21(4)	(E2)	2244.2+E_0
591.6(2)	38(5)	(E2)	2541.0+E_0
611.8(1)	130(12)		2453.2+E_1
613.7(4)	14(4)	(E2)	4932.7+E_0
614.5(2)	88(9)	(E2)	2858.8+E_0
625.7(1)	340(20)	M1	874.2
630.2(1)	320(18)		2745.3
651.2(2)	25(4)	(E2)	3192.6+E_0
655.1(2)	64(11)		2496.3+E_1
667.8(2)	25(3)	(E2)	3526.7+E_0
672.8(1)	290(17)	M2	1547.0
782.0(2)	35(8)		3527.1
786.3(3)	23(4)		3401.3
788.9(2)	80(9)	E3	1662.7
865.4(1)	200(16)		1841.4+E_1
976.0(1)	480(26)		976.0+E_1
984.2(3)	94(15)		3099.4
990.0(2)	80(8)		1979.0
1037.3(2)	37(8)		2496.3+E_1
1123.0(3)	32(5)		4524.1
1298.8(3)	60(7)	E3	1547.0

[b]This transition is unresolved from another transition

D, and E). The second part, based on the excitation of at least one proton, is divided into two branches: low-lying level and oblate band. The levels are discussed in the following sections of this chapter.

The energies of the γ rays and their corresponding coincident γ rays seen in the data are shown in Table 3.3. The gates (column one) are placed in order from small transition energy to large transition energy. The coincident γ rays (column two) are placed according to their subgroups and their placements in the subgroups. The order of the subgroups is following: Low-lying level structure from neutron excitation, band A, band B, band C, band E, band D, low-lying level structure from proton excitation, and the backbending band decaying to the proton excited low-lying level structure. The order of the placements in each group is from low energy level to high energy level. Placing the coincident γ-ray energies in the second column this way makes it easy to trace the coin γ rays through the maze of the level scheme.

3.2.2 Low-lying levels of ^{198}Bi

In order to analyse the ^{198}Bi data, the coincident events were sorted into E_γ-E_γ and E_γ-Timing matrices. The E_γ-E_γ matrix was constructed following these criteria:

a) The minimum total energy of an event (i.e., sum of energy in all Ge detectors, Compton suppressor detectors, and BGO ball detectors) was 5.6 MeV and the maximum total energy was 21.0 MeV. According to the data in Fig. 3.1b, these values of minimum and maximum would allow most of the events from ^{198}Bi to be recorded while rejecting about half of the events from ^{197}Bi.

b) The minimum total multiplicity (i.e., the number of "Ge + Shield" units and BGO detectors in coincidences) was 8 and the maximum total multiplicity was

Table 3.3: Coincidence relations of the transitions in ^{198}Bi. The coincident γ rays are placed according to their subgroups and their placement in the subgroups

Gate γ-ray (keV)	Coincident γ-rays (keV)
107.1	990.0, 468.0, 625.7, 672.8, 1298.8, 115.7, 788.9, 345.4, 630.2, 379.0, 402.8, 782.0, 330.6, 389.2, 500.9, 483.4, 984.2, 301.9, 785.9, 576.8, 546.0, 1123.0, 320.2, 242.0, 372.1, 379.8, 372.2, 401.6
107.8	990.0, 468.0, 625.7, 672.8, 1298.8, 115.7, 788.9, 107.0, 287.4, 294.1, 581.5, 296.8, 591.6, 317.8, 614.5, 213.1, 530.8, 242.0, 372.1, 379.8, 372.2, 401.6
115.7	672.8, 625.7, 1298.8, 107.0, 345.4, 630.2, 379.0, 402.8, 330.6, 500.9, 483.4, 984.2, 301.9, 576.8, 320.2, 287.4, 294.1, 296.8, 317.8, 333.8, 334.1, 213.1, 107.8, 242.0, 372.1, 379.8, 372.2, 401.6
138.0	976.0, 169.7, 214.3, 269.2, 325.8, 330.2
142.2	379.0, 402.8, 330.6, 389.2, 976.0, 865.4, 421.1, 300.4, 611.8, 454.9, 157.3
157.3	976.0, 482.8, 865.4, 454.9, 142.2
169.7	976.0, 482.8, 865.4, 421.1, 655.1, 454.9, 138.0, 214.3, 269.2, 325.8, 330.2, 203.3, 226.1, 289.4, 363.0, 426.6, 469.4, 497.0, 515.5
203.3	379.0, 976.0, 655.1, 169.7, 214.3, 269.2, 325.8, 330.2, 226.1, 289.4, 363.0, 426.6, 469.4, 497.0, 515.5
210.3	287.4, 294.1, 296.8, 317.8, 333.8, 651.2, 334.1, 667.8, 228.9, 254.3, 291.8, 546.2, 320.7, 613.7, 346.5, 353.3
213.1	990.0, 468.0, 625.7, 672.8, 1298.8, 115.7, 788.9, 107.0, 287.4, 294.1, 581.5, 296.8, 591.6, 317.8, 614.5, 107.8, 242.0, 372.1, 379.8, 372.2, 401.6
214.3	976.0, 482.8, 1037.3, 865.4, 421.1, 655.1, 454.9, 138.0, 169.7, 269.2, 325.8, 330.2, 203.3, 226.1, 289.4, 363.0, 426.6, 469.4, 497.0, 515.5

Table 3.3: (continued)

Gate γ-ray (keV)	Coincident γ-rays (keV)
226.1	345.4, 630.2, 379.0, 976.0, 1037.3, 865.4, 655.1, 611.8, 169.7, 214.3, 269.2, 325.8, 330.2, 203.3, 289.4, 363.0, 426.6, 469.4, 497.0, 515.5
228.9	287.4, 294.1, 296.8, 317.8, 333.8, 651.2, 334.1, 667.8, 210.3, 254.3, 291.8, 546.2, 320.7, 613.7, 346.5, 353.3
242.0	990.0, 468.0, 625.7, 672.8, 1298.8, 115.7, 788.9, 107.0, 287.4, 294.1, 581.5, 296.8, 591.6, 317.8, 614.5, 213.1, 530.8, 107.8, 320.8, 372.1, 379.8, 372.2, 401.6
254.3	287.4, 294.1, 296.8, 317.8, 333.8, 651.2, 334.1, 667.8, 210.3, 228.9, 291.8, 320.7, 613.7, 346.5, 353.3
269.2	976.0, 482.8, 1037.3, 865.4, 421.1, 564.9, 655.1, 454.9, 138.0, 169.7, 214.3, 325.8, 330.2, 203.3, 226.1, 289.4, 363.0, 426.6, 469.4, 497.0, 515.5
287.4	990.0, 468.0, 625.7, 672.8, 1298.8, 115.7, 788.9, 107.0, 294.1, 296.8, 591.6, 317.8, 614.5, 333.8, 651.2, 334.1, 667.8, 210.3, 228.9, 254.3, 291.8, 320.7, 346.5, 353.3, 213.1, 530.8, 107.8, 320.8, 242.0, 372.1, 379.8, 372.2, 401.6
289.4	345.4, 630.2, 379.0, 976.0, 865.4, 655.1, 611.8, 169.7, 214.3, 269.2, 325.8, 330.2, 203.3, 226.1, 363.0, 426.6, 469.4, 497.0, 515.5
291.8	287.4, 294.1, 296.8, 317.8, 333.8, 334.1, 667.8, 210.3, 228.9, 254.3, 320.7, 346.5, 353.3
294.1	990.0, 468.0, 625.7, 672.8, 1298.8, 115.7, 788.9, 107.0, 287.4, 296.8, 317.8, 614.5, 333.8, 651.2, 334.1, 667.8, 210.3, 228.9, 254.3, 291.8, 320.7, 346.5, 353.3, 213.1, 530.8, 107.8, 320.8, 242.0, 372.1, 379.8, 372.2, 401.6
296.8	990.0, 468.0, 625.7, 672.8, 1298.8, 115.7, 788.9, 107.0, 287.4, 294.1, 581.5, 296.8, 333.8, 651.2, 334.1, 667.8, 210.3, 228.9, 254.3, 291.8, 320.7, 346.5, 353.3, 213.1, 530.8, 107.8, 320.8, 242.0, 372.1, 379.8, 372.2, 401.6

Table 3.3: (continued)

Gate γ-ray (keV)	Coincident γ-rays (keV)
300.4	976.0, 564.9, 611.8, 142.2
301.9	990.0, 468.0, 625.7, 672.8, 115.7, 107.0, 345.4, 500.9, 483.4, 984.2, 576.8, 546.0, 1123.0, 320.2
317.8	990.0, 468.0, 625.7, 672.8, 1298.8, 115.7, 788.9, 107.0, 287.4, 294.1, 581.5, 296.8, 591.6, 333.8, 334.1, 667.8, 210.3, 228.9, 254.3, 291.8, 320.7, 346.5, 353.3, 213.1, 530.8, 107.8, 320.8, 242.0, 372.1, 379.8, 372.2, 401.6
320.1	990.0, 468.0, 625.7, 672.8, 115.7, 107.0, 345.4, 500.9, 483.4, 984.2, 301.9, 785.9, 576.8, 546.0, 1123.0
320.7	287.4, 294.1, 296.8, 317.8, 333.8, 334.1, 210.3, 228.9, 254.3, 291.8, 546.2, 320.7, 346.5, 353.3
320.8	287.4, 294.1, 296.8, 317.8, 242.0, 372.1, 379.8, 372.2, 401.6
325.8	976.0, 655.1, 138.0, 169.7, 269.2, 330.2, 203.3, 226.1, 289.4, 363.0, 426.6
330.2	976.0, 655.1, 138.0, 169.7, 269.2, 325.8, 203.3, 226.1, 289.4, 363.0, 426.6, 469.4, 497.0
330.6	990.0, 468.0, 625.7, 672.8, 1298.8, 115.7, 788.9, 107.0, 345.4, 630.2, 379.1, 402.8, 330.6, 389.2, 976.0, 865.4, 421.1, 611.8, 142.2
333.8	625.7, 672.8, 115.7, 287.4, 294.1, 581.5, 296.8, 591.6, 317.8, 614.5, 334.1, 210.3, 228.9, 254.3, 291.8, 546.2, 320.7, 613.7, 346.5, 353.3
334.1	625.7, 672.8, 115.7, 287.4, 294.1, 581.5, 296.8, 591.6, 317.8, 614.5, 333.8, 651.2, 210.3, 228.9, 254.3, 291.8, 546.2, 320.7, 613.7, 346.5, 353.3
345.4	990.0, 468.0, 625.7, 672.8, 1298.8, 115.7, 788.9, 107.0, 630.2, 379.0, 402.8, 782.0, 330.6, 389.2, 500.9, 483.4, 984.2, 301.9, 785.9, 576.8, 546.0, 1123.0, 320.2, 242.0, 372.1, 379.8, 372.2, 401.6, 226.1, 289.4, 363.0

Table 3.3: (continued)

Gate γ-ray (keV)	Coincident γ-rays (keV)
346.5	287.4, 294.1, 296.8, 317.8, 333.8, 334.1, 210.3, 228.9, 254.3, 291.8, 320.7, 353.3
353.3	287.4, 294.1, 296.8, 317.8, 333.8, 334.1, 210.3, 228.9, 254.3, 291.8, 320.7, 346.5
363.0	379.0, 976.0, 169.7, 214.3, 269.2, 325.8, 330.2, 203.3, 226.1, 289.4, 426.6, 469.4, 497.0, 515.5
372.1	990.0, 468.0, 625.7, 672.8, 1298.8, 115.7, 788.9, 107.0, 287.4, 294.1, 581.5, 296.8, 591.6, 317.8, 614.5, 213.1, 530.8, 107.8, 320.8, 242.0, 379.8, 372.2, 401.6
372.2	990.0, 468.0, 625.7, 672.8, 1298.8, 115.7, 788.9, 107.0, 287.4, 294.1, 581.5, 296.8, 591.6, 317.8, 614.5, 213.1, 530.8, 107.8, 320.8, 242.0, 372.1, 379.8, 401.6
379.1	990.0, 468.0, 625.7, 672.8, 1298.8, 115.7, 788.9, 107.0, 345.4, 630.2, 402.8, 330.6, 389.2, 976.0, 865.4, 421.1, 611.8, 142.2, 203.3, 226.1, 289.4, 363.0
379.8	990.0, 468.0, 625.7, 672.8, 1298.8, 115.7, 788.9, 107.0, 287.4, 294.1, 581.5, 296.8, 591.6, 317.8, 614.5, 213.1, 530.8, 107.8, 320.8, 242.0, 372.1, 372.2, 401.6
389.2	990.0, 468.0, 625.7, 672.8, 1298.8, 115.7, 788.9, 107.0, 345.4, 630.2, 402.8, 782.0, 330.6, 976.0, 865.4, 611.8, 142.2
401.6	625.7, 672.8, 115.7, 107.0, 287.4, 294.1, 581.5, 296.8, 591.6, 317.8, 614.5, 213.1, 530.8, 107.8, 320.8, 242.0, 372.1, 379.8, 372.2
402.8	990.0, 468.0, 625.7, 672.8, 1298.8, 115.7, 788.9, 107.0, 345.4, 630.2, 379.1, 330.6, 389.2, 976.0, 865.4, 421.1, 611.8, 142.2
421.1	379.0, 402.8, 976.0, 444.4, 611.8, 157.3, 142.2, 169.7, 214.3
426.6	976.0, 169.7, 214.3, 269.2, 325.8, 330.2, 203.3, 226.1, 289.4, 363.0, 469.4, 497.0, 515.5

Table 3.3: (continued)

Gate γ-ray (keV)	Coincident γ-rays (keV)
444.4	976.0, 421.1, 611.8, 142.2
454.9	976.0, 865.4, 300.4, 157.3, 142.2, 169.7, 214.3, 269.2, 289.4
468.0	990.0, 107.0, 345.4, 630.2, 379.0, 402.8, 500.9, 301.9, 576.8, 320.2, 287.4, 294.1, 296.8, 317.8, 333.8, 334.1, 213.1, 107.8, 242.0, 372.1, 379.8, 372.2, 401.6
469.4	976.0, 169.7, 214.3, 269.2, 330.2, 203.3, 226.1, 289.4, 363.0, 426.6, 497.0, 515.5
482.8	976.0, 1037.3, 169.7, 214.3, 269.2, 289.4
483.4	625.7, 672.8, 115.7, 107.0, 345.4, 500.9, 301.9, 785.9, 576.8, 546.0, 320.2
497.0	976.0, 169.7, 214.3, 269.2, 330.2, 203.3, 226.1, 289.4, 363.0, 426.6, 469.4, 515.5
500.9	990.0, 468.0, 625.7, 672.8, 115.7, 107.0, 345.4, 483.4, 301.9, 785.9, 576.8, 546.0, 1123.0, 320.2
515.5	976.0, 169.7, 214.3, 269.2, 203.3, 226.1, 289.4, 363.0, 426.6, 469.4, 497.0
530.8	287.4, 294.1, 296.8, 107.8, 242.0, 372.1, 379.8, 372.2, 401.6
546.0	625.7, 672.8, 115.7, 107.0, 345.4, 500.9, 483.4, 301.9, 576.8, 320.2
546.2	333.8, 334.1, 210.3, 228.9, 320.7, 346.5, 353.3
564.9	976.0, 300.4, 611.8, 157.3, 142.2
576.8	625.7, 672.8, 115.7, 107.0, 345.4, 500.9, 483.4, 301.9, 546.0, 320.2
581.5	296.8, 317.8, 333.8, 334.1, 213.1, 107.8, 242.0, 372.1, 379.8, 372.2, 401.6
591.5	287.4, 317.8, 333.8, 334.1, 213.1, 107.8, 242.0, 372.1, 379.8, 372.2, 401.6

Table 3.3: (continued)

Gate γ-ray (keV)	Coincident γ-rays (keV)
611.8	379.0, 402.8, 330.6, 389.2, 976.0, 865.4, 421.1, 444.4, 564.9, 300.4, 142.2, 226.1, 289.4, 363.0, 426.6, 469.4, 497.0
613.7	333.8, 334.1, 210.3, 228.9, 254.3, 346.5, 353.3
614.5	287.4, 294.1, 333.8, 334.1, 213.1, 107.8, 242.0, 372.1, 379.8, 372.2, 401.6
625.7	672.8, 115.7, 788.9, 107.0, 345.4, 630.2, 379.0, 402.8, 330.6, 500.9, 483.4, 984.2, 301.9, 576.8, 320.2, 287.4, 294.1, 296.8, 317.8, 333.8, 334.1, 213.1, 107.8, 242.0, 372.1, 379.8, 372.2, 401.6
630.2	990.0, 468.0, 625.7, 672.8, 1298.8, 115.7, 788.9, 107.0, 345.4, 379.0, 402.8, 782.0, 330.6, 389.2, 226.1, 289.4, 363.0
651.2	287.4, 294.1, 296.8, 334.1, 210.3, 228.9, 254.3
655.1	976.0, 865.4, 564.9, 611.8, 169.7, 214.3, 269.2, 325.8, 330.2, 203.3, 226.1, 289.4, 363.0, 426.6, 469.4, 497.0
667.8	287.4, 294.1, 296.8, 317.8, 210.3, 228.9, 254.3, 291.8
672.8	625.7, 1298.8, 115.7, 107.0, 345.4, 630.2, 379.0, 402.8, 330.6, 500.9, 483.4, 984.2, 301.9, 576.8, 320.2, 287.4, 294.1, 296.8, 317.8, 333.8, 334.1, 213.1, 107.8, 242.0, 372.1, 379.8, 372.2, 401.6
782.0	990.0, 468.0, 625.7, 672.8, 1298.8, 115.7, 788.9, 107.0, 345.4, 630.2, 379.1, 402.8, 330.6, 389.2
785.9	500.9, 576.8, 320.2
788.9	625.7, 107.0, 345.4, 630.2, 379.0, 402.8, 500.9, 287.4, 294.1, 296.8, 317.8, 213.1, 107.8, 242.0, 372.1, 379.8, 372.2, 401.6
865.4	379.0, 402.8, 330.6, 389.2, 976.0, 611.8, 454.9, 157.3, 142.2, 169.7, 214.3, 269.2, 325.8, 330.2, 203.3, 226.1, 289.4, 363.0, 426.6, 469.4, 497.0

Table 3.3: (continued)

Gate γ-ray (keV)	Coincident γ-rays (keV)
976.0	379.0, 402.8, 330.6, 389.2, 482.8, 1037.3, 865.4, 421.1, 444.4, 564.9, 300.4, 655.1, 611.8, 454.9, 157.3, 142.2, 138.0, 169.7, 214.3, 269.2, 325.8, 330.2, 203.3, 226.1, 289.4, 363.0, 426.6, 469.4, 497.0, 515.5
984.2	625.7, 672.8, 115.7, 107.0, 345.4, 301.9, 576.8, 546.0, 320.2
990.0	468.0, 107.0, 345.4, 630.2, 379.0, 402.8, 500.9, 301.9, 287.4, 294.1, 296.8, 317.8, 333.8, 334.1, 213.1, 107.8, 242.0, 372.1, 379.8, 372.2, 401.6
1037.3	976.0, 482.8, 169.7, 214.3, 269.2, 226.1
1123.0	345.4, 500.9, 301.9, 320.2
1298.8	672.8, 625.7, 107.0, 345.4, 630.2, 379.0, 402.8, 500.9, 287.4, 294.1, 296.8, 317.8, 213.1, 107.8, 242.0, 372.1, 379.8, 372.2, 401.6

22. Similar to the total energy requirement above, these values of minimum and maximum would allow most of the events from ^{198}Bi to be recorded while rejecting about half of the events from ^{197}Bi. (See Fig. 3.2b.)

c) The minimum timing between the first BGO ball pulse and the second Ge pulse was set at channel number 306 (corresponding to about 32 ns after the average centroid from the timing spectrum of all the data). The maximum timing was set at channel number 444 (corresponding to about 10 ns before the average centroid). As mentioned earlier, since most of the γ rays from ^{197}Bi were decaying from long-lived isomeric states ($\approx$ 200 ns half-lives), this condition would further discriminate the inclusion of ^{197}Bi γ rays into the matrix.

The use of all the conditions above insured that most of the prompt events from ^{198}Bi were recorded while most of the events from other nuclei, especially those of ^{197}Bi, were rejected.

The E_γ-Timing matrix was constructed from the low-energy γ rays of the doubly coincident events and the corresponding timings between the BGO ball pulse and the second Ge pulse. The total energy and total multiplicity conditions for this matrix were the same as those for the E_γ-E_γ matrix. A third criterion for this matrix was that the energy difference between two γ rays must be at least 200 keV. The reason for this criterion is given in the following paragraph.

As mentioned on page 30 in subsection 3.2.1, the primary goal of this experiment was to search for superdeformed bands and not to measure isomeric lifetimes. Therefore, the experimental setup was not optimal for lifetime measurements. However, it was still possible to extract the lifetime of one isomeric state from the data. Due to the characteristics of HERA's Ge detectors and electronics, the timing spectra of the

γ rays were neither symmetrical nor uniform. In general, the low-energy pulses from the Ge detectors had their corresponding logic pulses arriving at the Multiplicity-Logic-Unit (MLU) a little latter than the higher-energy pulses. The MLU combined the Ge detector's logic pulses and sent the outputs to the Master Gate (MG) and the timing circuit. As discussed earlier in chapter 2, the timing pulse sent out by the MLU corresponded to the timing arrival of the second pulse (for 2γ), third pulse (for 3γ), or fourth pulse (for 4γ). Therefore, the timing of an event generally corresponded to the lower-energy γ ray. A 200-keV difference between two γ rays insured that the timing information from each event in the matrix was the timing of the lower-energy γ ray. Fig. 3.3 shows the timing spectra of the prompt γ rays (coincident with γ rays with energies at least 200 keV larger). One can see that those spectra are not symmetrical and their centroids shift from left to right as the energies increase. From these (and other) prompt spectra, a "prompt centroid v.s. energy" curve was generated, which is shown in Fig. 3.4.

Fig. 3.5 shows the timing spectra of the 116-keV peak and of the background around the 116-keV peak. From these spectra, it is clear that the 116-keV transition depopulates an isomeric state. The lifetime of a state can be calculated using the formula $\tau = t_o - \bar{t}$, where τ is the lifetime, t_o is the centroid (or first moment) of the prompt timing peak and $\bar{t}$ is the centroid of the delayed timing peak. Using the first-moment method, with the prompt centroid taken from the "prompt centroid v.s. energy" curve, a half-life of 3 ns was determined for that isomer. Thin target was used in the experiment to allow the produced compound nuclei to recoil away from the detectors. For that reason, only some fraction of the delayed γ rays were recorded. This reduced the number of counts on the delayed side of the timing spectrum, which

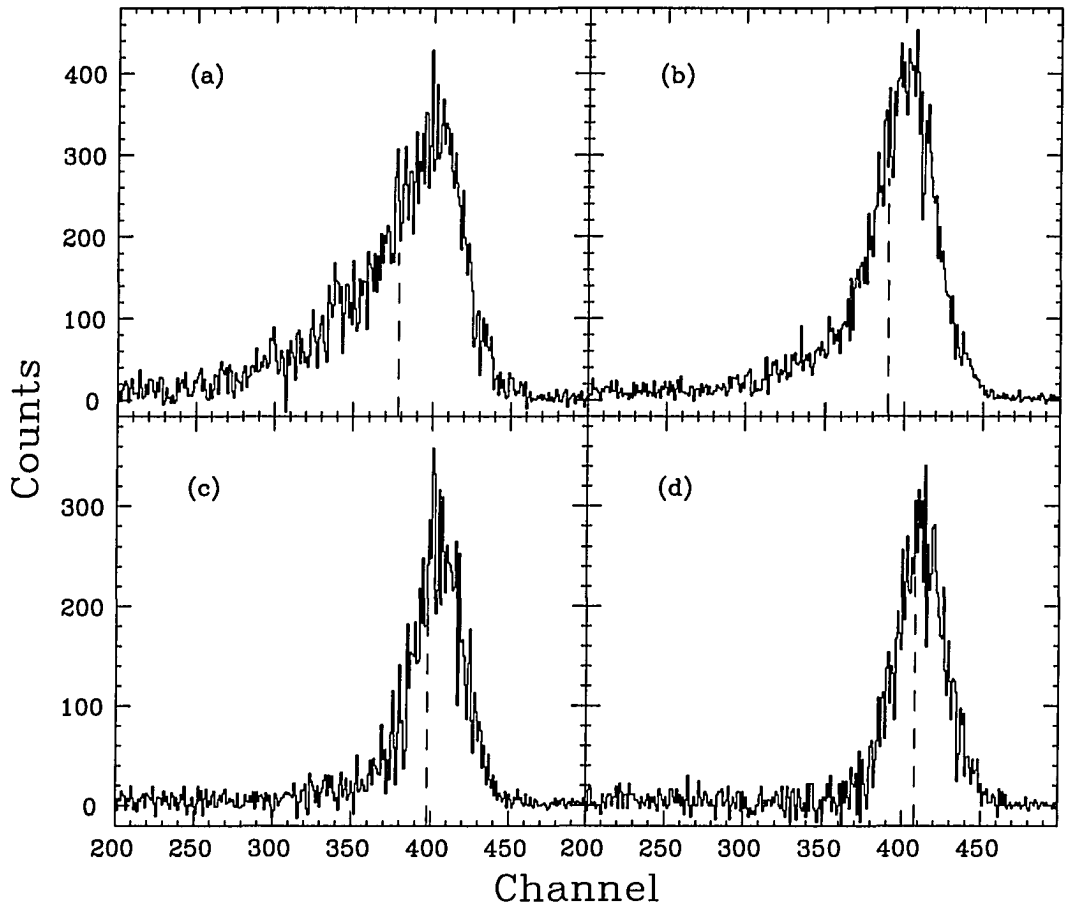

Figure 3.3: Timing spectra of prompt γ rays at different energies: (a) at 107 keV; (b) at 242 keV; (c) at 501 keV; (d) at 976 keV. The centroids calculated from channel 260 to channel 460 are presented by the dashed lines. Each channel corresponds to a time of 0.3 ns

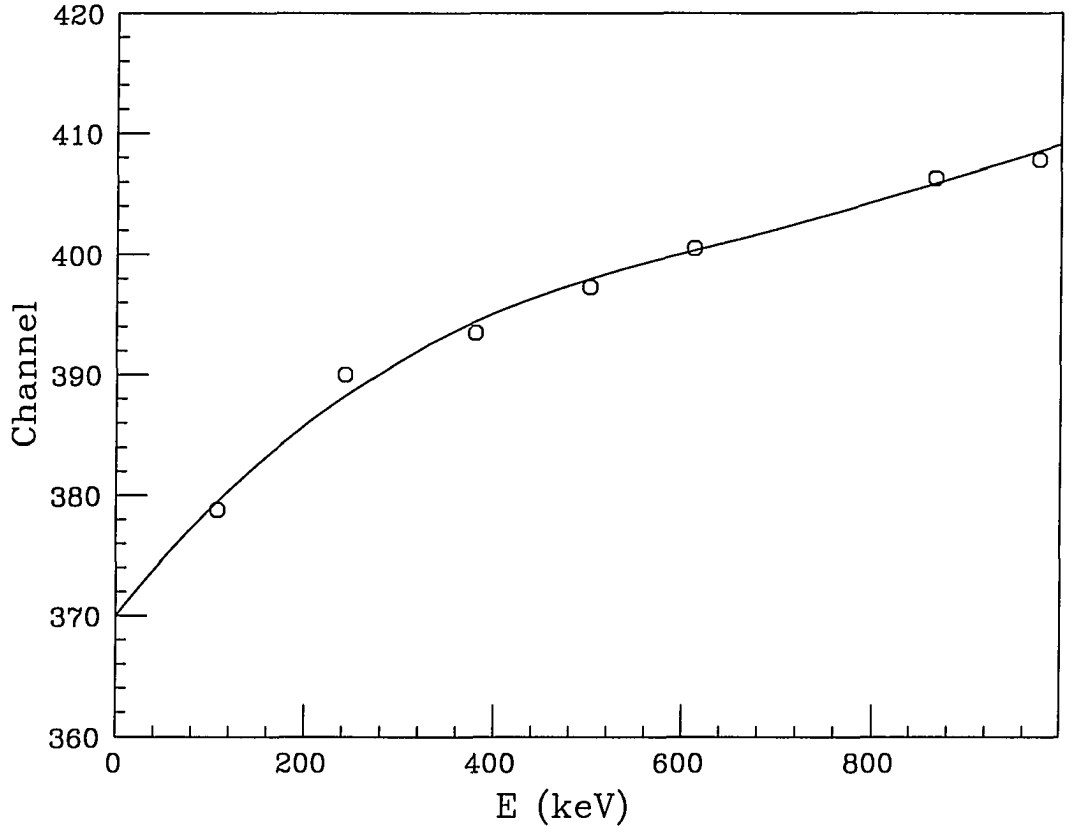

Figure 3.4: Centroids of prompt γ rays at different energies. The circles were the centroids calculated from the data. The curve was generated by fitting the data points to a third-order polynomial. Each channel corresponds to 0.3 ns

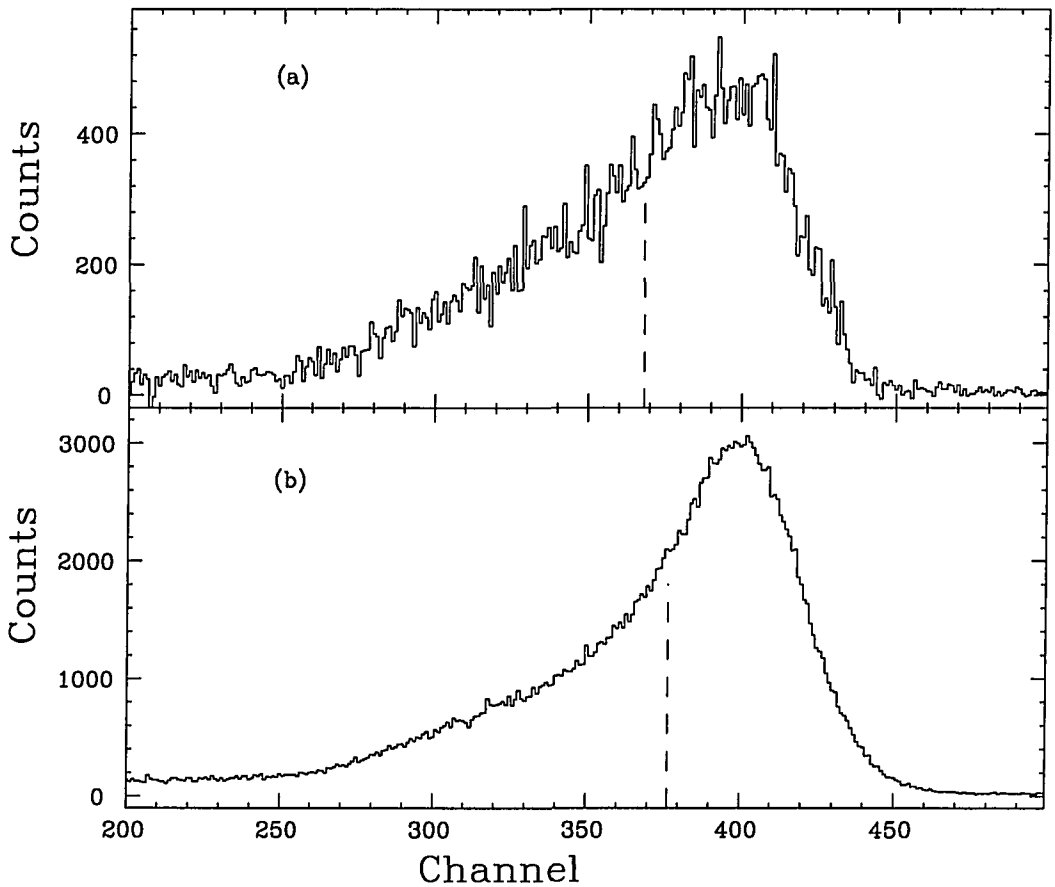

Figure 3.5: (a) Timing spectra of the 116-keV peak. (b) Timing spectra of the background around the 116-keV peak. The centroids calculated from channel 260 to channel 460 are indicated by the dashed lines

in turn made the measured lifetime too small. Therefore, the measured value of 3 ns for the isomer mention above is the lower limit of the half-life of that isomer.

The partial level scheme deduced from the present work is shown in Fig. 3.6. The 7^+ 11.85-min ground state and the 10^- 7.7-s isomer at 248.5 keV were known from a previous work [1]. The newly found isomeric state is the 14^+ state at 1663.3 keV. The placement of this state at this energy is based on arguments presented below. The spin-parity assignments of the levels are described later. Note the dashed arrows showing the feeding of the 3124-keV state from the 3944+E_2-keV and 4147+E_2-keV states, and the decaying out of the 2747-keV state with 36% of its intensity going to the 2596+E_1-keV level. These 3944+E_2-keV, 4147+E_2-keV, and 2596+E_1-keV states are described in subsection 3.2.5.

The states (at 874.5 keV and 1547.4 keV) between the known 7.7-s 10^- isomer and the newly found isomer of ^{198}Bi were determined from the crossover transitions. Examples of the crossover transitions are shown in Fig. 3.7. The spectrum in Fig. 3.7a shows the 789-keV crossover transition. In Fig. 3.7b, neither the 789-keV nor the 1299-keV transition are present since the gate is on the parallel 673-keV transition. Fig. 3.7c, gated on the 116-keV, shows the 1299-keV transition but not the 789-keV transition.

Fig. 3.8 shows the ^{198}Bi background-subtracted γ-γ coincidence spectra. The spectrum in Fig. 3.8a shows the coincident events gated on all four members of the cascade of four transitions above the 16^+ state, from the 631-keV transition to the 331-keV transition. Fig. 3.8b is gated on five members of the other cascade above the 16^+ state, from the 501-keV transition to the 320-keV transition. The low-lying transitions (transitions below the 14^+ isomer) are marked with #. The crossovers

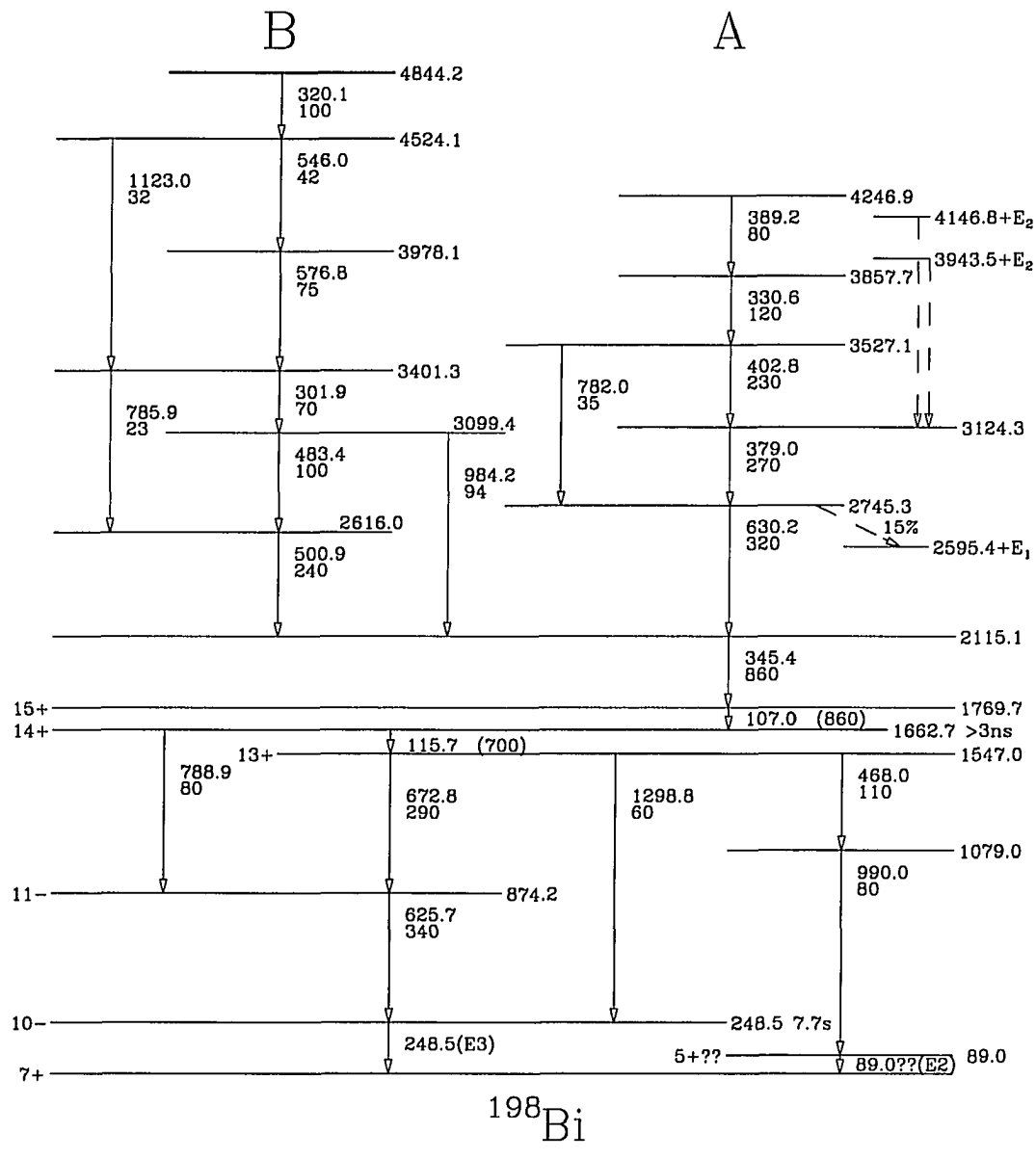

Figure 3.6: The partial level scheme of ^{198}Bi as deduced from the present investigation. The 7^+ ground state and 10^- isomeric state at 248.5 keV are taken from [1]. The 5^+ state at 89.4 keV is from [37]. The indicated values of intensities have the internal conversion coefficients included

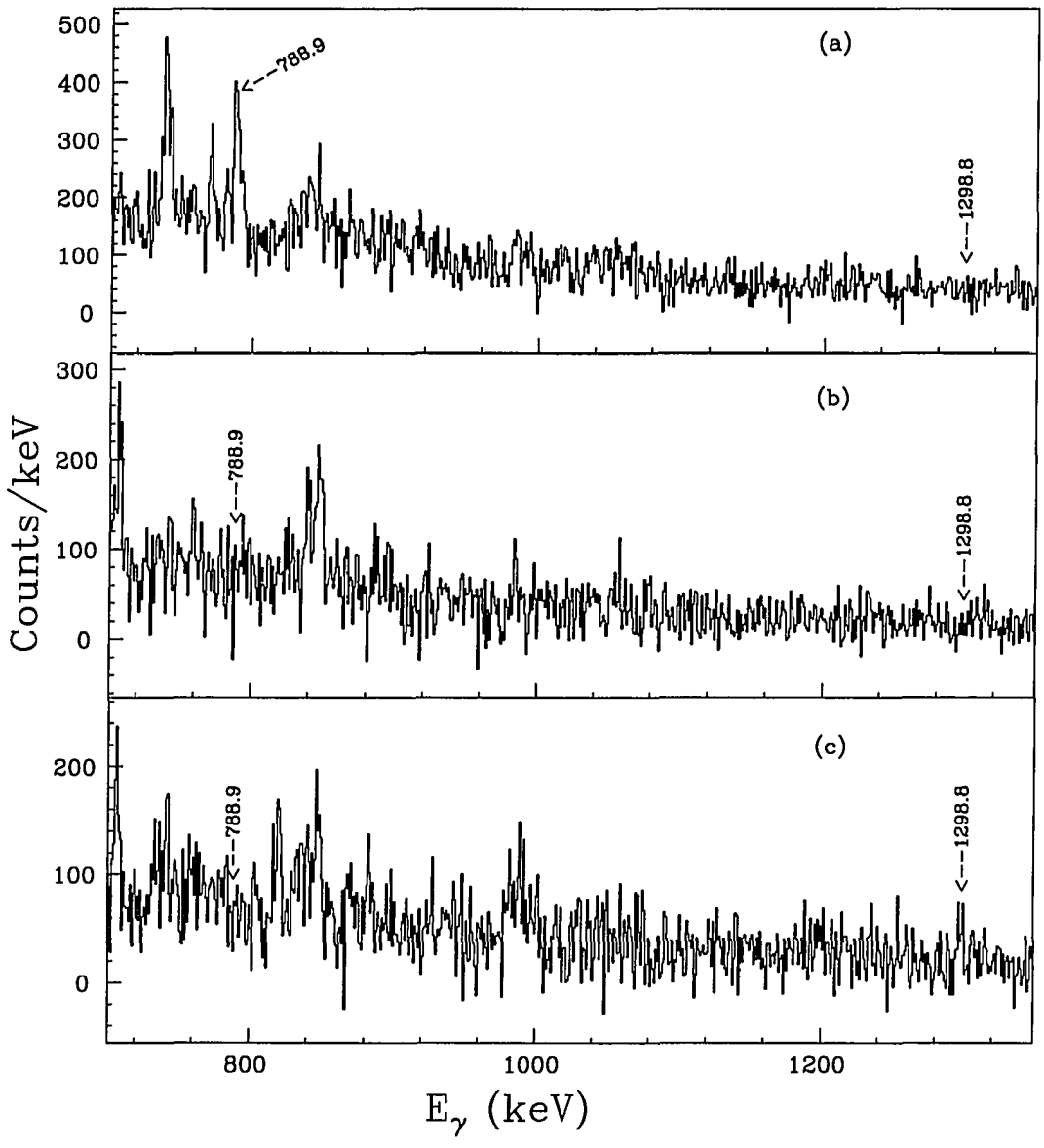

Figure 3.7: The γ-coincidence spectra gated on following transitions of the low-lying states: (a) 626 keV, (b) 673 keV, (c) 116 keV. The unmarked peaks are contaminations from nearby γ rays

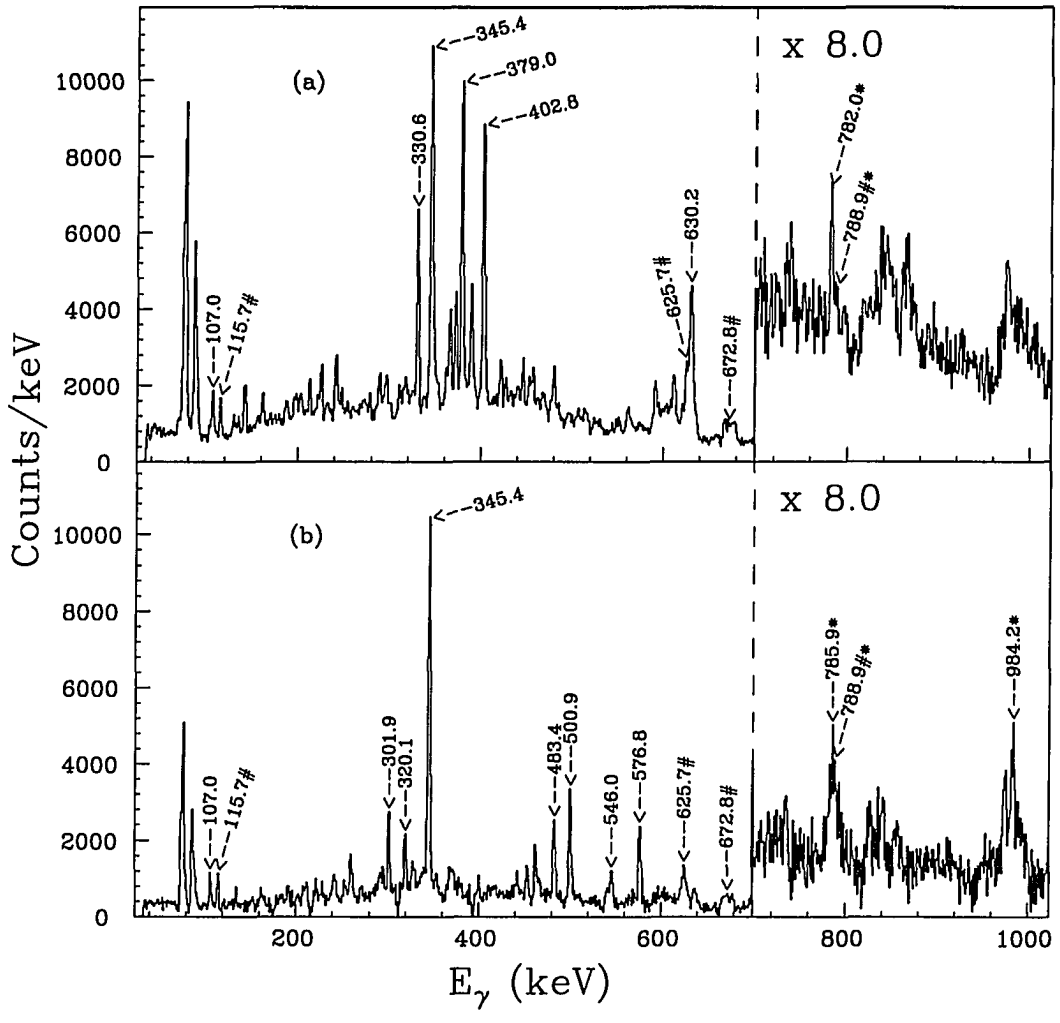

Figure 3.8: The γ-coincidence spectra gated on various members of the cascades. The low-lying transitions are marked with #, the crossovers are marked with $*$; (a) gated on 631-keV, 379-keV, 403-keV, and 331-keV transitions; (b) gated on 501-keV, 484-keV, 302-keV, 577-keV, and 320-keV transitions

are marked with $*$. The crossover transitions are very prominent in these spectra. The 789-keV transition is marked with both # and $*$ because it is both a low-lying transition and a crossover transition. Note that the two sets of gates are not in coincidence with each other but they both are in coincidence with the 346-keV, 107-keV, and the low-lying transitions.

In order to obtain a rough idea of the transition multipolarities, the angular distribution ratio R of the γ-ray yield for a particular transition in the detectors "near parallel" to the beam direction (8 detectors at angles of $\Theta = 37°$, 152° and 154°) to those "near perpendicular" to the beam direction (6 detectors at angles of $\Theta = 79°$ and 103°) was formed [33, 34]. The γ-ray yields for the γ-transitions in both sets of detectors were normalized to each other. There was no detector "perfectly parallel" or "perfectly perpendicular" to the beam direction (i.e., at angle $\Theta = 0°$ or 90°). The results for some of the clean peaks are shown in Fig. 3.9. Because of the large background and nearby peaks in the spectra, these results are only rough estimations of the mutipolarities. Any spin-parity assignments based solely on them alone should be regarded as tentative. However, it can still be seen that most of those stopover transitions probably correspond to $\Delta I = 1$ transitions rather than $\Delta I = 2$ pure quadrupoles. Note that one crossover transition at about 790 keV has the ratio $R \approx 0.5$. It is not a $\Delta I = 2$ transition but a $\Delta I = 3$ transition.

Spin-parity assignments By the observation of the systematic behaviors of the single-neutron states in the odd-A Pb isotopes and of the single-neutron and single-proton states in the heavier odd-odd Bi isotopes, and by comparison with other low-lying states of the neighboring odd-A Pb and odd-odd Bi isotopes (Figs. 3.10,

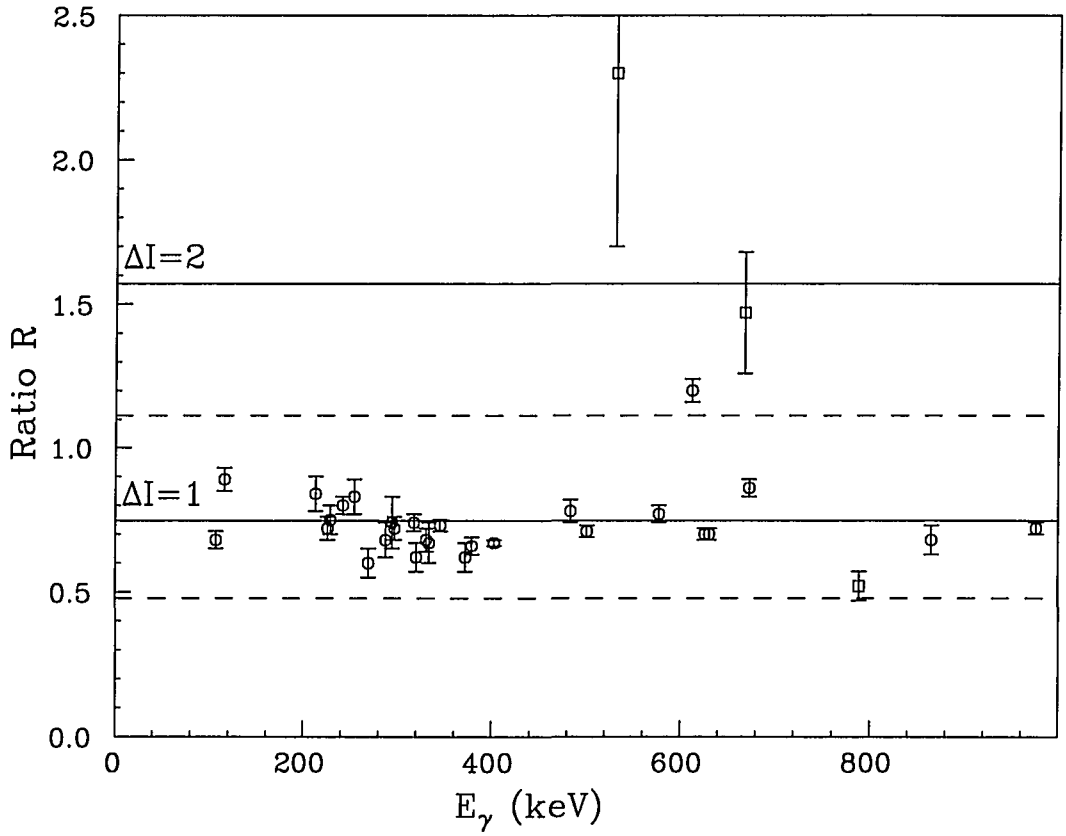

Figure 3.9: The ratio $Y_{\|}/Y_{\perp}$ for some of the clean γ-peaks in Fig. 3.6. The horizontal lines indicate the expected ratio for stretched transitions averaged over the detector angles used, assuming full alignment. Lower solid line: dipoles ($I_i = 13 \rightarrow I_f = 12$), $\delta = 0$; upper solid line: quadrupoles ($I_i = 13 \rightarrow I_f = 11$); lower dashed line: dipoles, $\delta = -0.2$; upper dashed line: dipoles, $\delta = 0.2$. Circles: stopovers; squares: crossovers

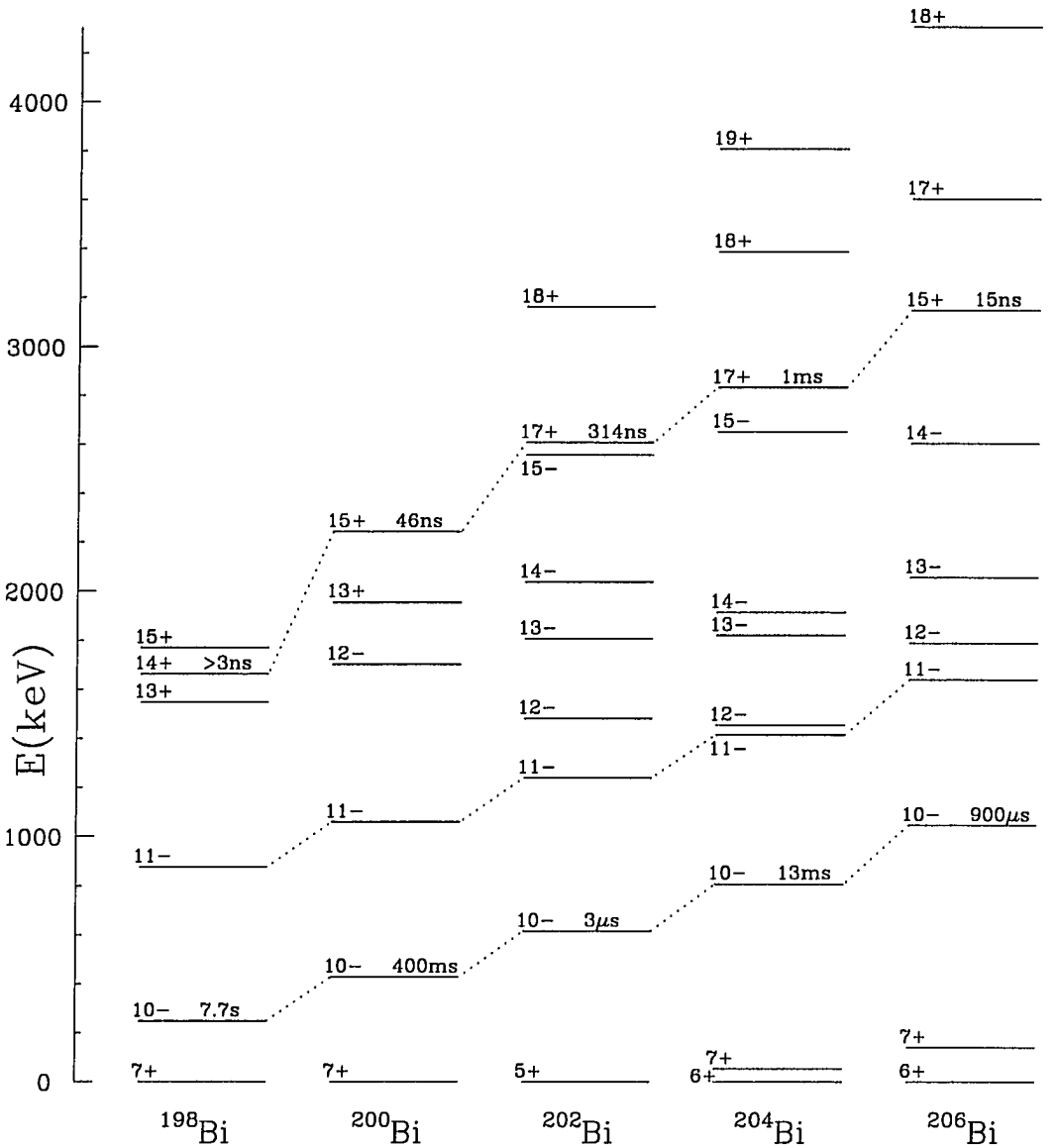

Figure 3.10: Comparison of odd-odd Bi isotopes

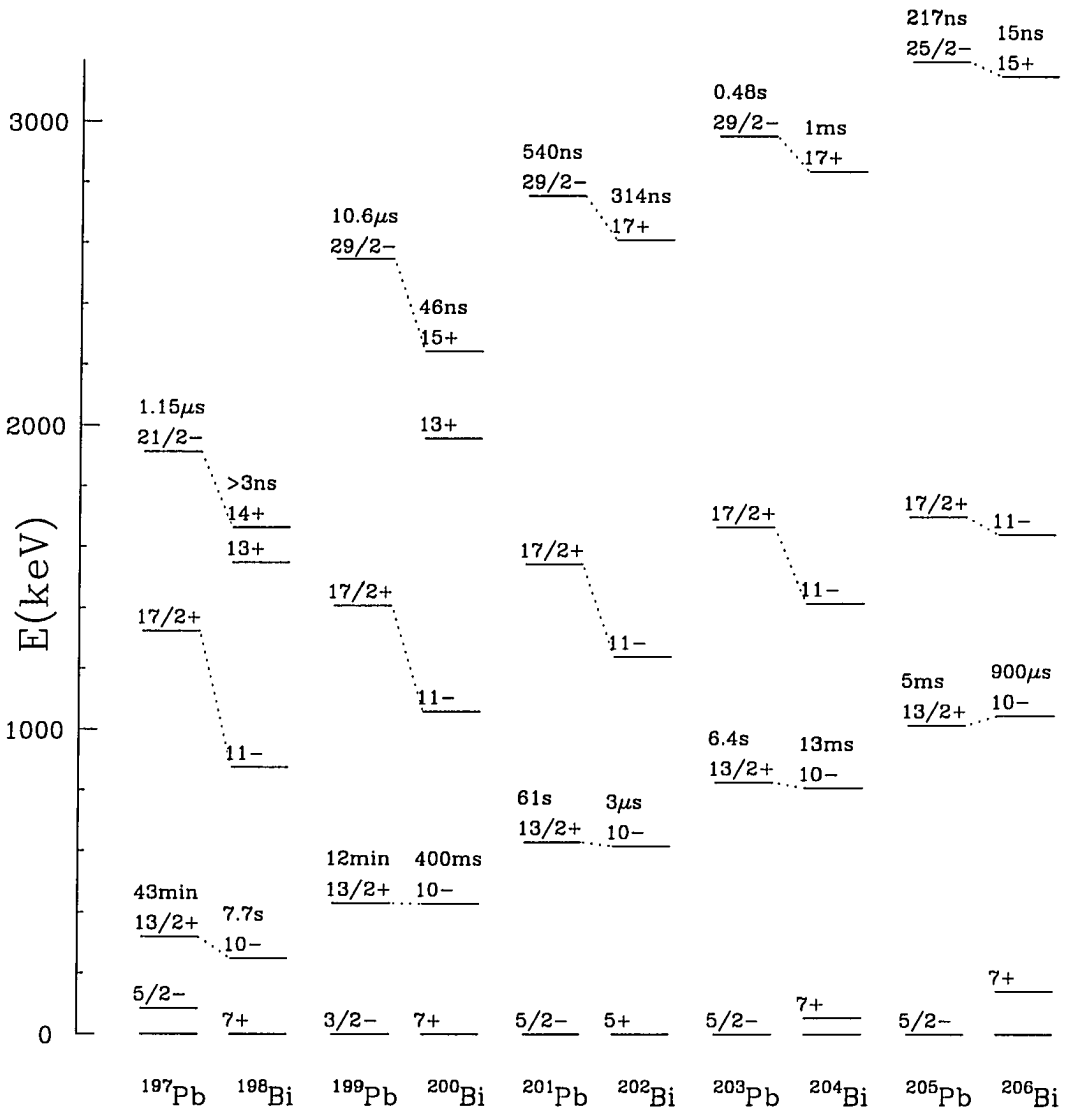

Figure 3.11: Comparison of the isomeric levels of odd-A Pb and odd-odd Bi isotopes

3.11), the spin assignments and the configurations may be deduced for some low-lying states of ^{198}Bi. Fig. 3.10 shows only a few levels of interest of the neighboring nuclei. From the level systematics of odd-odd Bi isotopes, the state at 875 keV would appear to have spin-parity of 11^- or 12^-.

To deduce spin-parity assignments, a DCO (directional correlation of γ transitions from oriented nuclei) analysis was made [35, 36]. To do this, a two-dimensional E_γ-E_γ matrix was sorted. The matrix contained coincidences between eight detectors at angles 37°/152°/154° (x axis) and six detectors at angles 79°/103° (y axis) with respect to the beam axis. The matrix was projected on the x axis and y axis respectively, while requiring the same energy gate. The intensity ratio, $I_\gamma(x)/I_\gamma(y)$, for a particular transition observed in these two spectra depends on the multipolarity of this transition and of the chosen gate. The results of the DCO ratio analysis showed that the 626-keV, 673-keV, and 116-keV transitions should have the spin differences $\Delta I = 1$, 2, and 1, respectively. The 875-keV level was thus assigned the spin-parity of 11^-. The 673-keV transition could have been either M2 or E2; however, since there was the 1299-keV crossover transition (with L = 3, presumably) competing with the 673-keV $\Delta I = 2$ transition, it was more reasonable to tentatively assign the 673-keV as M2 and the 1299-keV as E3. Therefore, the spin-parity of the 1547-keV state was assigned the value 13^+.

For the 1663-keV isomeric state, depopulated by the 116-keV transition to the 13^+ state, only M1 or E2 would have been consistent with the measured lifetime and relative intensity. If it was a pure E2 transition, then the 1663-keV level would have spin and parity of 15^+. This would have made the 789-keV transition from this level to the 875-keV 11^- level to be a M4 transition, which was very unlikely

and inconsistent with the observed lifetime. Therefore, the spin-parity of this state was assigned to be 14^+, which is consistent with both the 116-keV M1/E2 and the 789-keV E3 transitions.

In addition to those levels described above, two other transitions, 468 keV and 990 keV, are in coincidence with the 116-keV transition and other transitions above it, but not in coincidence with either the 673-keV or the 626-keV γ rays. Their placements are also shown in Fig. 3.6. It was not possible to assign the spins for these levels. It is interesting to mention that the 95±3 keV 5^+ state [37], though not satisfactorily confirmed, had been assigned to ^{198}Bi. The energy difference between the state following the 990-keV transition and the ground state is 89 keV. This energy difference is 2σ away from the value 95 keV of the 5^+ state mentioned above, thus the 89.4-keV level of Fig. 3.6 may very well be that 5^+ state of Ref. [37]. The transition from that state to the ground state was not observed because its energy was so close to the Bi X rays, its internal conversion coefficient was very large, and it might be an isomeric state with lifetime $\gg$10 ns.

Due to the large uncertainty, the 107-keV transition from the 1770-keV level to the 1663-keV level could be either M1 or E2 and still have a reasonable intensity balance with the transitions above and below it. However, the angular distribution ratio and the DCO ratio suggested it to have the spin difference $\Delta I = 1$. Therefore, the 1770-keV state was assigned the spin-parity 15^+. For other levels above the 1770-keV level (i.e., the states in the structures A and B shown in Fig. 3.6), the angular distribution and the DCO ratios gave all strong transitions, i.e., the stopover transitions, the spin difference $\Delta I = 1$. Unfortunately, the types of radiation (magnetic or electric) for those transitions were not known. From the the strong crossover transitions,

one may be tempted to assign the multipolarities of M1 to the stopover transitions (and E2 to the crossover transitions) in structure A and structure B. However, that argument is rather weak and tentative. Therefore, in this work, no spin and parity was given to those levels in structure A and structure B.

Discussion The aim of this discussion is to examine the systematic behavior of the levels in odd-odd Bi isotopes and to identify the configuration of levels in ^{198}Bi. The states in ^{198}Bi may be studied by comparing them to the states in ^{196}Pb [38], ^{197}Pb [39], ^{197}Bi [40], and some other heavier odd-A Pb (Z = 82) and odd-odd Bi (Z = 83) nuclei (^{199}Pb and ^{201}Pb [41, 42], ^{203}Pb [43], ^{205}Pb [44], ^{200}Bi [1, 45], ^{202}Bi [46], ^{204}Bi [47], ^{206}Bi [48]) since those nuclei have been studied in great detail.

It has been found that the energies calculated from any model for heavy nuclei far from a closed shell are not very reliable, especially for odd-odd nuclei. Therefore, no calculations were done for the energies of states in ^{198}Bi. Instead, in order to verify their assignments, the experimental levels and characteristics were compared with the energy levels and characteristics of neighboring nuclei. Fig. 3.12 shows the comparison of low-energy states of ^{198}Bi with the states of ^{197}Pb and ^{197}Bi. In this figure, the 3/2− and the 5/2− states of ^{197}Pb are shown as one neutron outside the ^{196}Pb core. All other states are displayed as one neutron hole ($i_{13/2}$) coupled to the ^{198}Pb core. The configurations of ^{197}Bi are given as one neutron coupled to the states of the ^{196}Pb core. Note that the configurations of the states in ^{196}Pb are very similar to those in ^{198}Pb.

In the shell-model, most of the states in ^{197}Bi may be described as a proton in the $\pi h_{9/2}$ orbital coupled to the yrast $0^+, 2^+, 4^+, 5^-, 7^-, 9^-$, and 12^+ states in the

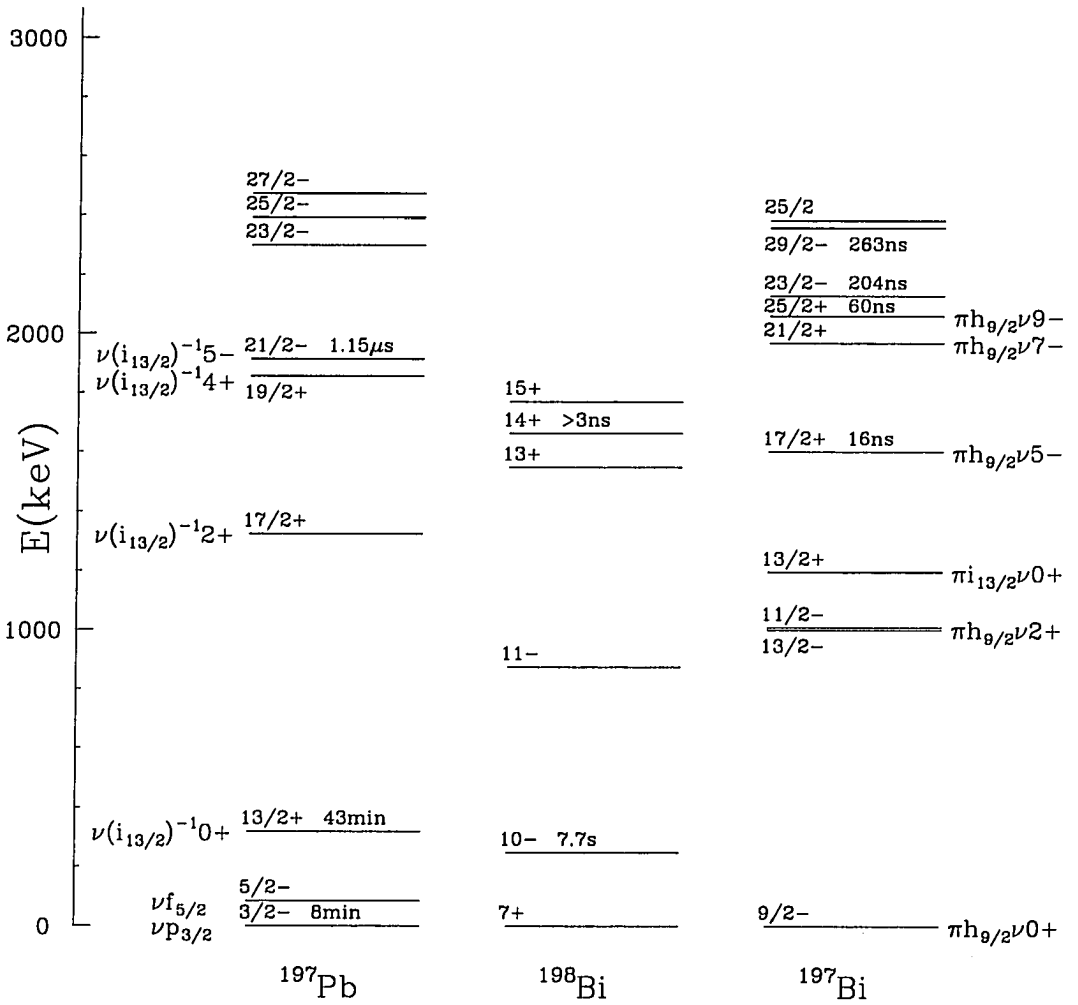

Figure 3.12: Level scheme and configurations of ^{198}Bi. For comparison, the levels and configurations of ^{197}Pb and ^{197}Bi are shown

even-A ^{196}Pb core (see Fig. 3.12). Similarly, some of the ^{198}Bi states shown could be described as a proton orbital (perhaps $\pi h_{9/2}$) and either a neutron orbital (perhaps $\nu i_{13/2}$) coupled to the yrast states in a ^{196}Pb core or a neutron-hole orbital coupled to the yrast states in a ^{198}Pb core. Alternatively, the states in ^{198}Bi could be described as either a proton orbital coupled to ^{197}Pb or a neutron orbital coupled to ^{197}Bi.

From the ^{197}Bi level structure shown in Fig. 3.12, one can see that it is much easier to excite the ^{196}Pb core than to excite one odd proton, because all states but one below 2.4 MeV have the same $h_{9/2}$ proton, whereas there are three closely spaced neutron orbitals in ^{197}Pb. This should also hold for ^{198}Bi (with the same proton number and an extra neutron). Therefore, in this work, the states in ^{198}Bi are going to be built up from the states in ^{197}Pb, i.e., $^{198}\text{Bi} = {}^{197}\text{Pb}\otimes\pi$. In previous works [39, 41], excited states in odd-A Pb nuclei in this region were attributed to the coupling of a neutron hole, mainly $i_{13/2}$, with the known states of the adjacent even-A core nucleus. Consequently, the states in ^{198}Bi are going to be described as a proton orbital and a neutron-hole orbital coupled to the yrast states in the ^{198}Pb core.

The configurations of the 7^+ ground and 10^- isomeric states in ^{198}Bi were already known [1]. They are respectively $\pi h_{9/2}\nu f_{5/2}0^+$ and $\pi h_{9/2}\nu i_{13/2}0^+$. In other heavier odd-odd Bi isotopes [47], the 11^-, 12^- and 13^-, and 14^- states were assigned the configurations $\pi h_{9/2}\nu i_{13/2}^{-1}$ coupled to the 0^+, 2^+, and 4^+ of the even-A Pb core, respectively. From this, the 11^- in ^{198}Bi may be assigned the configuration $\pi h_{9/2}\nu i_{13/2}^{-1}0^+$. However, a systematic comparison between the 11^- states in odd-odd Bi and the $17/2^+$ states in neighboring odd-A Pb isotopes shows that the 11^- Bi states should have the configuration of a $h_{9/2}$ proton coupled to the $17/2^+$ state of

Pb (which is $\nu i_{13/2}^{-1}2^+$). Therefore, the 11^- state in ^{198}Bi should instead be assigned the configuration $\pi h_{9/2}\nu i_{13/2}^{-1}2^+$ (although this configuration may also be mixed with the $\pi h_{9/2}\nu i_{13/2}^{-1}0^+$ configuration).

For the 13^+ and the isomeric 14^+ states of ^{198}Bi, comparison with other odd-odd Bi isotopes was not helpful. A detailed study of Fig. 3.12 shows that the configuration $\pi i_{13/2}\nu i_{13/2}^{-1}2^+$ as well as $\pi h_{9/2}\nu i_{13/2}^{-1}5^-$ could be possible configurations for these two states. From ^{197}Bi [40], the proton excitation energy from the $\pi h_{9/2}$ orbital to the $\pi i_{13/2}$ orbital was found to be relatively large ($\approx$ 1200 keV). The study [39] of ^{197}Pb showed that the energy difference between the $\nu(i_{13/2}^{-1}5^-)_{21/2-}$ and the $\nu(i_{13/2}^{-1}2^+)_{17/2+}$ was about 600 keV, which is just slightly less than the energy separation between the 1547- and 1663-keV levels and the 875-keV 11^- level. Therefore, the 13^+ and 14^+ in ^{198}Bi are likely to be the configuration $\pi h_{9/2}\nu i_{13/2}^{-1}5^-$. This assignment would also explain the 14^+ isomeric state since this state corresponds to the $21/2^-$ isomeric state in ^{197}Pb and the 5^- isomeric state in ^{198}Pb. For this assignment, the observed sequence in ^{198}Bi is that the 13^+, or $J_{max} - 2$, state is lower in energy than the 14^+, or $J_{max} - 1$, state. If the observation that the $\pi h_{9/2}\otimes$ odd-A Pb level gives the configuration of the level in the Bi isotone (with A+1) of the low-lying states (up to the positive-parity isomeric level) were applied for other Bi isotopes (which was not always done [47, 48]), then the pattern that emerges is that for the states in ^{202,204,206}Bi (especially the positive parity isomeric state), the lower energy states are usually the $J_{max} - 2$ state (see Fig. 3.11). ^{198}Bi also appears to follow this pattern. Note also that the ratio of the lifetimes of the $13/2^+$ isomeric state to that of $21/2^-$ state of ^{197}Pb is similar to the lifetime ratio of the 14^+ and 10^- states in ^{198}Bi. Similar ratios are also found in the ^{199}Pb-^{200}Bi, ^{203}Pb-^{204}Bi, and ^{205}Pb-^{206}Bi pairs (see Fig.

3.11).

3.2.3 High-energy states of ^{198}Bi

The analysis of the γ-γ coincidence data yielded more than 30 other $\Delta I = 1$ transitions and about 10 $\Delta I = 2$ transitions, which seemed to fall into groups of M1 band structures. These bands could be unambiguously assigned to ^{198}Bi due to the fact that they all are in coincidence with the low-lying transitions in ^{198}Bi. There are a total of four rotational band structures. There are two "regular" bands, one backbending band, and one "irregular" band. A regular band is a band that has its transitional energies gradually increase as the spins increase. An irregular band can have its transitional energies varied without following any rule. A backbending band may be thought of as two regular bands with different moment of inertia merging to form one band. At the merging (or crossing) point, the transitional energies decrease as the spins increase.

The irregular band and two regular bands are interconnecting with each other and their decay paths go through the 14^+ isomeric state. Most of its intensity goes to the 7^+ ground state through a cascade of γ rays. Note that the low-spin states discussed in the subsection 3.2.2 were from the excitations of the neutrons. In this subsection, only the interconnecting irregular and two regular bands (which are named C, D, and E, where band D is irregular and bands C and E are regular) are discussed. The remaining rotational band has the backbending property, and it only decays weakly to the 14^+ isomeric state. This backbending band will be discussed in a later subsection.

Fig. 3.13 shows the transitions of bands C, D, and E, together with the low-lying

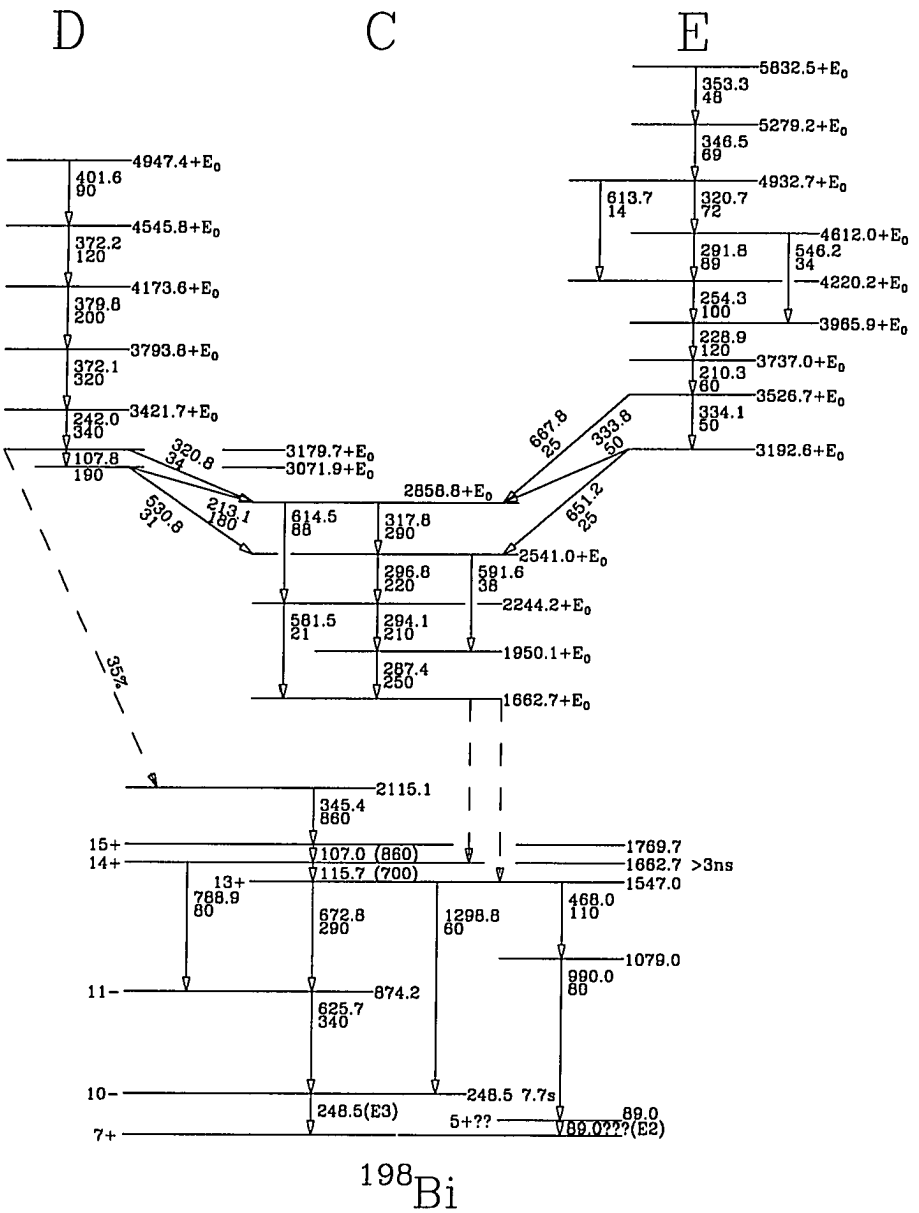

Figure 3.13: Partial level scheme of bands C, D, and E

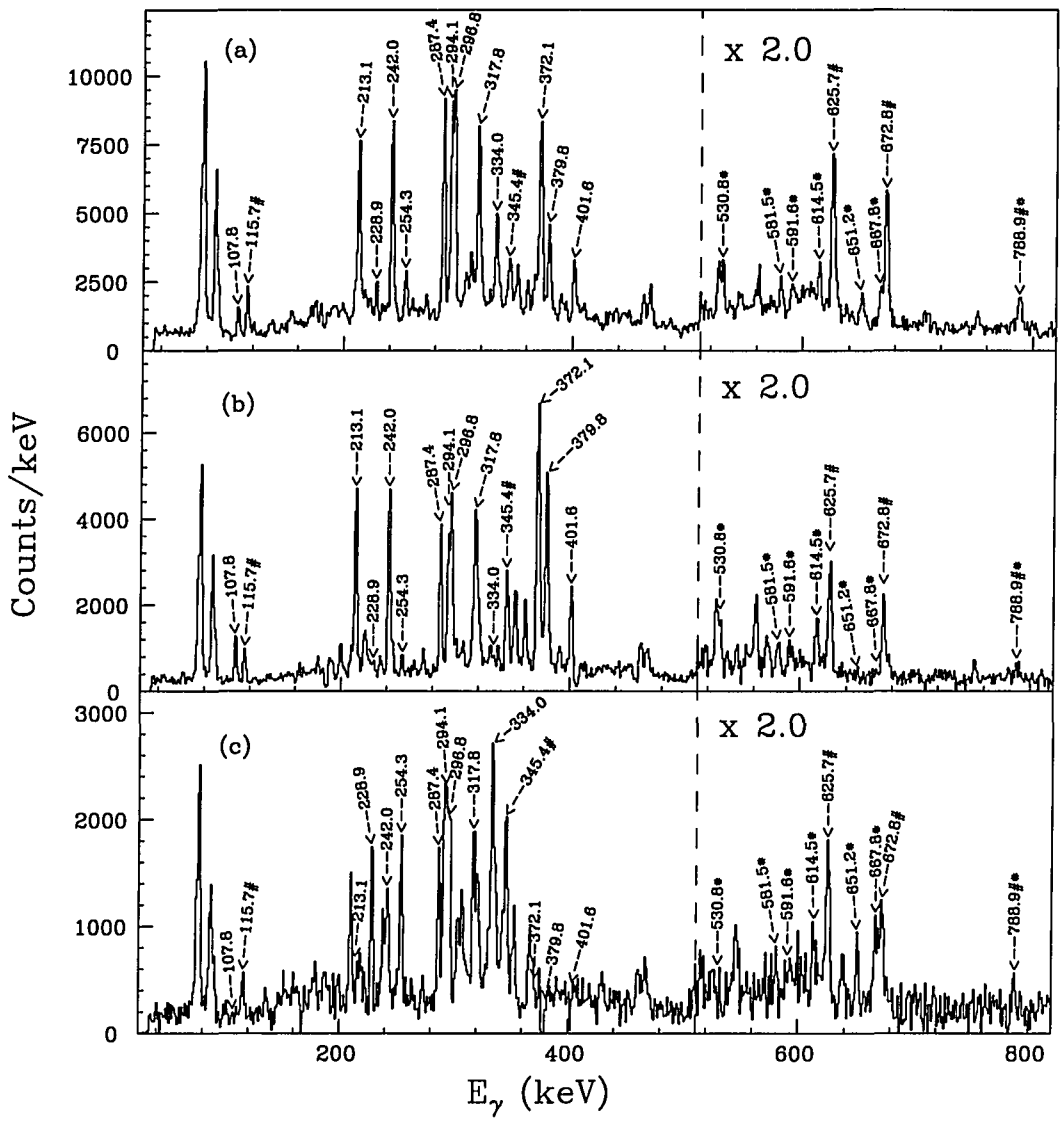

Figure 3.14: The γ-coincidence spectra gated on various member of the cascades. The low-lying transitions are marked with #, crossovers are marked with $*$; (a) gates on all members of band C; (b) gates on 242-keV and 372-keV transitions of band D; (c) gates on 334-keV, 254-keV, and 229-keV transitions of band E

transitions in ^{198}Bi. The spectrum in Fig. 3.14a is that of coincident events gated on all four M1 members of band C. Most of the crossover transitions are seen clearly and are very intense. All the members of bands D and E are also seen to be in coincidence with band C. This band feeds the 14^+ isomeric level and the connecting transitions were not found. Fig. 3.14b is gated on the 242-keV and 372-keV transitions of band D. These transitions are in coincidence with both band C and the transitions below the 2116-keV level. Band E, gated on the 334-, 254-, and 229-keV transitions, is shown in Fig. 3.14c. The intensity of this band is much weaker than those of band C and band D. Band E also feeds the top level of band C.

Either band D or E can be combined with band C to make one band out of the two groups. From the intensities of band C and band D, one could be tempted to combine these two bands into one, but from the transitional-energy point of view, bands C and E should instead be one band. The transition energies of these two bands, which are regular, are not very different from one another. All the M1 transitions in these two bands (13 total) have energies between 211 keV and 354 keV. Therefore, those two bands, C and E, are merged together and, from now on, will be denoted as band CE. Fig. 3.15 shows the transitions of band CE together with the low-lying transitions. Note the backbending at the merging point of the two bands (C and E). Fig. 3.16 shows the spins of band CE compared to other regular and backbending bands of the neighboring nuclei.

The spins of band CE are not known and they were arbitrarily adjusted to closely match those of band 1 in ^{199}Pb for comparison in Fig. 3.16. One may see that this band, at least the section above the backbend, resembles the ^{199}Pb band to some degree. Note that the spins of this band can not be arbitrarily adjusted any lower to

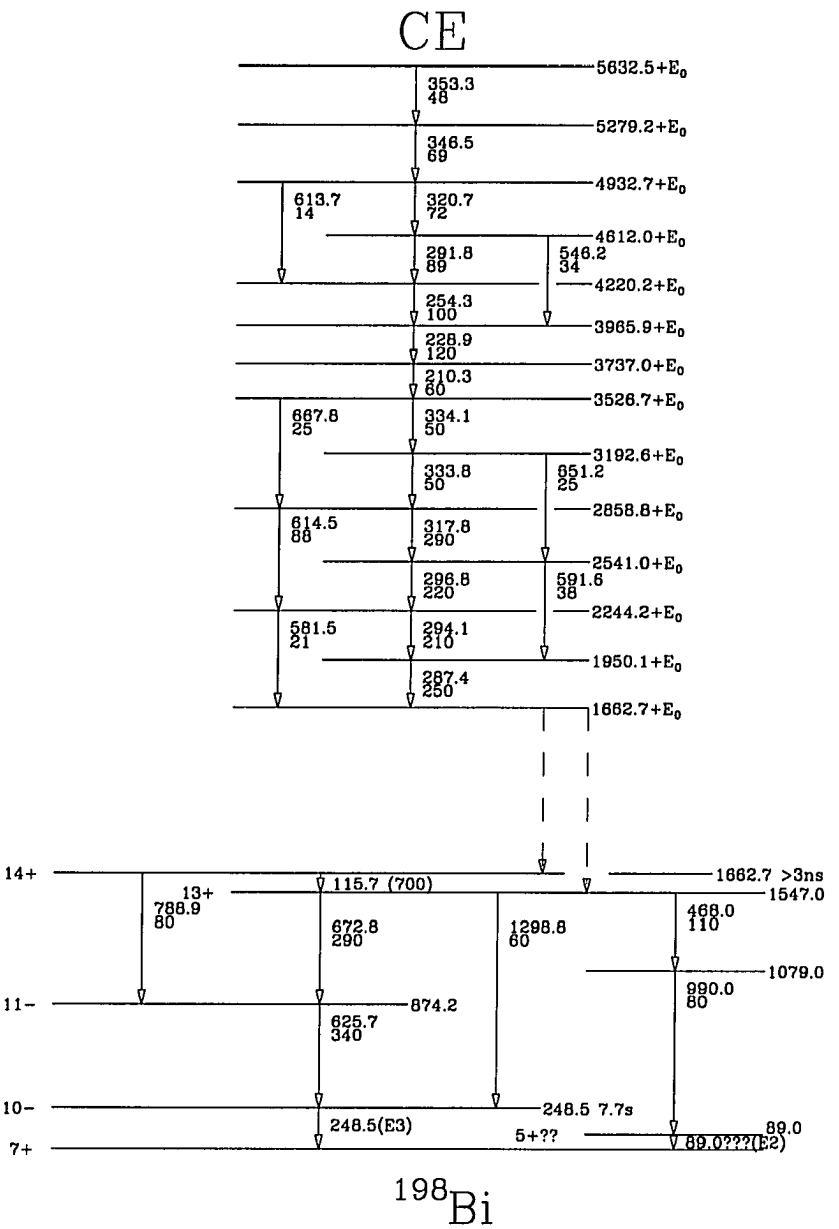

Figure 3.15: Partial level scheme of band CE

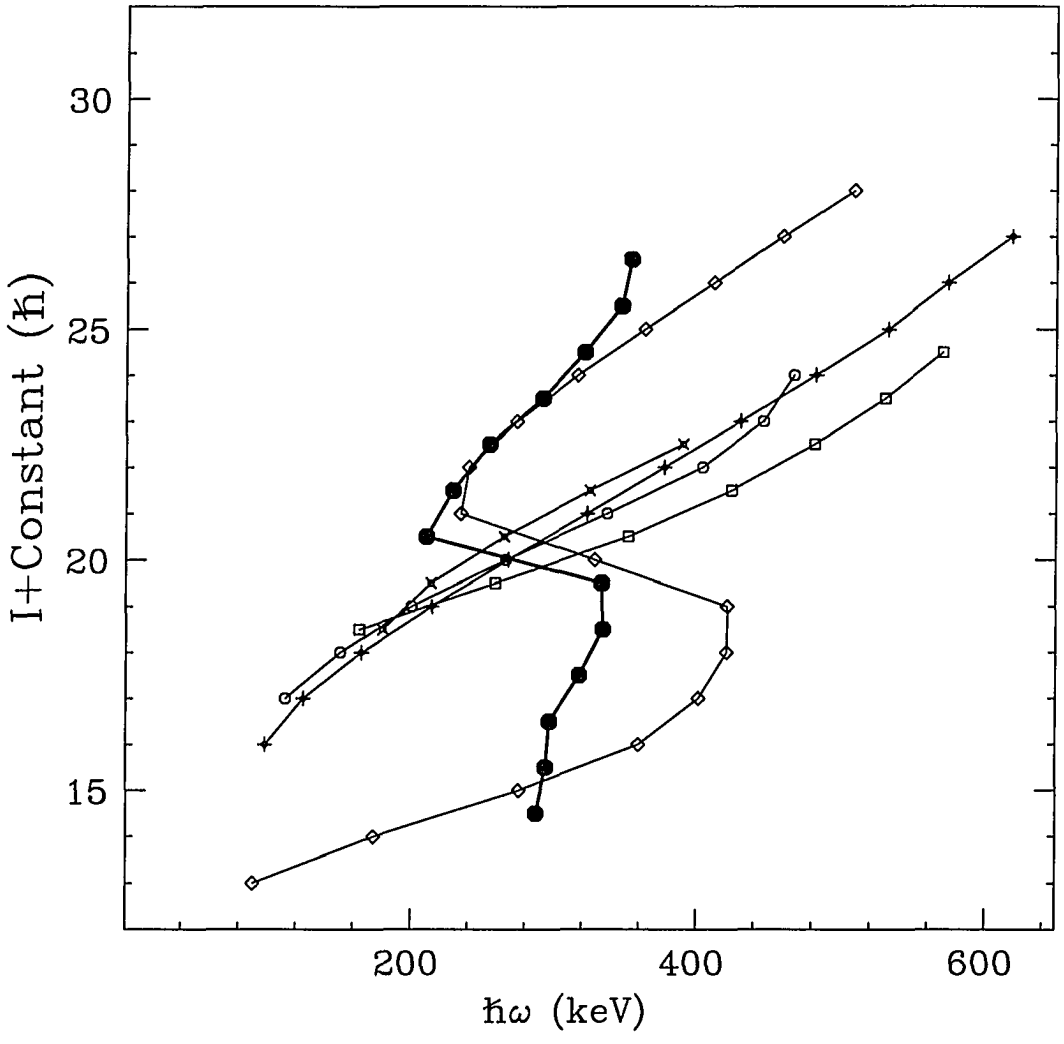

Figure 3.16: Spins of band CE compared to those of the neighboring nuclei. Closed circles: the regular band in ^{198}Bi; open square: band 1 in ^{202}Bi; diagonal crosses: band 2 in ^{202}Bi; open diamonds: band 1 in ^{199}Pb; vertical crosses: band 2 in ^{199}Pb; open circles: the regular band in ^{197}Pb. The spin for each transition is the average value of the upper and lower spins for that transition

match those of other bands shown in Fig. 3.16 because it decays to the 14^+ isomeric state and its band-head already has the spin value of 14. Also note the section of the band below the backbend where the transitional energies are almost constant; this property of this band is not understood.

3.2.4 Oblate collective band in ^{198}Bi

Analysis of the DCO ratios, with the gates set on the lowest four transitions in band CE, is consistent with a stretched-dipole character for the stopover transitions. The measured DCO ratios of the transition intensities in band CE and band D, together with the low-lying transitions below the 14^+ state, are shown in Fig. 3.17. These ratios are consistent with either the expected values for $\Delta I = 1$ with the mixing ratio $\delta = 0$ or the expected values for $\Delta I = 2$ for gates on $\Delta I = 1$ transitions. Furthermore, from the strong crossover transitions, one can safely assume M1 transitions for the main members of the bands.

There are few other irregular bands found in the A=200 region: 193Hg [49], 196Hg [50], ^{194}Pb [51], ^{197}Pb [52], ^{195,197}Tl [53], and more; few other regular bands: ^{196}Pb [54], ^{197}Pb [52, 55], ^{198}Pb [56], ^{199}Pb and ^{200}Pb [57], ^{201}Pb [58], 202Bi [59]; and one backbending band: ^{199}Pb [60]. A common feature for all these bands is that all have very strong $\Delta I = 1$ transitions leading to $B(M1)/B(E2)$ ratios of about 20 $\mu_N^2/(eb)^2$. The $B(M1)/B(E2)$ ratio was calculated using [61]

$$B(M1)/B(E2) = 0.697[E_\gamma(\Delta I = 2)]^5/[E_\gamma(\Delta I = 1)]^3\lambda(1+\delta^2) \quad \mu_N^2/(\mathrm{eb})^2$$

with λ = branching ratio $I_\gamma(\Delta I = 2)/I_\gamma(\Delta I = 1)$ and δ is E2 to M1 mixing ratio. Because of poor statistics, the mixing ratio δ could not be determined accurately from the data. However, in the neighboring nuclei, the mixing ratios of the bands

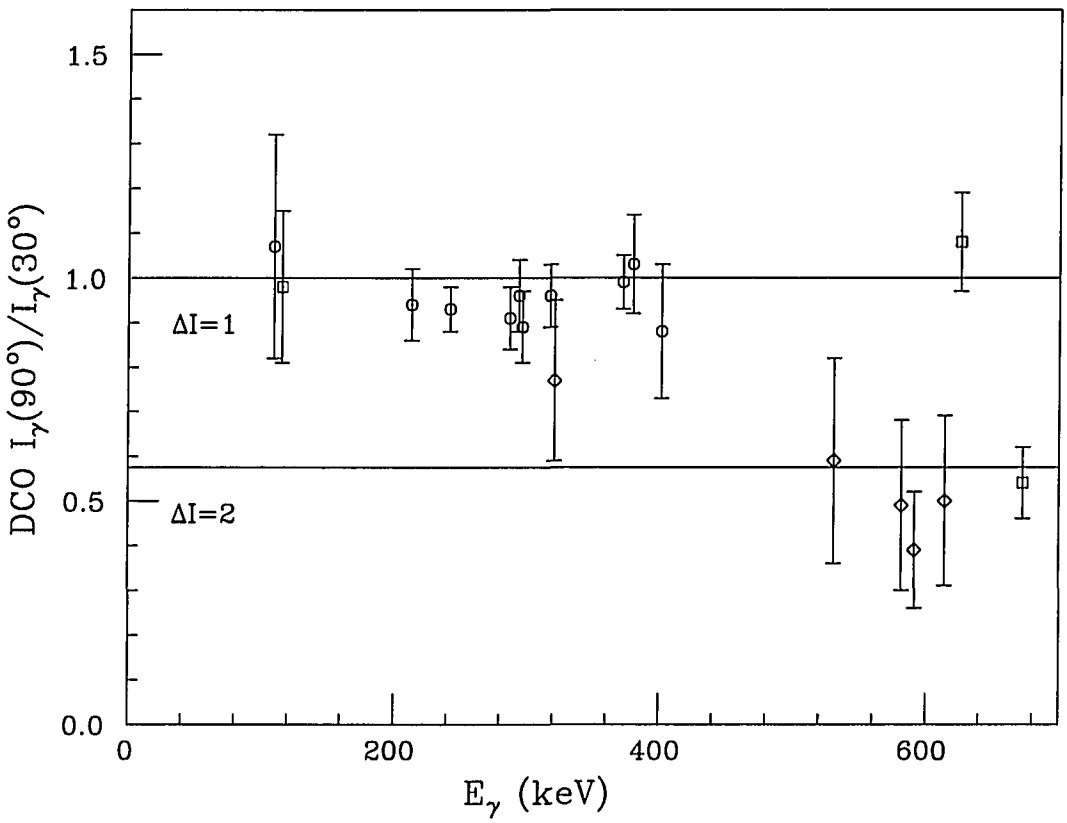

Figure 3.17: DCO ratio for the transitions in bands D and CE, and for low-lying transitions in ^{197}Pb. The energy gates are set on the four lowest M1 transitions of band CE. The solid lines are the expected ratios for $\Delta I = 1$ (top line) and $\Delta I = 2$ (bottom line). Circles: band CE and band D stopovers; squares: low-lying transitions; diamonds: crossovers

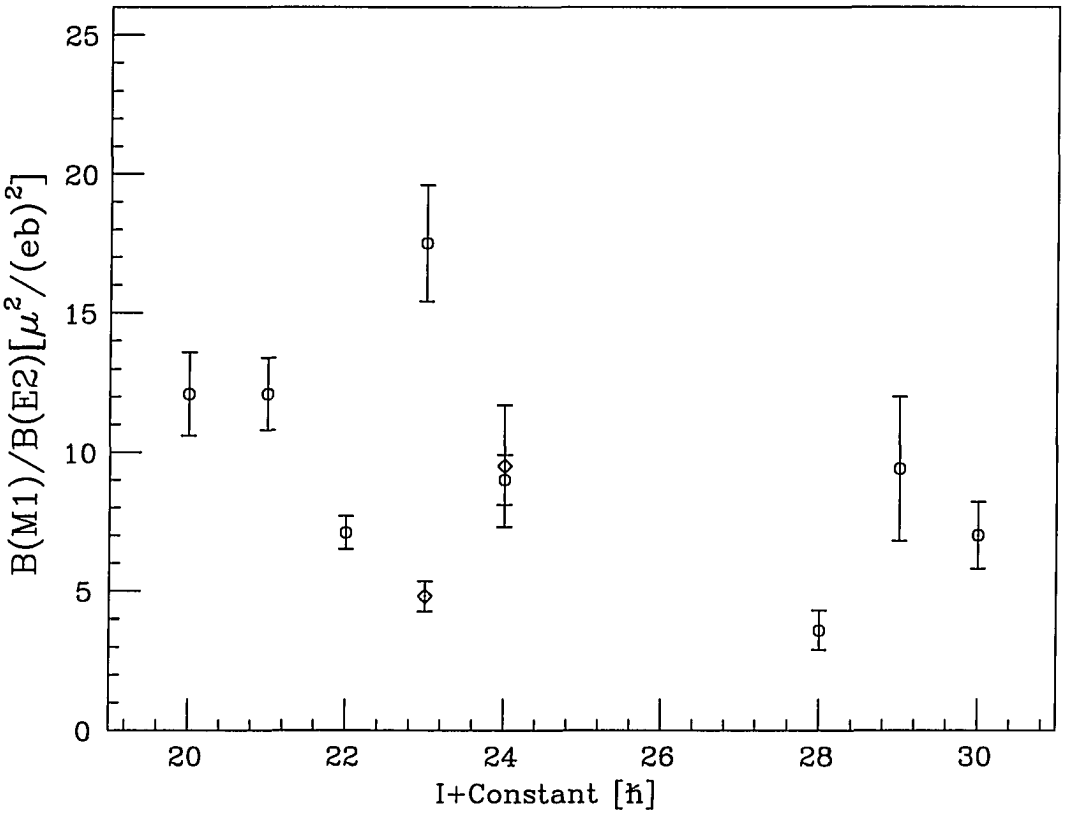

Figure 3.18: $B(M1)/B(E2)$ ratios for the observed crossover transitions in bands CE and D. Circles: band CE; diamonds :band D

appeared to be small [51, 52, 53]. Therefore, δ was assumed to be small, i.e., $\delta^2 \ll 1$, and it was assumed to be zero in the calculations of $B(M1)/B(E2)$ ratios for the ^{198}Bi. The $B(M1)/B(E2)$ ratios of band CE and band D are somewhat less than the average of about 20 $\mu_N^2/(eb)^2$. They are presented in Fig. 3.18.

These bands, CE and D, show the characteristics of collective bands (i.e., the transitions are a sequence of $\Delta I = 1$ γ rays, and the observed $B(M1)/B(E2)$ ratios are large). However, as explained in Ref. [52], the irregular bands are not typical

collective bands because of the strong irregularities between the spins and the transition energies. It was suggested in Ref. [52] that the irregular bands could be triaxial rotational bands built on the same general configurations as for the regular collective bands, or that these irregular bands have smaller β deformation than the regular bands. This suggestion can not be confirmed by the present data for ^{198}Bi. The discussion of the regular band CE is in the next subsection, 3.2.5.

3.2.5 Low-energy levels from proton excitation and the oblate dipole band

New low-energy levels (different from the levels shown in Fig. 3.6) and another oblate dipole band were found to belong to ^{198}Bi. The partial level scheme of these levels and the new backbending band is shown in Fig. 3.19. The connecting transitions from this new band to the new low-energy states and the states in Fig. 3.6 are not known. Those connecting transitions are denoted by dashed lines.

Low-lying levels from proton excitation in ^{198}Bi Since the first proton excitation energy from the $\pi h_{9/2}$ ground state to the $\pi i_{13/2}$ state is relatively large, not many states resulting from proton excitation have been reported for Bi isotopes in earlier works. All the known states in odd-odd Bi nuclei in this region have been interpreted as one, two, or three excited neutrons coupled to the $\pi h_{9/2}$ lowest proton energy level [1, 38, 39, 40, 41, 43, 44, 45, 46, 47, 48]. In the present subsection, the low-lying states of ^{198}Bi (different from the states reported in subsection 3.2.2), which are believed to come from the excitations of a proton, are reported. The gated spectrum is shown in Fig. 3.20. This spectrum is gated on the 976-keV transition,

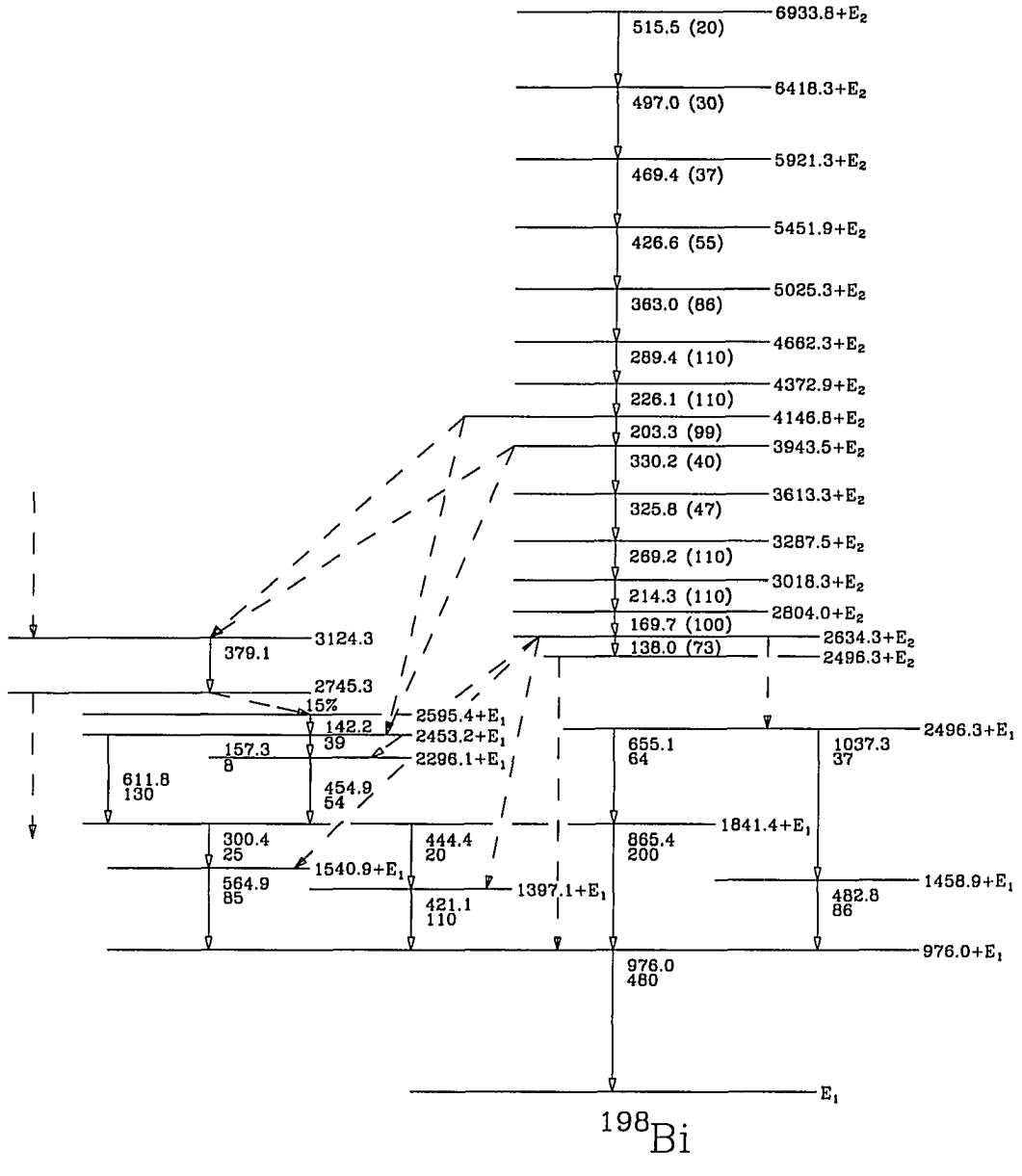

Figure 3.19: Partial level scheme for ^{198}Bi showing the backbending band and the connecting low-lying transitions

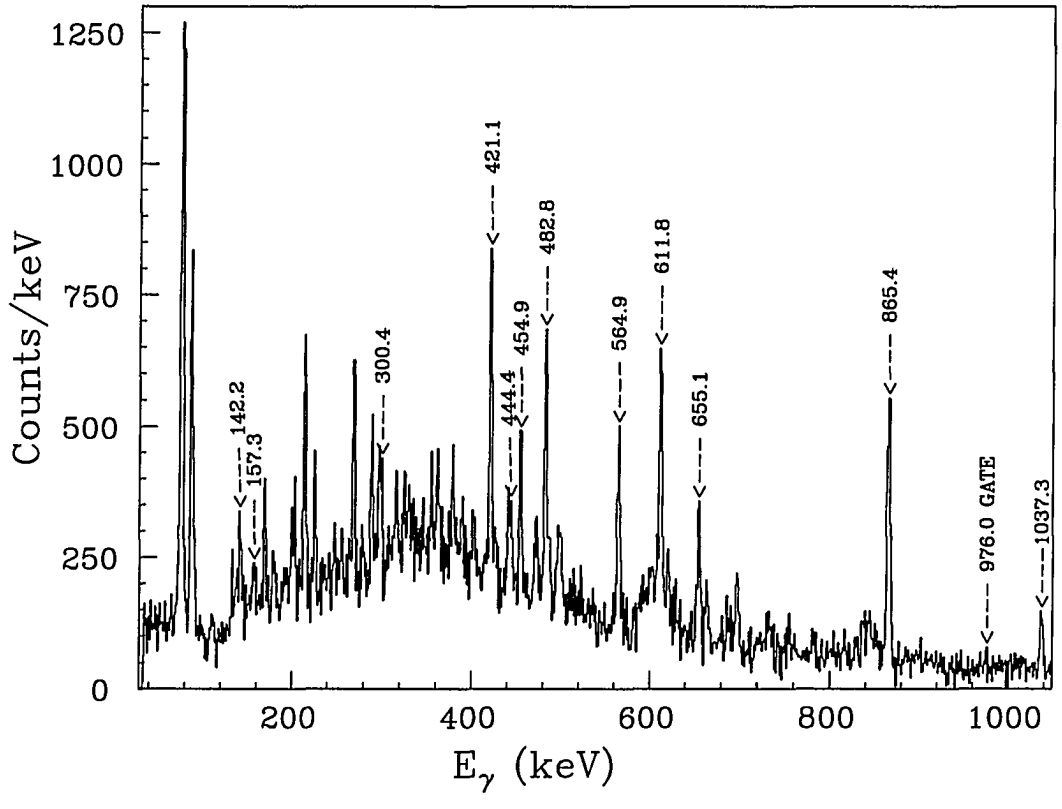

Figure 3.20: The γ-coincidence spectrum gated on the 976-keV transition. The energies of the members of the cascades are shown. The unmarked peaks are from the backbending band which decays to these low-lying levels

which is the lowest transition for these cascades. These transitions are assigned to ^{198}Bi based on the same kinds of arguments as discussed in subsection 3.2.1 and on the feeding of the 2747 keV level (which also decays through the 14^+ isomeric state mentioned earlier). These transitions are not in coincidence with the low-lying states of ^{198}Bi discussed earlier. This evidence suggests these cascades may be excited by a completely different process than just neutron excitations. These levels may be the excitations of the odd proton in ^{198}Bi coupled to one or more quasineutrons. However, it was not possible to assign the spins and configurations for these levels. The 976-keV transition is the lowest and strongest transition of these cascades. It may be that the state below this 976-keV transition is the 7^+ ground state. However, due to characteristics of HERA which did not detect low-energy γ rays or γ rays decaying from long-lived isomeric states effectively, there may be other states below the lowest state shown in Fig. 3.19. Therefore, the spins and energies of the these states are not assigned and the energy of the lowest level shown in Fig. 3.19 was given the value E_1 instead of the value zero.

Oblate dipole band When an essential part of the nucleons are aligned parallel to the rotational axis, the nucleus may have an axially symmetric oblate shape. Energy levels of a nucleus with this shape will form an oblate band. Oblate rotational bands consisting of rather regular sequences of magnetic dipole transitions have been observed in many nuclei in the mass A $\approx$ 200 region [52, 54, 55, 56, 57, 58, 59, 60]. The structures of those bands exhibit the features:

(i) Regular energy spacings (from $\approx$ 40 to 70 keV)

(ii) Large $B(M1)/B(E2)$ ratios ($\approx 20(\mu/eb)^2$)

(iii) Small dynamic moments of inertia ($J^{(2)} \approx 20\hbar^2/MeV$)

These structures were generally interpreted as proton particle-hole excitations involving high-K $\pi h_{9/2}$ and $\pi i_{13/2}$ states coupled to one or more $\nu i_{13/2}$ quasineutrons. (K represents the projection of the total momentum onto the symmetry axis.) The high-K deformation-aligned proton excitations are responsible for the oblate deformation and the low-K neutrons align their spins due to the Coriolis forces in the nuclei undergoing oblate collective rotations.

This subsection reports a new oblate dipole band in ^{198}Bi which shows backbending. This band appears to be consistent with one other backbending oblate bands in this region [60]. As with the irregular band (band D) and the backbending band (band CE) described in subsection 3.2.4, and many other oblate bands in this region, no linking transitions to the low-energy levels could be established. Therefore, the excitation energies and the spins of the band are not known.

The analysis revealed a cascade of 14 coincident γ rays in ^{198}Bi with energy spacings typical for oblate collective bands in this region. The partial level scheme of the band and the low-lying transitions were shown in Fig. 3.19. The coincidence spectrum of the band is displayed in Fig. 3.21. The gates in Fig. 3.21a were set on the 203-, 226-, 290-, and 363-keV transitions. Those transitions are above the backbend. Note the sharp drop in intensities of the transitions below the backbend. This implies that decaying out of the band starts at the backbend position. The spectrum in Fig. 3.21b was gated on the four transitions below the backbend. Fig. 3.19 shows the levels to which this band decay.

The spins and excitation energies of this band are not known. However, from the feeding of the band into the 3126-keV state, it can be estimated that the band-head

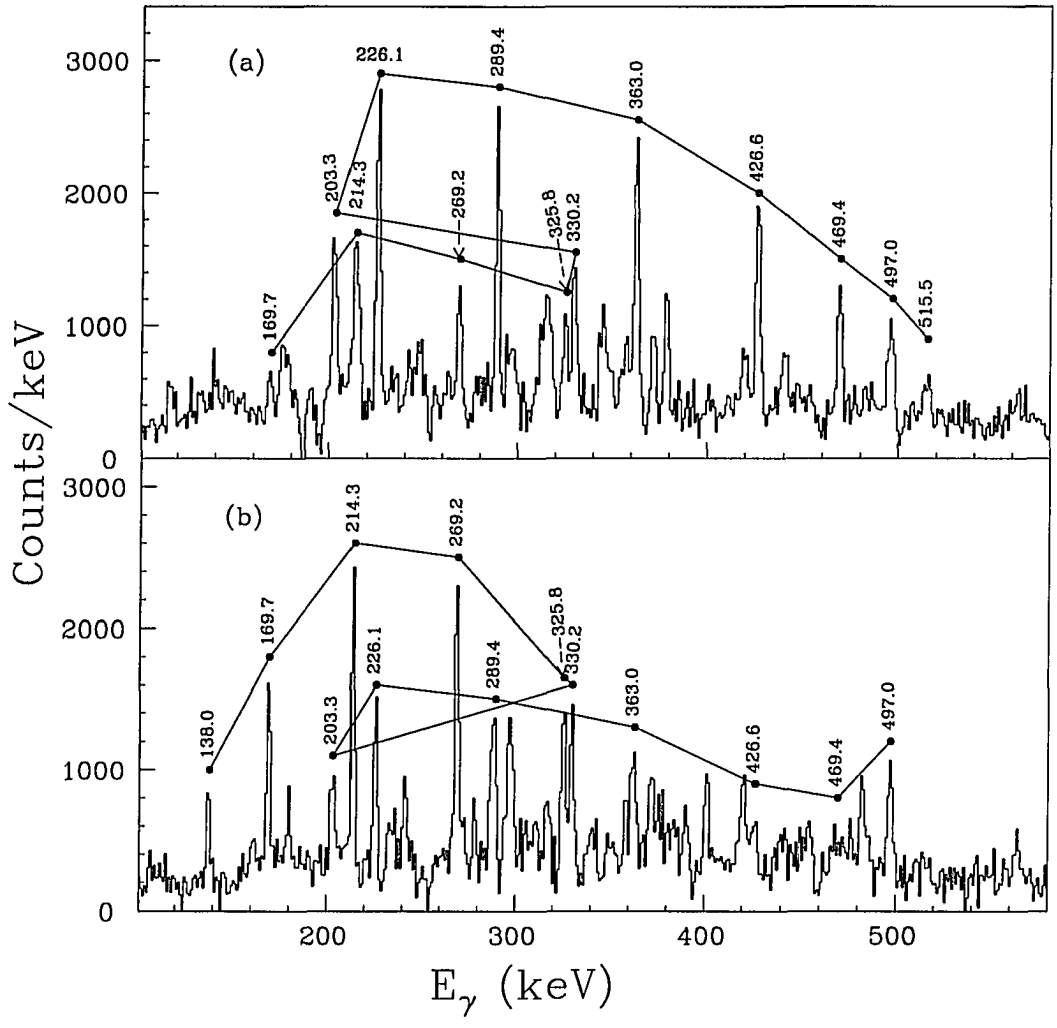

Figure 3.21: The γ-coincidence spectra gated on various members of the band. The dots show the positions of the transitions of the band and the line shows the connection of the band in sequential order: a) gated on the four transitions above the backbend (203, 226, 290, and 363 keV); b) gated on the four transitions below the backbend (170, 214, 269, and 326 keV)

of this band must have a spin of at least 13, which is comparable to the band-head spin of the other backbending band (band CE) in ^{198}Bi. The intensity of this band relative to the total intensity was measured to be about 10%. DCO measurements confirm that the transitions in the band are all dipoles. No associated E2 crossover transitions were found in the data. The lower limit at 95% confidence for the ratio $B(M1)/B(E2)$ was measured to be about $7(\mu/eb)^2$ which is about the same as the ratios for the other backbending band and the irregular band in ^{198}Bi mentioned earlier.

The static moment of inertia, $J^{(0)}$, is not very useful in describing the behavior of nuclei at high spin. The kinematic moment of inertia, defined by $J^{(1)} = \hbar I_x/\omega \approx \hbar^2 I/(E_\gamma \Delta I)$ (where $I_x = \sqrt{I(I+1)} \approx I$ for large I, $w \approx E_\gamma/\hbar$ for dipole and $w \approx E_\gamma/(2\hbar)$ for quadrupole), is more useful but it requires knowledge of the values of the spins. The dynamic moment of inertia, $J^{(2)}$, is more useful in describing the nucleus and the spins need not be known. It is defined as $J^{(2)} = \hbar \mathrm{d}I_x/\mathrm{d}\omega$, is approximately given by $\hbar^2/\Delta E_\gamma$ (for dipole) when the spins are unknown but are assumed to be relatively large ($I \geq 10$).

The dynamic moments of inertia $J^{(2)}$ of the band (before the backbend) and the spins I, as a function of rotational frequency, are shown in Fig. 3.22 together with those in ^{202}Bi, ^{197}Pb and ^{199}Pb. The absolute spins of ^{198}Bi are not known and the ones shown in Fig. 3.22 were adjusted to match those of ^{199}Pb for comparison. There clearly are similarities between the dynamic moments of inertia for the regular band in ^{198}Bi and the bands in ^{202}Bi, ^{197}Pb, and ^{199}Pb. This suggests that the structures in these nuclei are built on similar configurations. For the bands in ^{197,199}Pb and ^{202}Bi [52, 55, 60, 59], it has been suggested that the proton configurations responsible are

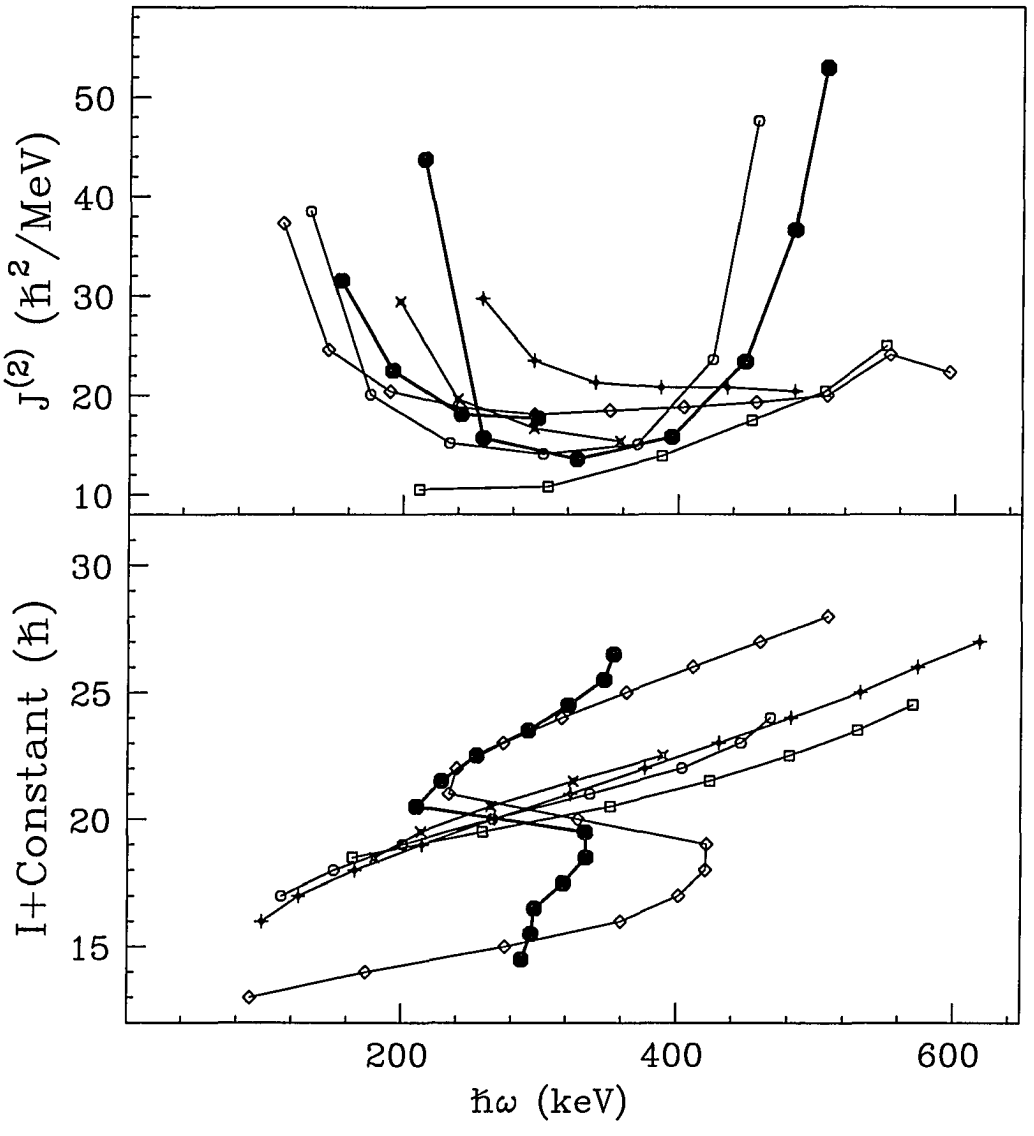

Figure 3.22: Dynamic moments of inertia, $J^{(2)}$, and spins, I, of the regular band in ^{198}Bi compared to those of the neighboring nuclei. Closed circles: the regular band in ^{198}Bi; open square: band 1 in ^{202}Bi; diagonal crosses: band 2 in ^{202}Bi; open diamonds: band 1 in ^{199}Pb; vertical crosses: band 2 in ^{199}Pb; open circles: the regular band in ^{197}Pb

2p-2h (for Pb) such as $(\pi h_{9/2} \otimes \pi i_{13/2} \otimes \pi s_{1/2}^{-2})$ or $(\pi h_{9/2}^2 \otimes \pi s_{1/2}^{-2})$, and 2p-1h (for ^{202}Bi) such as $(\pi h_{9/2} \otimes \pi i_{13/2} \otimes \pi s_{1/2}^{-1})$ or $(\pi h_{9/2}^2 \otimes \pi s_{1/2}^{-1})$, coupled to one or more $i_{13/2}$ neutron-holes. For the bands in ^{198}Bi, the band just mentioned and band CE in subsection 3.2.4, a similar interpretation is also suggested (i.e., the bands may have the configuration $(\pi h_{9/2} \otimes \pi i_{13/2} \otimes \pi s_{1/2}^{-1})$ or $(\pi h_{9/2}^2 \otimes \pi s_{1/2}^{-1})$ coupled to one or more neutron-holes).

3.3 Conclusion

About 80 new transitions have been identified and placed into the level scheme of ^{198}Bi. The partial level scheme of ^{198}Bi has been extended up to a spin of about $30\hbar$ (see Fig. 3.22b) and an energy of about 7 MeV (see Fig. 3.19). The low-lying transitions based on neutron excitation were found to be similar to those in heavier Bi isotopes. Another cascade of low-lying transitions, thought to be based on the excitation of one proton and one (or more) neutrons, is completely new for any Pb or Bi nucleus in this mass region. At least one irregular and two backbending bands with fast dipole transitions were observed. Similar bands have also been observed in other nuclei in this region. These bands are interpreted as evidence of a collective rotation of an oblate-deformed nucleus. Further detailed experimental studies are necessary to establish the linking transitions between the bands and the low-lying states.

CHAPTER 4. SUPERDEFORMATION IN ^{191}Au

A nucleus can have a variety of shapes, sometimes "exotic" one such as superdeformed (SD). A SD nucleus has axially symmetric prolate shape that can be characterized by the ratio of the major axis to the minor axis. For the nuclei in the actinides and the mass 150 region, this ratio is 2:1. This ratio is not as large for the nuclei in mass 190 region (1.7:1), and it is only 1.5:1 for the nuclei in the mass 130 region. This chapter will focus on the properties of ^{191}Au at very high spin where it has superdeformed shape.

4.1 Experimental method

The experiments were carried out at the Lawrence Berkeley Laboratory 88-Inch Cyclotron using the High Energy-Resolution Array (HERA) facility. (HERA, which consisted of twenty Compton-suppressed Ge detectors and a central 40-element bismuth germanate (BGO) ball, was described in chapter 2). States in ^{190,191,192}Au were populated in the reaction ^{186}W(^{11}B,xn) at three different beam energies: 78-, 84-, and 86-MeV. The targets consisted of one to three stacked self-supporting ^{186}W foils of 0.5 mg/cm^2 thickness. Previous experiments in high-spin studies showed that superdeformed bands were always associated with high-multiplicity events. The low-multiplicity doubly coincident events (i.e., two Ge detectors in coincidence) were not

useful for these particular experiments because most of those events were not SD related. SD information could still be extracted from the low-multiplicity events, if those were triple coincidences, by double gating (i.e., if two of the three γ-ray energies coincide with the two gates then the third γ-ray energy is put in the energy spectrum). Therefore, in the experiment, all three- and higher-fold γ-ray coincidences were recorded. The two-fold coincidence events were recorded only if they were in coincidence with at least six inner ball detectors. All events were recorded together with the γ-ray sum energy and multiplicity of the "Ge + shield" detector units, and of the inner ball. Also, in the 86-MeV reaction, the time differences between the γ rays detected in the BGO ball and the first-coincident Ge detector were recorded to enable the rejection of delayed γ rays and neutron-induced events. A total of 2.0×10^8, 1.9×10^8, and 3.7×10^8 double events and 3.5×10^7, 4.3×10^7, and 5.0×10^7 triple and higher coincidence events were recorded for the three runs at 78-, 84-, and 86-MeV, respectively. In each case Doppler-shift corrections were made on the energies of the γ rays emitted from the recoiling nuclei.

The reasons why those particular energies were chosen to populate the SD ^{191}Au nuclei can be seen from Fig. 4.1. This figure was generated using a program named PACE to calculate the cross sections of the products in a reaction. PACE uses the semiempirical method to calculate the cross sections (i.e., it employs both theory and known experimental results in its calculations). From the previous works on SD nuclei in this mass region, it was known that SD populations peak at an energy slightly higher than those for normal deformation. Therefore, in the original experiment, the bombarding energies used were 78 MeV (which is the peak energy for normal deformation) and 84 MeV. Unfortunately, the target used in that experiment (three

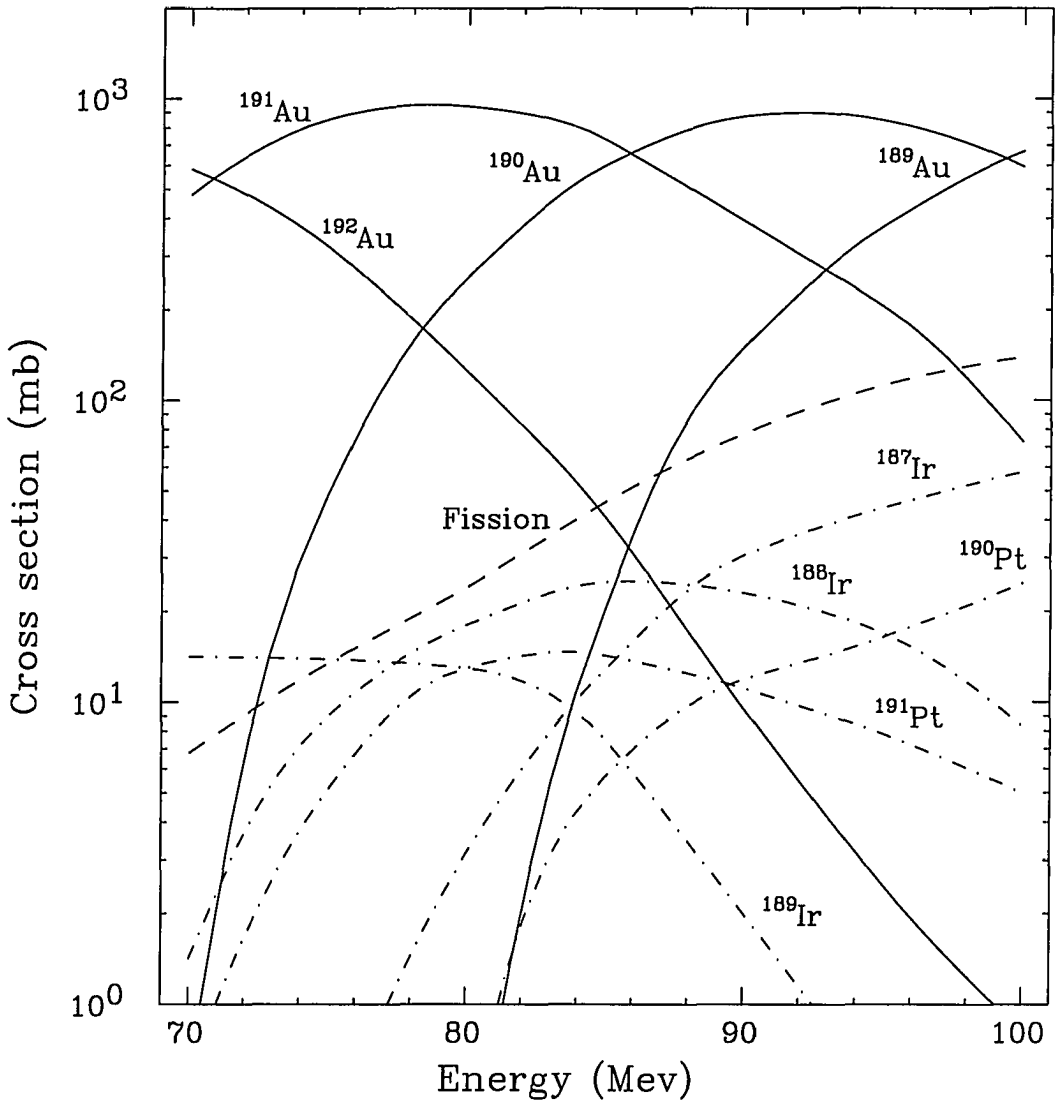

Figure 4.1: PACE calculations for the reaction ^{11}B+^{186}W

stacked self-supporting ^{186}W foils of 0.5 mg/cm^2 thickness) was too thick to let all the compound nuclei recoil out of the target. A large fraction of the compound nuclei was stopped in the target. This fact was not known during the data taking process and it became apparent only after intensive analysis was done on the data. As mentioned in the last paragraph, the γ rays emitted from the recoiling nuclei would be Doppler-shifted and corrections had to be made for those γ rays. When Doppler-shift corrections were applied to γ rays emitted from the stopped nuclei, the true energies of the γ rays would be shifted. These shifted energy peaks mixed with the true energy peaks from recoiling nuclei and the results were broad peaks. This made the search for weak SD bands almost impossible.

In the second experiment, the target used originally was one self-supporting ^{186}W foil of 0.5 mg/cm^2 thickness. It later was changed to two stacked foils of 0.5 mg/cm^2 to increase the reaction rate. Due to the fruitless search in the 78-MeV and 84-MeV data sets, a slightly higher bombarding energy (86 MeV) was used in this experiment. This decision had proved to be a success.

In a separate set of experiments, the ^{176}Yb(^{19}F,xn) reaction was used at 100- and 105-MeV bombarding energies with a target consisting of three stacked ^{176}Yb metallic foils of 0.5 mg/cm^2 thickness to produce states in ^{189,190}Au. Summed over both bombarding energies, a total of 3.4×10^8 double and 1.2×10^8 triple and higher coincidence events were recorded.

4.2 Data analysis

Correlation matrices of E_γ-E_γ coincidences were constructed with various γ-ray sum-energy (H) and multiplicity (k) requirements. A channel-by-channel search of

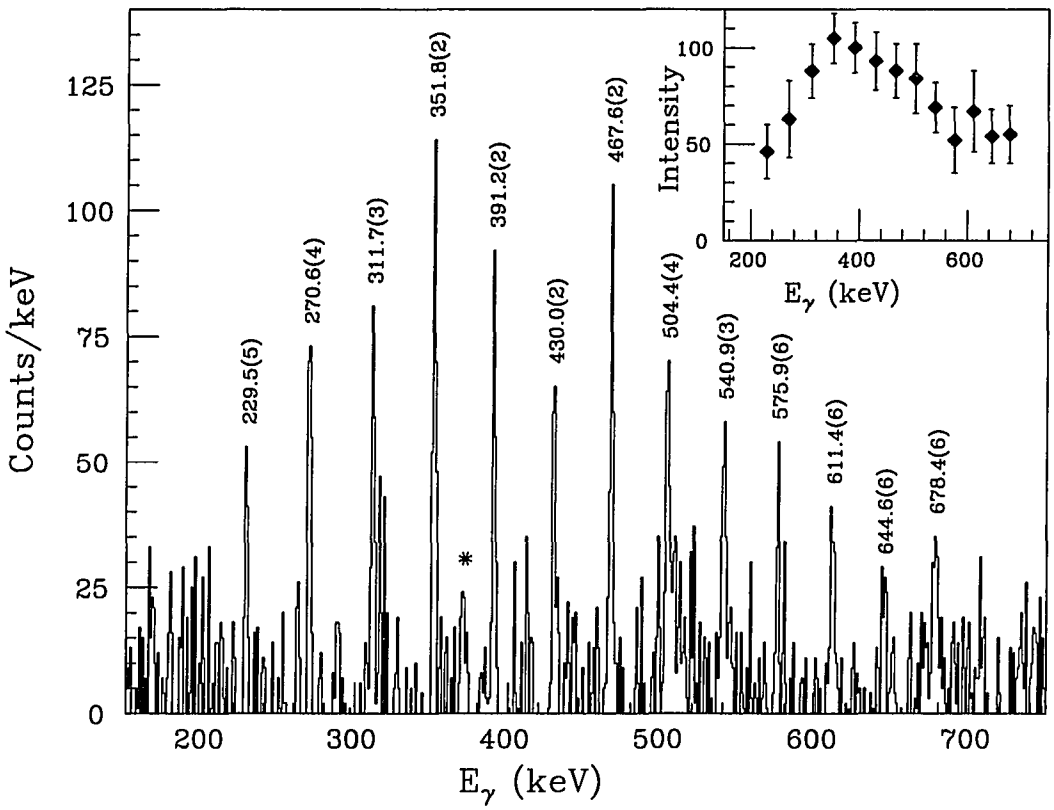

Figure 4.2: The γ-ray spectrum of the SD band produced in the $^{186}W(^{11}B, 6n)^{191}Au$ reaction. The data represent the sum of the 84-MeV and 86-MeV data sets. This spectrum is obtained by double gating three- and higher-fold events at multiplicity k$\geq$17 and sum-energy H$\geq$12 MeV. For the 84-MeV data set, the gates are 9 transitions from 228 keV to 540 keV. The gates for the 86-MeV data set are all 13 band members. The transition indicated by (*) is 371 keV (see text). The inset shows the transition intensities, deduced from the double-gated spectrum

the matrices revealed a band of at least 13 transitions from E_γ = 229 keV to 678 keV in the 86-MeV set for the $^{186}W(^{11}B,xn)$ reaction (Fig. 4.2). After knowing the γ-ray energies of the band, the old data (taken at 78-MeV and 84-MeV bombarding energies) was reanalized and the same band was found in the 84-MeV data set. There is also some weak indication of this band in the 78-MeV data set. The transition indicated by (*) in Fig. 4.2 is found in coincidence with SD band members. It has the same energy (371 keV) as the known low-spin $13/2^-$ to $9/2^-$ transition in ^{191}Au [62]. However, this transition feeds the 10-ns isomer in ^{191}Au. Because the recoiling nuclei move out of view of the Ge detectors, the 274-keV ($9/2^-$ to $11/2^-$) and subsequent transitions in the decay of the isomer are not seen.

The energies and intensities of the γ rays in this band are listed in Table 4.1. The relative intensity pattern of the band is shown in the inset in Fig. 4.2. The intensity uncertainties are relatively large due to the very weak γ-ray intensities. The transition intensities (with internal conversion included) increase as the transition energies decrease, become relatively constant for energies from 500 keV down to 300 keV, and decrease at lower energies. This intensity pattern is similar to those of the bands in ^{191}Hg[63]. The energy spacings of the transitions in this band are similar to others in this region, with the differences between adjacent transitions being $\approx$ 41 keV for the lowest energy transitions and $\approx$ 34 keV for the highest energy transitions.

4.2.1 Mass assignment of the SD band

The assignment of the new band to ^{191}Au is supported by the excitation function and cross bombardment results. The SD band is much weaker in the 78-MeV reaction data where ^{192}Au is much more intense (compared with either the 84- or

Table 4.1: Transitions and relative intensities of the SD band. The intensity of the 391.2-keV transition is about 0.15% of the total intensity of ^{191}Au. The uncertainties of the least significant digits of the energies and intensities are indicated in the parentheses

γ-ray energy (keV)	Relative γ-ray intensity
229.5(5)	46(14)
270.6(4)	63(20)
311.7(3)	88(14)
351.8(2)	105(13)
391.2(2)	100(13)
430.0(2)	93(15)
467.6(2)	88(14)
504.4(4)	84(18)
540.9(3)	69(13)
575.9(6)	52(17)
611.4(6)	67(21)
644.6(6)	54(14)
678.4(6)	55(15)

86-MeV reaction) so that one may rule out the possibility of the SD band belonging to ^{192}Au. Known states with similar spins were populated in the other experiment, ^{176}Yb(^{19}F,xn). The residual nucleus has about the same energy of excitation and maximum angular momentum as those in the ^{186}W(^{11}B,6n) reaction. The statistics of ^{190}Au in this reaction are much better, and the ^{191}Au populations are much smaller, than those in the ^{186}W(^{11}B,xn) reaction at 84 MeV and 86 MeV. Careful searches for this SD band were performed in these data and it was not found. This suggests that this SD band most likely belongs to ^{191}Au and not to ^{190,192}Au. With a multiplicity $k \geq 18$ and sum-energy $H \geq 14$ MeV, the band intensity is only 0.15% of the total ^{191}Au intensity. It is one of the most weakly populated SD bands found to date.

There are not sufficient statistics for making a directional correlation analysis to establish multipolarities, and it may be possible that this is a dipole band. However, Fig. 4.3 and Fig. 4.4, which are the plots of the dynamic moments of inertia against frequency ($\hbar\omega$) for this new band compared with similar plots of dipole bands (e.g., in ^{197}Pb and in ^{199}Pb)[52, 60] and other SD bands in this region show a behavior of the dynamic moments of inertia more regular than those of dipole bands and more similar to that of the SD bands. In fact, the new SD band in ^{191}Au is identical to some other SD bands in ^{192}Hg, ^{191}Hg ... Therefore, the reasonable assumption was made that these cascade γ-rays of the new SD band have multipolarity $L = 2$. Because of the weakness of this SD band one might be tempted to assign it to a Pt nucleus produced by a competing (^{11}B,pxn) reaction. However, the present data show that the amount of the Pt produced by the competing pxn channel is a factor of about 30 less than the Au. Typically SD bands in this region are populated at $\approx$ 1% or less. For the observed SD band to be in Pt, therefore, it would have to be populated

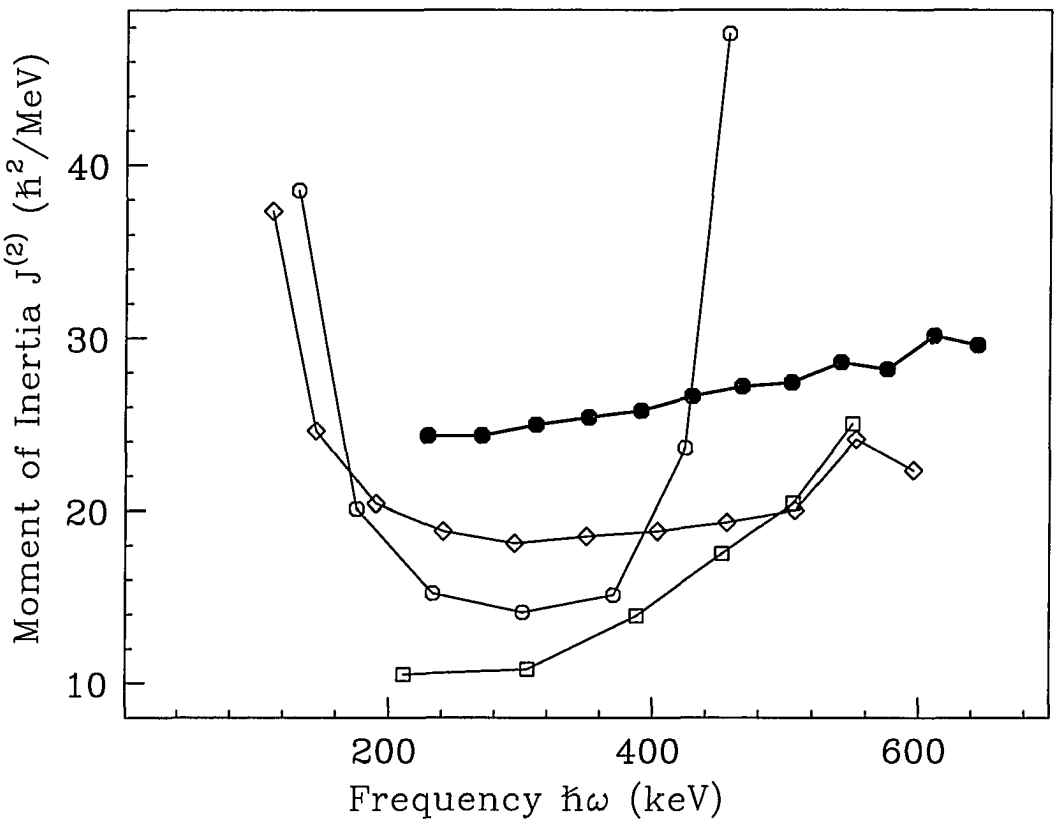

Figure 4.3: Dynamic moments of inertia of the new band in ^{191}Au (assuming dipole) compared to the dipole bands of some other nuclei in the mass $\approx$ 190 region. Closed circles: the new band in ^{191}Au; open diamonds: band 1 in ^{199}Pb; open squares: band 2 in ^{199}Pb; open circles: the regular band in ^{197}Pb

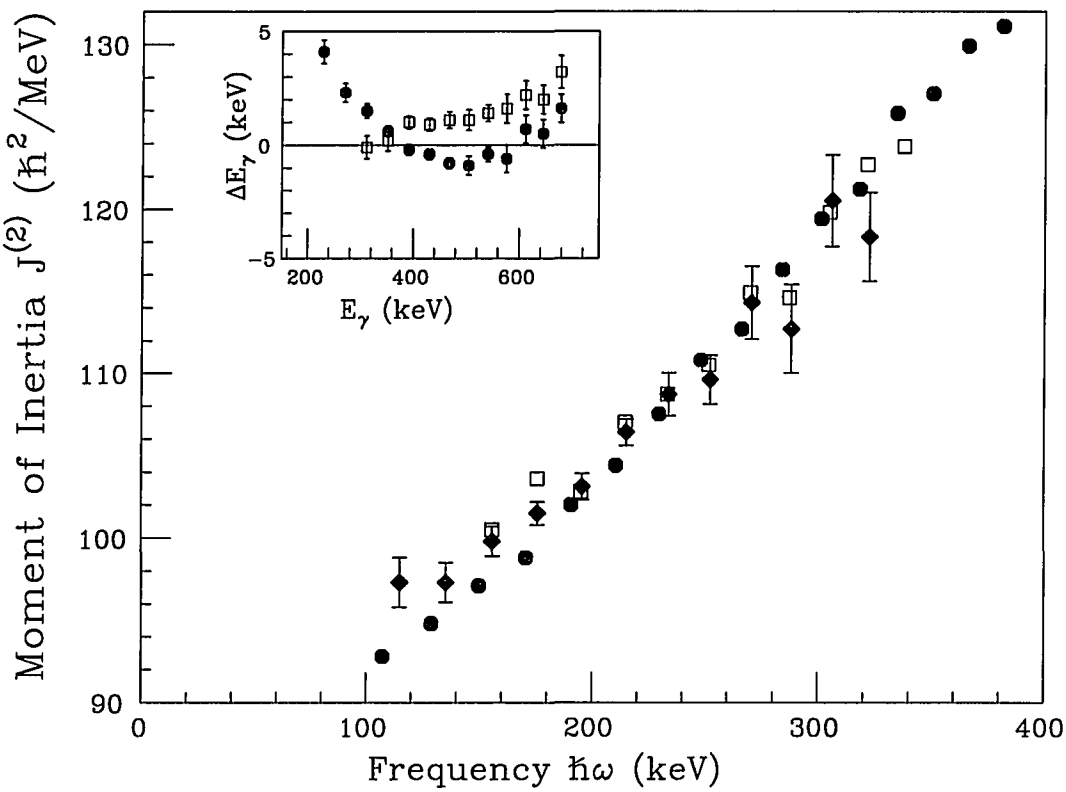

Figure 4.4: Dynamic moment of inertia of the ^{191}Au SD band (diamonds) compared to those in ^{192}Hg (circles) and ^{191}Hg* (squares). The inset shows the energy differences between the bands (circles, ^{191}Au - ^{192}Hg quarter-point energies; squares, ^{191}Au - ^{191}Hg*)

at the unusually high level of 5% to give the intensity observed. This alternative is regarded as unlikely.

4.2.2 Discussion

In order to compare this new SD band to other bands in this mass region, its dynamic moment of inertia is displayed in Fig. 4.4 together with those of ^{192}Hg [64, 65] and ^{191}Hg* (band 3 in Ref. [63]). It is seen that the moment of inertia for ^{191}Au is very similar to those of the SD bands of ^{192}Hg and ^{191}Hg* . The energy differences between the transitions of ^{191}Au, ^{192}Hg, and ^{191}Hg* SD bands are also shown. Except for the lowest- and highest-energy transitions, all the comparable transitions in the band are within 2 keV of "quarter-point energies" of the ^{192}Hg band and those of the ^{191}Hg* SD band. (As an example, if three successive transition energies of a band are 200, 240, and 280 keV, then the "quarter-point energies" of that band are 210, 250, and 290 keV.) This makes the ^{191}Au SD band appear to be identical to the ^{192}Hg and ^{191}Hg* SD bands.

Using the particle-rotor model, in which one or more particles are coupled to a rotating deformed core, the γ-ray energy for an $I \rightarrow I-2$ transition is given by

$$E_\gamma = \frac{\hbar^2}{2J}[4(I-i)-2], \tag{4.1}$$

where i is the alignment caused by the Coriolis force (i.e., the Coriolis force tries to break up the coupling of the odd particle to the deformed core and align it parallel to the rotational axis), and J is the moment of inertia of the band. In the particle-rotor model, to the first order perturbation,

$$i = \frac{1}{2}(-1)^{I-1/2} a \delta_{K,1/2}, \tag{4.2}$$

where the quantum number K represents the projection of the total momentum I on to the symmetry axis and a is the decoupling parameter. This makes $i = 0$ for $K \neq 1/2$. Note that $i = \pm 1/2$ for $K = 1/2$ and $a = \pm 1$.

From equation 4.1, it can be seen that for an odd-A nucleus to be identical to quarter-point energies of the even-even core, the alignment i must be an integer. The fact that the transition energies of the SD band in ^{191}Au are identical to the quarter-point energies of the ^{192}Hg band implies that the odd proton hole (relative to the ^{192}Hg core) occurs in an orbital which has a zero or an integer alignment. This suggests the SD band in ^{191}Au is probably a high-K ($K \neq 1/2$) band. However, this also means that there should be a signature-partner band (with comparable γ-ray intensities) to the ^{191}Au SD band with the transition energies at half-point energies of the ^{191}Au SD band. Signature-partner bands are bands with the same Nilsson quantum numbers $[Nn_z\Lambda]\Omega^\pi$ but have opposite signature (i.e., if one band is characterized by the single particle with the intrinsic spin pointing in the positive z direction then its signature partner has the intrinsic spin of the single particle pointing in the negative z direction). The Nilsson quantum numbers $[Nn_z\Lambda]\Omega^\pi$ are used to classify the levels of a nucleus, where N is the principal quantum number of a shell, n_z is the projection of N on to the symmetry axis, Λ is the projection of the orbital angular momentum on to the symmetry axis, Ω is the projection of angular momentum j of the valence particle on to the symmetry axis, and π is the parity of the states. For the case of axial symmetry, the even-even core of the nucleus does not contribute to the total angular momentum I. Therefore, Ω has to be equal to K, the projection of total angular momentum on to the symmetry axis.

From the property of signature-partner bands, it can be seen that if one band

has the $I = ...10.5, 12.5, 14.5...$ then the other band will have $I = ...11.5, 13.5, 15.5....$ An illustration of the half-point transition energies of signature-partner bands can be readily built from equation 4.1 above (by setting $i = 0$). No such band was observed in ^{191}Au. The absence of a signature-partner band with the transition energies at half-point energies of the ^{191}Au SD band suggests some signature splitting. Signature splitting occurs when the Nilsson orbital is split into two distinct orbitals with different moments of inertia. When that happens, the energy levels (and the transition energies) of the signature-partner bands do not relate to each other any more. (This can be seen form equation 4.1 by using different moments of inertia for the signature-partner bands.) Therefore, for signature splitting orbitals, the transition energies of one band will not be at half-point energies of its signature-partner band. A $K = 1/2$ orbital begins to split at zero rotational frequency. When the rotational frequency of a nucleus is increasing, all the Nilsson orbital will eventually split into two distinct orbitals. However, for high-K orbitals, the splittings do not happen until the rotational frequency becomes large. The half-point energy property of signature-partner bands can still be seen at low transition energies. Therefore, the absence of half-point energies of the signature-partner band, even at low transition energies, suggests that the signature splitting takes place at zero rotational frequency, which in turn implies that the band belongs to a $K = 1/2$ band and not a $K \neq 1/2$ band.

In the strong coupling limit of the particle-rotor model, the alignment i is assumed to be very small compared with the coupling term and it is set to be zero. This assumption is correct for high-K bands but not for $K = 1/2$ bands (see equation 4.2) The arguments presented above suggest the band may belong to a $K = 1/2$ band. It therefore appears that this band is not based on a strongly coupled orbital.

In order to help assign this odd-Z band to a specific orbital, the single-particle Routhians (Figs. 4.5, 4.6) for ^{191}Au were constructed. Routhian energy is the nuclear energy, calculated from the single-particles in a deformed potential, and is given as

$$E_R(I) = E(I) - I_x(I)\hbar\omega,$$

where $E_R(I)$ is the Routhian energy, $E(I)$ is the energy level of the rotational band, and I_x represents the component of the angular momentum perpendicular to the symmetry axis.

The deformation parameters used to produce these plots were obtained from total Routhian surface (TRS) calculations, based on a deformed Woods-Saxon potential and the Strutinsky shell correction formalism with a monopole pairing interaction [66, 67]. Fig. 4.6 shows that at these deformations there are several proton orbitals near the Fermi surface, including the [411]1/2 and [530]1/2. Other possibilities are the 6_2 (i.e., [651]3/2 in full Nilsson notation) and the [532]3/2 orbitals. However, these seem less likely because the 6_2 orbital has a changing alignment and the [532]3/2 appears farther away from the Fermi level in these calculations. Both the [411]1/2 and the [530]1/2 orbitals are fairly flat in the observed frequency range. Since a proton hole in a flat orbital will produce no alignment relative to ^{192}Hg, either of these two orbitals would not be inconsistent with the observed γ energies.

The acceptance of the SD band in ^{191}Au belonging to either the [411]1/2 or the [530]1/2 orbital (i.e., $K = 1/2$) requires that the decoupling parameter for this orbit be different at these deformations (see eq. 4.2), i.e., requiring $a \approx 0$ instead of $a = \pm 1$.

Within the framework of the particle-rotor model, the decoupling parameter can be calculated using the asymptotic quantum numbers. For a $[Nn_z\Lambda]\Omega$ orbital, the

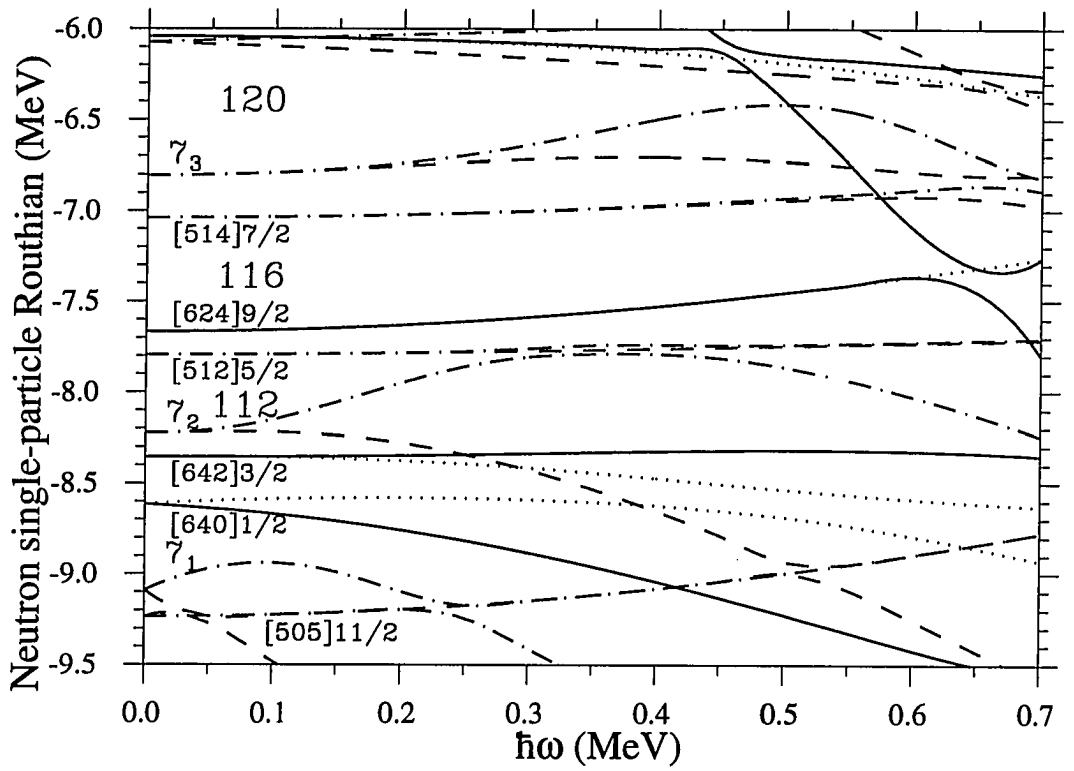

Figure 4.5: Neutron single-particle Routhians for ^{191}Au with deformation parameters $\beta_2 = 0.457$, $\beta_4 = 0.048$, and $\gamma = 0.0$. The parameters are taken from the lowest SD minimum in the TRS calculations. Spin & signature (π,α) : solid = (+,+1/2), dotted = (+,–1/2), dash-dotted = (–,+1/2), dashed = (–,–1/2)

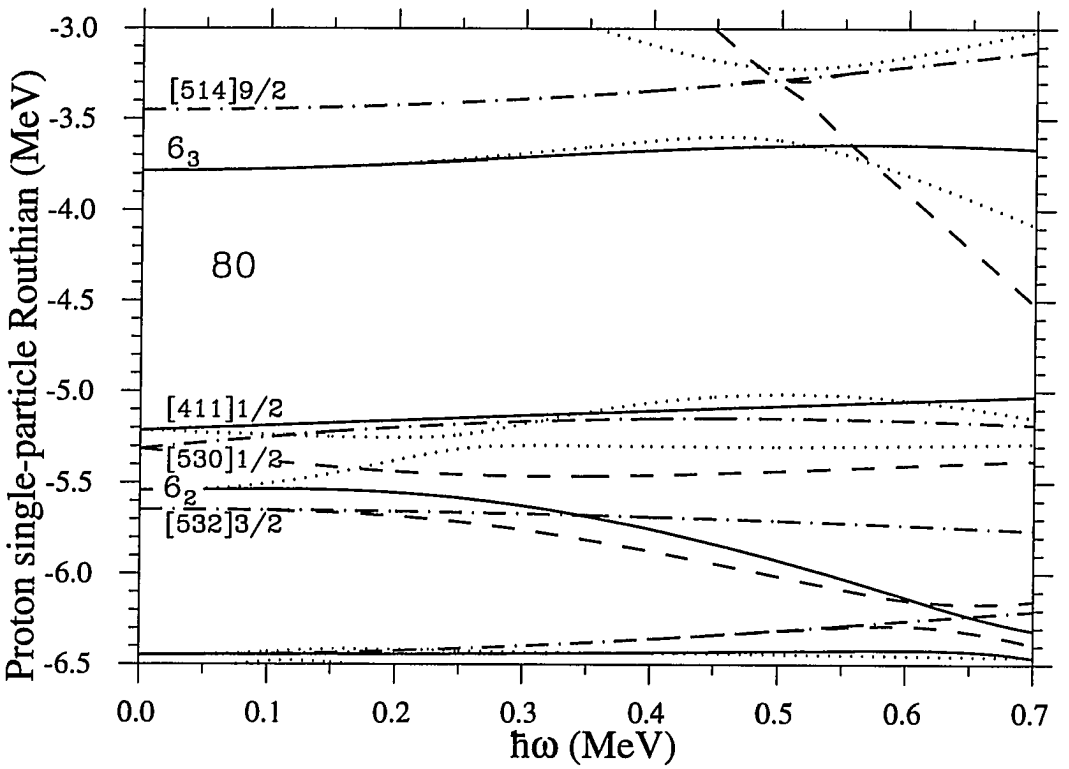

Figure 4.6: Proton single-particle Routhians for ^{191}Au with deformation parameters $\beta_2 = 0.457$, $\beta_4 = 0.048$, and $\gamma = 0.0$. The parameters are taken from the lowest SD minimum in the TRS calculations. Spin & signature (π,α) : solid = (+,+1/2), dotted = (+,−1/2), dash-dotted = (−,+1/2), dashed = (−,−1/2)

decoupling parameter is given by

$$a = (-)^N \delta_{\Lambda,0}. \tag{4.3}$$

That would result in $a = 0$ for the [411]1/2 orbital and $a = -1$ for the [530]1/2 orbital. These results would favor the ^{191}Au SD band occupying the [411]1/2 orbital. However, in the attempts to explain the identical bands in the A = 150 region, it was found that the normal-asymptotic limit was not good in determining the decoupling parameter [5]. Instead, it was suggested to use the pseudo-asymptotic limit to calculate the decoupling parameter a. Pseudo-asymptotic numbers are calculated in a similar manner as the normal-parity orbitals, where the $(d_{5/2}, g_{7/2})$ doublet becomes $\tilde{f}_{5/2,7/2}$ and the $(f_{7/2}, h_{9/2})$ becomes $\tilde{g}_{7/2,9/2}$, etc... For the pseudo-asymptotic numbers, the pair of orbits

$$[N, n_z, \Lambda]\Omega = \Lambda + 1/2 \quad \text{and} \quad [N, n_z, \Lambda + 2]\Omega = \Lambda + 3/2$$

will become

$$[\widetilde{N} = N - 1, n_z, \tilde{\Lambda} = \Lambda + 1]\tilde{\Omega} = \tilde{\Lambda} \pm 1/2$$

which can be written as $[\widetilde{N n_z}\Lambda]\Omega$.

The new asymptotic doublet is best thought of as pseudo-spin-orbit partners. The main feature of this picture is that the mixing of parallel and antiparallel couplings of the intrinsic spin to the orbital angular momentum gives strongly coupled pseudo-orbital angular momentum and weak pseudo-spin-orbit coupling. Since the spin-orbit coupling $\tilde{l} \cdot \tilde{s}$ is weak, the Coriolis forces could then align the pseudo-spin $\tilde{s}$ along the rotation axis, leaving the pseudo-orbital angular momentum coupled to the symmetry axis.

Applying the pseudo-spin formula to the normal-asymptotic quantum numbers, the [411]1/2 orbital (coupled to itself) will become $[\widetilde{310}]1/2$ and the [530]1/2 orbital (coupled to the [532]3/2 orbital, see Fig. 4.6) will become $[\widetilde{431}]1/2$. Using these new numbers and the equation 4.3, the decoupling parameter for the [411]1/2 orbital becomes zero and the decoupling parameter for the [530]1/2 orbital becomes -1. This result favors the odd proton in ^{191}Au belonging to the [530]1/2 orbital. However, even though the pseudo-asymptotic formalism was able to provide the correct decoupling parameter for explaining the identical SD bands in the A = 150 region, it is not guaranteed to give the correct explanation for the SD bands in the A = 190 region because SD bands in the A = 150 region are not the same as SD bands in the A = 190 region. One example of this is the fact that most of the pairs of identical SD bands in the A = 190 region are different by a pair of protons or a pair of neutrons, but in the A = 150 region, all the identical SD pairs are different by one nucleon. Therefore, the [530]1/2 orbital assignment based on this formalism may be regarded as one of the possible choices.

None of the attempts described above to assign the SD band in ^{191}Au to a specific orbital, from the strong coupling limit to the normal- and pseudo-asymptotic limits, has satisfactorily explained and confirmed the orbital for the band. The difficulty in trying to assign the orbital and to explain the properties of this band is that it is the first (and the only) SD band with Z<80, the "SD nuclear magic number", in this A = 190 region. Note that the magic numbers for SD nuclei are not the same numbers as those for normal nuclei (see Fig. 4.6, where the major band gap is at 80 instead of 82). It is also the only SD band proposed as based on a $K = 1/2$ orbital. More studies of SD bands in Au, Pt, and Ir (with Z<80) are needed before one can confirm

to which orbital the SD band in ^{191}Au belongs.

An alternate method of assigning the SD band in ^{191}Au to an orbital is to compare it with the identical SD band in ^{191}Hg*. From Fig. 4.5 and Fig. 4.6, it can be seen that proton hole in the orbital ([411]1/2, $\alpha = +1/2$) (^{191}Au yrast) would produce a similar effect as a neutron hole in ([642]3/2, $\alpha = +1/2$) (^{191}Hg*) because both orbitals have almost zero slopes and curvatures. This interpretation may explain the absence (or weakness) of the signature-partner of the ^{191}Au SD band since the [411]1/2 orbital has some signature splitting. However, it is not clear how the inclusion of pairing would affect these arguments.

The spins of the states are suggested using the methods of Draper *et al* [68] and Becker *et al* [69]. In Ref. [68], the moment of inertia $J^{(2)}$ is first fitted by the Harris expansion

$$J^{(2)}(\omega) = 2\alpha + 4\beta\omega^2 + 6\gamma\omega^4,$$

to obtain the coefficients α, β, and γ. Integrating $J^{(2)}$ with respect to ω gives

$$I_\gamma(\omega) - i + \frac{1}{2} = 2\alpha\omega + \frac{4}{3}\beta\omega^3 + \frac{6}{5}\gamma\omega^5,$$

where i is the alignment. The value i can not be directly determined, but was believed to be very small, i.e., $i \approx 0$. This alignment i was set to zero in the fitting program.

The second spin fitting method [69] uses two fitting equations. In the first case, the fitting procedure is similar to that of Ref. [68] but only the first two terms of the Harris expansion are used. In the second case, least-squares fit is made to the equation,

$$E_\gamma = E(I+2) - E(I),$$

with $E(I)$ expressed as a series in powers of $I(I+1)$,

$$E(I) = AI(I+1) + BI^2(I+1)^2 + CI^3(I+1)^3.$$

Using the two methods to fit the energies of the transitions gives an average of 11.23(6) for the spin of the upper level of the 229-keV transition. Since the nucleus is odd-A, the most likely spin consistent with the above least-squares analysis for the upper level is 23/2. The difference between the fitted spin and the expected spin could be accounted for if the initial alignment is included. The orbital alignment at $\omega = 0$ is not zero since this SD band is a $K = 1/2$ band. From the TRS calculations (see Fig. 4.6), the initial alignment, $dE/d\omega$ at $\omega = 0$, is found to be about $0.25\hbar$. Adding this value to the spin obtained from the fits above would give the spin of 11.5. Thus, the 229-keV transition is tentatively assigned to represent the decay of the 23/2 level to the 19/2 level. Given the uncertainty of both the spin fittings and the TRS calculations, it is not clear how significant this agreement is.

The alignment plots [70] for ^{191}Au and ^{191}Hg* relative to ^{192}Hg are displayed in Fig. 4.7. As with many other examples of SD bands in this region, ^{191}Au shows an alignment of i=1 relative to ^{192}Hg. This general phenomenon is not well understood. However, it has been discussed [70] in terms of the aligned intrinsic pseudo-spins of a pair of valence nucleons. The weak coupling of the pseudo-orbital angular momentum to the pseudo-intrinsic spin is a property of the observed approximate pseudo-spin symmetry in nuclear systems [71].

In addition to the SD band in ^{191}Au described above, another somewhat weaker band with energies nearly identical to the yrast SD band in ^{191}Hg[72] was observed. Fig. 4.8 show the γ-ray spectrum of this SD band produced in the ^{186}W(^{11}B, xn) reaction at 186-MeV bombarding energy. The transition energies of this band are

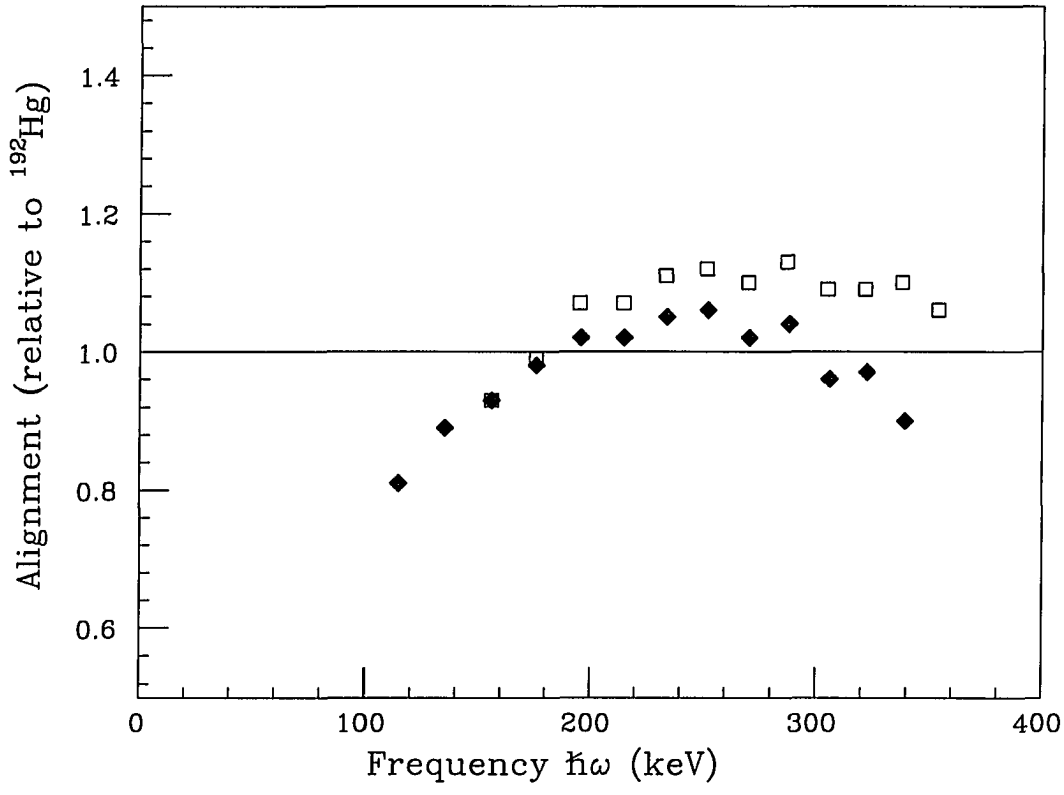

Figure 4.7: Alignment of the ^{191}Au SD band (diamonds) and the ^{191}Hg* SD band (squares) relative to the ^{192}Hg SD band.

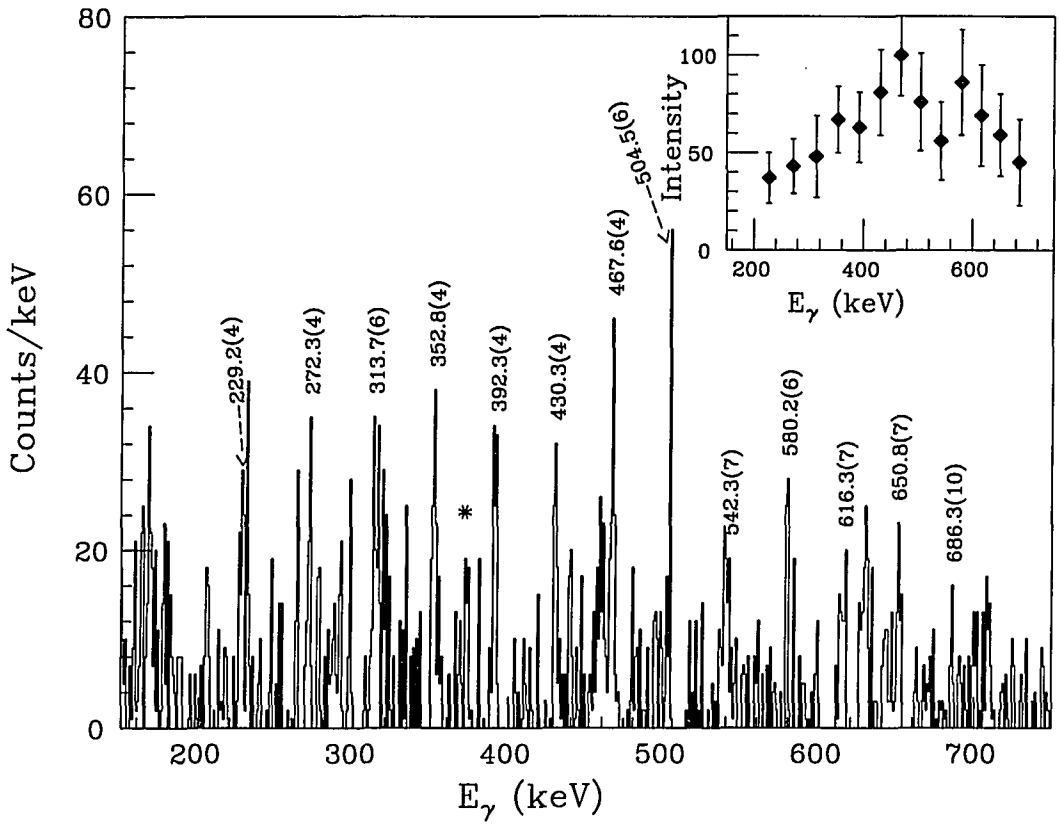

Figure 4.8: The γ-ray spectrum of the SD band produced in the $^{186}W(^{11}B, 6n)^{191}Au$ reaction at 186-keV bombarding energy. This spectrum is obtained by double gating three- and higher-fold events at multiplicity k$\geq$12 and sum-energy H$\geq$9 MeV. The gates are all 13 band members. The transition indicated by (*) is the 371-keV transition that has appeared earlier in Fig. 4.2. The inset shows the transition intensities, deduced from the double-gated spectrum

Table 4.2: Transitions and relative intensities of the second SD band. The uncertainties of the least significant digits of energies and intensities are indicated in the parentheses

γ-ray energy (keV)	Relative γ-ray intensity
229.2(4)	37(13)
272.3(4)	43(14)
313.7(6)	48(21)
352.8(4)	67(17)
392.3(4)	63(18)
430.3(4)	81(22)
467.6(4)	100(21)
504.5(6)	76(25)
542.3(7)	56(20)
580.2(6)	86(27)
616.3(7)	69(26)
650.8(7)	59(21)
686.3(10)	45(22)

nearly the same as those in the newly found SD band for low E_γ and they diverge at high E_γ. The relative intensity pattern of the band is shown in the inset. This second band was seen only in the 86-MeV data set and the data are insufficient to assign it to a nucleus.

The energies and intensities of the γ rays in this band are listed in Table 4.2. The energy uncertainties and intensity uncertainties are large due to the very weak γ-ray intensities. By comparing the double-gated spectra of this band and the first band, the average intensity of this second band appears to be about half of that of the first band. Because of its apparent relationships to the SD bands of ^{191}Hg and ^{191}Au, it would be very interesting to characterize this band further. It is interesting to note that, if this band belongs to ^{191}Au, then it could be the signature-partner

of the first SD band. From the particle-rotor model calculations (discussed earlier), the alignment i for the SD band in ^{191}Au could have either value zero or $\pm 1/2$ depending on the kinds of calculations (strong coupling, normal-asymptotic numbers, or pseudo-asymptotic numbers) and on the orbitals ([411]1/2, [530]1/2, or [651]3/2 (6_2 in Fig. 4.6)). If $i = \pm 1/2$ then the signature-partner bands would have the same transition energies (see eq. 4.1). At an energy of about 500 keV (or $\hbar\omega \approx 250$ keV), where the ([411]1/2, $\alpha = -1/2$) orbital crosses the intruder 6_2 orbital (see Fig. 4.6), the transition energies of the second signature-partner band should begin to deviate from the first one. That was exactly what appears to have happened to the weaker, second band mentioned above.

4.3 Conclusion

In conclusion, the SD band in ^{191}Au represents the first experimental evidence concerning the nature of the proton orbitals below Z=80 in superdeformed nuclei. The band may be characterized by either the [411]1/2 or the [530]1/2 proton orbital. This is the first observation of an SD band in this region based on these orbitals. This band has an unexpected and interesting property: it shows an identical band relationship to the yrast (quarter-point energies) SD band in ^{192}Hg and to the SD band in ^{191}Hg*. However, there is no (or very weak) evidence as yet of a signature-partner band. A report on this SD band has been published in Physical Review Letters [73]. This band is very weak and it represents a limit of what can be done with the current generation of Compton-suppressed Ge arrays. A great deal remains to be learned concerning the properties of this SD region and the relationships between the SD bands observed in it. It is important that this region of superdeformation is

extended by continuing to study it with the next generation of detector arrays.

CHAPTER 5. SEARCH FOR RESONANCES IN MULTI-PHOTON FINAL-STATES FROM LOW-ENERGY e^+e^- SCATTERING

5.1 Experimental Procedure

A search was carried out for 2γ and 3γ decay channels of a resonant e^+e^- composite system, which was referred to as photonium. An e^+ source made of ^{68}Ga, in secular equilibrium with its 288-day half-life parent ^{68}Ge, was enclosed inside the cavity of a lead spherical shell. The HERA facility at the Lawrence Berkeley Laboratory was used to detect the γ rays. (The HERA array, which consisted of 20 Compton-suppressed Ge detectors and a 4π, 40-element bismuth germanate (BGO) inner ball, was discussed in chapter 2.) The solid angle of each Ge detector is 82 msr. The angle between a pair of Ge detectors ranged from 37° to 157°. The lead shell had an inner radius of 0.238 cm and an outer radius of 0.476 cm. The positrons of interest for the experiment are emitted in the decay of ^{68}Ga to the ground state of ^{68}Zn. The ground-state decay branch is 97%, with 88% by positron emission, and the positron kinetic endpoint energy is 1.9 MeV [74]. Even for a pure 2-body process, this endpoint energy is above the threshold energy needed to observe the lowest energy GSI resonance (1660 keV) and the three lowest predicted resonances (1351, 1498, and 1659 keV) in photonium [30]. The target-source assembly was positioned at the focal center of HERA so each of the 20 Ge detectors subtended the same solid angle (82 msr).

The source strength at the beginning of the experiment was 67 μCi. The counting took place whenever HERA was available for off-line experiments (i.e., not used for in-beam experiments). The total counting time on HERA using the lead sphere was 94 days (2260 hrs) over a period of 5 months. Additional measurements were carried out using a copper sphere identical to the lead sphere in dimensions and containing 44 μCi of activity. The total counting time using the copper sphere at HERA was 9 days over a one month period. There were not enough data using the copper sphere to have any meaningful analysis. The experiment was terminated by the permanent shut down of HERA in preparation for the construction of Gammasphere.

During the experiments, the energies of the coincident γ rays from the Ge detectors, the time relationship between the first and second γ rays, plus the total energy and multiplicity from the BGO ball were recorded on magnetic tape. The average singles rate in each Ge detector was 12 kHz and the average total coincidence rates were 610 Hz and 12 Hz for 2γ and 3γ coincidences, respectively. A total of 4.9×10^9 double and 9.8×10^7 triple coincidence events were recorded from the 94-d total counting time with the lead sphere. For analysis, the only accepted events were those with no energy deposited in the BGO ball and a multiplicity of two (for 2γ coincidences) or three (for 3γ coincidences) in order to insure that most of the events came from the annihilation of positrons or the decay of photonium. This condition reduced the total number of accepted events to 1.1×10^9 and 1.3×10^7 for the double and triple coincidences, respectively. Also, the events were selected within the timing window of 35 ns. Random coincidence events were selected by setting a chance timing gate about 60 ns from the true timing gate.

5.2 Experimental Results

A prime motivation of this experiment was to measure the invariant mass for photonium decaying into two or three γ rays. An additional motivation was to search for the peaks at 1455 and 1648 keV that were observed by Skalsey and Kolata [29]. It is interesting to note that all previous experiments used an "energy-sum" formula to search for the resonances rather than an "invariant mass" formula. In the present experiments, the data were analyzed using both methods. The restrictions, advantages, and disadvantages of each method are described in the following subsections.

5.2.1 3γ Decay at Rest

The search for 2γ decay of photonium at rest was not possible due to the geometry of HERA since it had no pair of detectors separated by 180°. Therefore, the search was performed only for 3γ decay at rest. In constructing the 3γ energy-sum plots, a sort was first made on all triple-coincidence events. Conditions were imposed on the sorted data such that the three γ rays were coplanar with the source and that their measured total momentum was in the interval [p, p+δp] where p is the total momentum and δp is the deviation from the true value due to the finite solid angles of the Ge detectors such that about 75% of the true decay would be accepted. For decay at rest, p equals zero and the average δp was about 66 keV/c for an 1100 keV resonance and 108 keV/c at 1800 keV. Also, random coincidences were subtracted and any coincident event with a single 511-keV γ ray or with any known γ ray from the ^{68}Ga source was rejected. A number of new, very low intensity γ rays were identified as being emitted in the ^{68}Ga decay. These new results on the level scheme are briefly discussed in the Appendix.

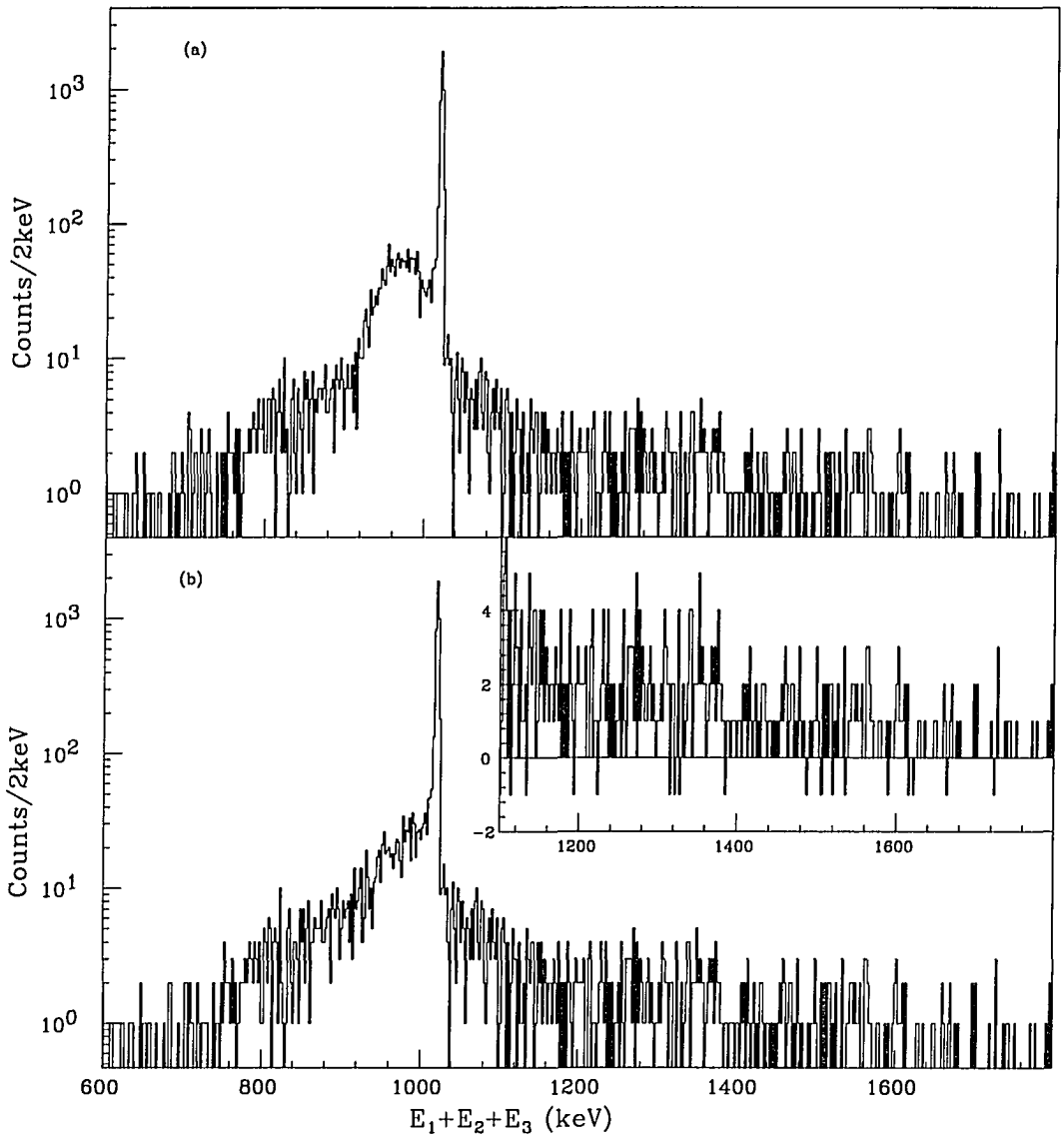

Figure 5.1: (a) Energy-sum spectrum for 3 coincident γ rays. (b) Energy-sum spectrum for 3 coincident γ rays with the rejection of events in which the sum of any two γ rays falls into the window 511$\pm$5 keV. The inset shows the detail of the region above 1.1 MeV on a linear scale

The spectrum for the 3γ energy-sum measured in this work is shown in Fig. 5.1a. The broad bump around 900 keV is due to the scattering of two 511-keV back-to-back γ rays: one γ ray hits a detector, deposits part of its energy and then scatters into a second detector; the second 511-keV γ ray forward scatters from the lead sphere surrounding the source into the third detector. Fig. 5.1b includes an additional condition: rejection of any event in which the sum of any two γ rays falls into the window 511 ± 5 keV. The difference between the two spectra in Fig. 5.1a and Fig. 5.1b is the absence of the broad bump around 900 keV. Fig. 5.1a is similar to the 3γ energy-sum spectrum shown in Ref. [29]. The lack of rejection of the scattering of two 511-keV back-to-back γ rays may explain the broad bump below the 1022-keV peak and the sharp drop of the background above the 1022-keV peak shown in Ref. [29].

The large peak at 1022 keV in Fig. 5.1b is due to the 3γ decay of orthopositronium in the non-metallic material within the hollow metal sphere. It has an energy resolution of 3.7 keV (FWHM). The energy resolution of any photonium peak is assumed to be similar to that of the orthopositronium peak and linearly proportional to the resonant energy. The values of the energy resolutions used in the calculations were 3.7 keV at 1022 keV and 4.8 keV at 2044 keV. The background events can mostly be attributed to coincidences between Compton-scattered γ rays from positron annihilation and the Compton scattering of the 1077-keV γ ray from ^{68}Ga decay. The decay branch to the 1077-keV level in ^{68}Zn is 1.3% abundant. There will also be some events from Compton scattering between detectors since the BGO Compton suppression system is not 100% efficient.

Figure 5.1b shows no evidence for peaks above 1100 keV in the energy sum

spectrum for the 3γ decay of photonium. The region between 1200 keV and 1800 keV is shown in the inset using a linear scale for counts. In particular, no evidence was seen for small peaks at 1455 and 1648 keV reported by Skalsey and Kolata [29].

From the data shown in Fig. 5.1b, upper limits for photonium decaying at rest into 3γ were extracted. A Breit-Wigner line shape and a total angular momentum of $\hbar$ were assumed for a resonant state of mass M. Then the integrated cross-section is given by (for c = speed of light = 1):

$$\int \sigma_{3\gamma}(E)dE = \frac{6\pi^2\hbar^2}{[M^2 - 4m_e^2]} \frac{\Gamma_{3\gamma}\Gamma_{e^+e^-}}{\Gamma}, \tag{5.1}$$

where Γ, $\Gamma_{3\gamma}$, and $\Gamma_{e^+e^-}$ are the total width of the resonance and partial widths for decay into 3γ and e^+e^-, respectively. Furthermore, $\int \sigma_{3\gamma}(E)dE$ can be determined from the data using:

$$\frac{1}{\Gamma}\int \sigma_{3\gamma}(E)dE = \frac{N_{3\gamma}}{C_{3\gamma} \times n_p(e^+) \times n_t(e^-)}, \tag{5.2}$$

where

$N_{3\gamma}$ = counts in the hypothetical peak of the resonance at mass M

$C_{3\gamma}$ = (opening angle factor) $\times$ (γ-ray attenuation factor in lead) $\times$ (detector efficiency)

$n_p(e^+)$ = number of e^+ above the resonance

$n_t(e^-)$ = number of e^- in the target (82 e^- per atom), in unit of barns^{-1}

The "opening angle factor" is the probability of all 3 coincident γ rays getting into 3 detectors. It was calculated using Monte Carlo simulation techniques and the HERA detector geometry. It is interesting to note that out of all 1140 possible combinations of 3 detectors, 62 were coplanar with the source. Of these 62 triplets,

events were retained from only those 26 triplets sensitive to the decay of photonium at rest in or near the Pb sphere.

The number of e^- in the target is calculated using an effective thickness in the Pb target. This is approximately the average distance an e^+ with kinetic energy $E_{res} + \Gamma/2$ will travel before its energy decreases to $E_{res} - \Gamma/2$. The e^+ can excite the resonance at E_{res} only within this thickness. Thus,

$$n_t(e^-) = \frac{Z}{A} N_A \Gamma (\frac{dE_{loss}}{dx})^{-1}, \tag{5.3}$$

where dE_{loss}/dx = energy loss per unit thickness and N_A = Avogadro's constant.

To obtain an upper limit for $N_{3\gamma}$, the following analysis was used: Assume that all the events (after subtracting the chance background) with total energy greater than 1022 keV in the spectrum are from the decay of an isolated state of photonium. This portion of the spectrum is then fitted to a Gaussian, with the centroid held fixed at a certain energy and the FWHM = [2.6 keV + 1.1×10^{-3} $E_{centroid}$]. From the fit, the area N_o and its rms uncertainty σ_o are obtained. The 95% upper limit on N_o is then calculated assuming the distribution of N_o to be Gaussian and σ_o to be its standard deviation. From the Gaussian, the 95% confidence level upper limit of $N_{3\gamma}$ is taken to be the point in the distribution dividing the physical region (positive N_o values) into two subareas—one with the lower 95% area and the other with the higher 5% area [75]. The process is then repeated in 1-keV steps of the hypothetical resonance across the energy range.

The resulting upper limits of the "strength", $\int \sigma_{3\gamma}(E)dE$, and the partial width, $\Gamma_{3\gamma}\Gamma_{e^+e^-}/\Gamma$, of the resonance decaying at rest into 3γ are shown in Fig. 5.2. These limits were deduced from the data in Fig. 5.1b. These results can be compared with those of Skalsey and Kolata [29], who gave results of 95% confidence level upper

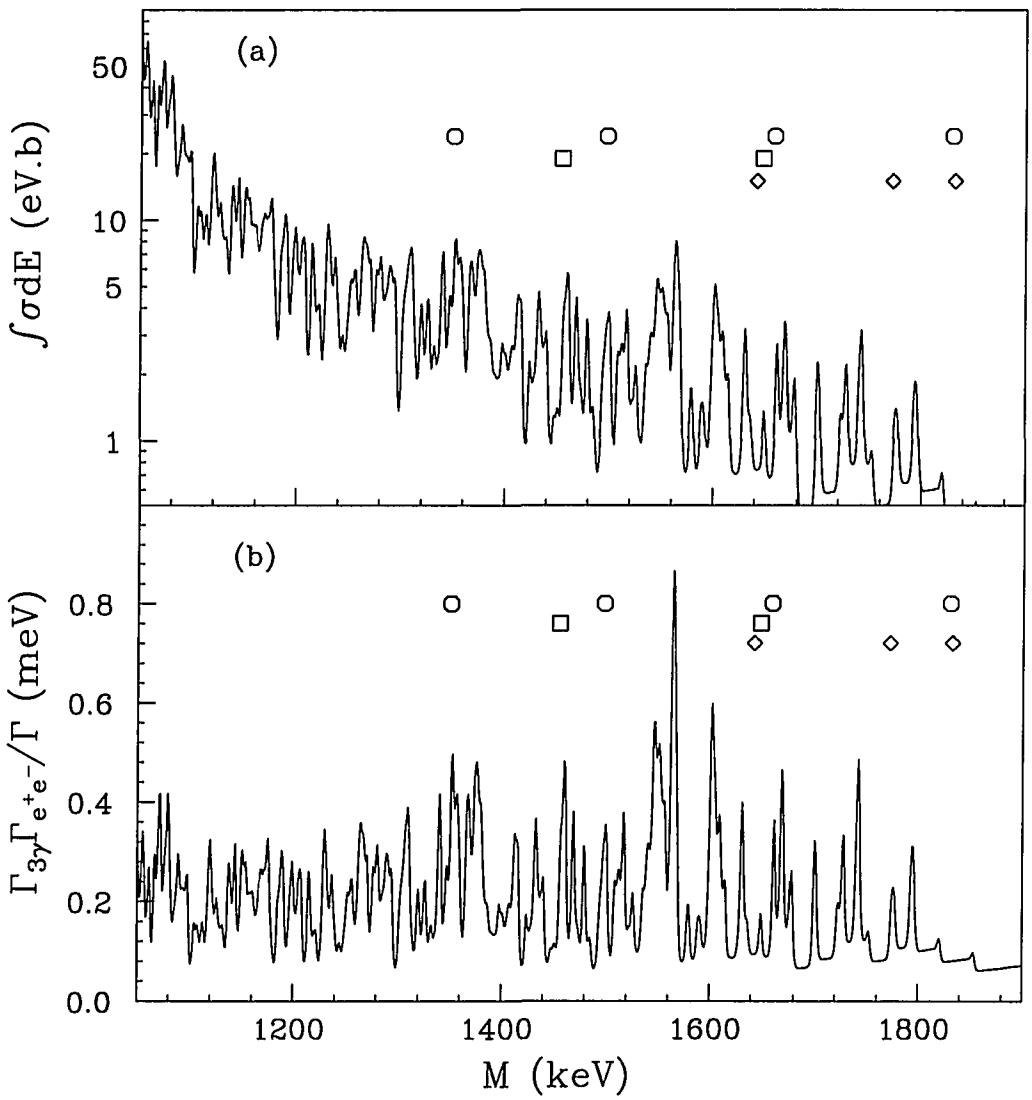

Figure 5.2: (a) Upper limits (95%) of the total strength $\int \sigma_{3\gamma}(E)dE$ for a resonance of mass M decaying at rest in the range 1050-1900 keV. Diamonds: energies of peaks seen by EPOS and ORANGE [8, 10]; squares: energies of peaks seen in the data reported by Skalsey and Kolata [29]; circles: predicted energies of photonium peaks [30]. (b) Upper limits (95%) of the partial width $\Gamma_{3\gamma}\Gamma_{e^+e^-}/\Gamma$. Comparison of the present upper limits with those of Ref. [29] is made in the text

limits for $\Gamma_{3\gamma}\Gamma_{e^+e^-}/\Gamma$ at three energies: 1500, 1540, and 1640 keV. At these energies, the present upper limits are lower by factors of about 20, 20, and 70, respectively. Thus, overall, the present results in Fig. 5.2 decrease the upper limits by more than an order of magnitude.

5.2.2 2γ and 3γ Energy-Sum Masses

A search for photonium decaying in flight into 2γ and 3γ was made. This was possible since there are many combinations of two detectors in HERA with angles between them less than 180° and three detectors not lying in a plane containing the source.

If it is assumed that photonium is formed from a moving e^+ and a stationary, free e^- which decays spontaneously into nγ, then an "energy-sum" plot could be generated. This type of plot is motivated by the fact that the directions and energies of the two (or three) decay γ rays are not fixed, but the sum of the two (or three) energies is uniquely related to the total momentum and mass M. Therefore, a narrow resonance would occur at the position $M = \sqrt{2m_e \sum_j^n E_j}$ as a sharp peak above a positron-annihilation-in-flight background in the $(\sum_j^n E_j)$ spectrum. Such a sharp peak would have a width (FWHM) of about 4 keV due to the intrinsic detector resolution. The upper limits are also calculated using the Breit-Wigner formula:

$$\int \sigma_{n\gamma}(E)dE = \frac{2\pi^2\hbar^2(2J_n+1)}{[M^2-4m_e^2]}\frac{\Gamma_{n\gamma}\Gamma_{e^+e^-}}{\Gamma}, \tag{5.4}$$

where J_n is the total angular momentum of the resonant state and other values are the same as in Eq. 5.1. The value $\sigma_{n\gamma}$ can be calculated using:

$$\frac{1}{\Gamma}\int \sigma_{n\gamma}(E)dE = \frac{N_{n\gamma}}{C_{n\gamma} \times n_p(e^+) \times n_t(e^-)}, \tag{5.5}$$

which is similar to Eq. 5.2.

In the calculations of $n_t(e^-)$, all the K, L, and M shell electrons were excluded. For such tightly bound electrons, their Fermi motion would smear out the resonant peak. Use of less than the full electron number was also done in Ref. [26], where 75% of the total electrons were used. The cutoff imposed here leads to the use of only 54 of the 82 electrons in lead (66% of the total number of electrons). This makes the present upper limit larger by a factor of 82/54, which can be regarded as a conservative choice.

The energy-sum spectra, unlike the case for 3γ decay at rest, contain a large background due to the annihilation-in-flight of positrons. The upper limits of $N_{2\gamma}$ and $N_{3\gamma}$ are calculated by assuming the peak's area to be zero and the standard deviation to be the statistical uncertainty of the background. The 3σ upper limits for $N_{2\gamma}$ and $N_{3\gamma}$ are then just three times the standard deviation.

The momentum restriction set on these spectra was the same as that in subsection 5.2.1, i.e., the measured total momentum was in the interval [p–δp, p+δp]. For these energy-sum spectra, $\mathrm{p} = \sqrt{E_{tot}^2 - M^2} = \sqrt{E_{tot}^2 - 2mE_{tot}}$, and δp was chosen so that 95% of true decay events would satisfy the imposed condition. For 2γ decay, this δp corresponds to a deviation of about 9.5° in the separation angle of detector pairs. For 3γ decay, δp varies greatly for different energies and different detector combinations. On the average, δp was about 200 keV/c for a hypothetical resonance at 1100 keV and about 800 keV/c for a hypothetical resonance at 1700 keV.

The spectrum and the upper limits of 2γ decay are shown in Figs. 5.3 and 5.4. From the positron kinetic endpoint energy of 1.9 MeV, the smallest angle between a pair of detectors possible for two coincident γ rays is 73°. However, the probability

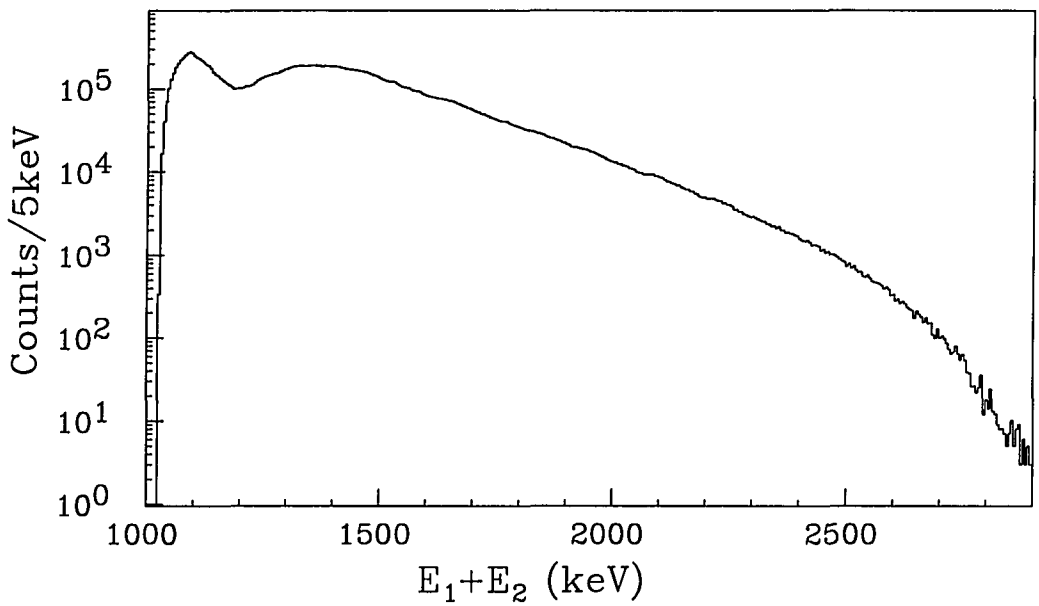

Figure 5.3: Energy-sum spectrum for 2 coincident γ rays

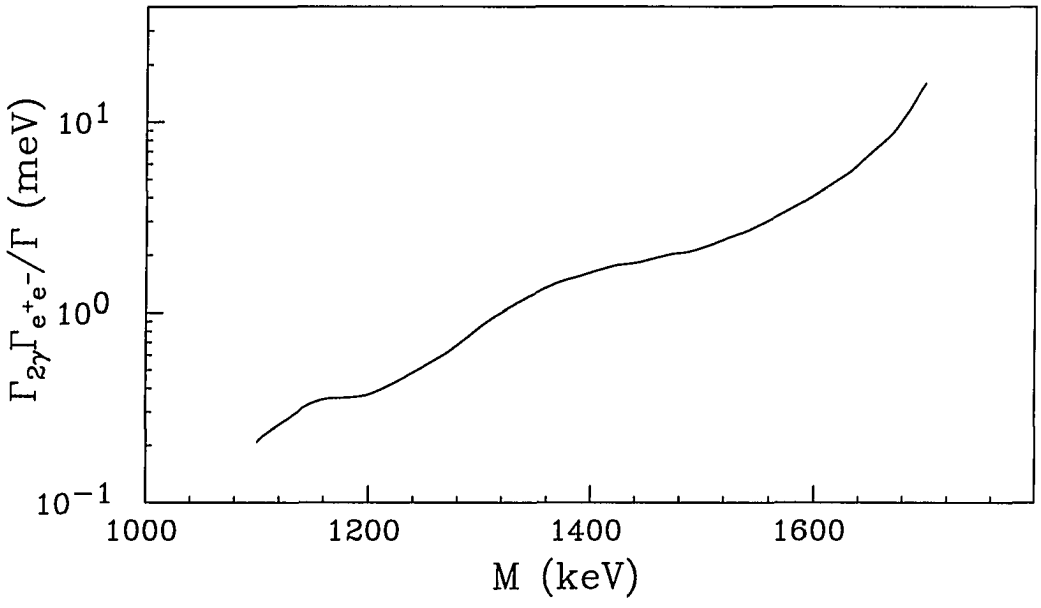

Figure 5.4: Upper limits (3σ) of the partial width for a resonance of mass M decaying into 2γ using the energy-sum formula in the range 1100-1700 keV

of two coincident γ rays (decay from photonium) getting into pairs of detectors with small angles between them is small. Most of the events recorded in those pairs of detectors were from coincidences between Compton scattered γ rays from ^{68}Ga decay and not from photonium decay. Therefore, only the data from detector pairs whose separations ranged from 103° to 157° was used. This reduced the combinations of detector pairs from a total of 190 (out of 20 detectors) to 88. Because of HERA's geometry, which did not have a smooth distribution of detector combinations, the 2γ and 3γ spectra are somewhat "bumpy". The two broad bumps at about 1100 keV and 1300 keV in Fig. 5.3 are caused by annihilation-in-flight in two sets of angles, 152°-157° and 103°-123°, respectively. There were no pairs of detectors with angles between 123° and 152°. Again, there is no photonium peak seen above the annihilation-in-flight background. In the energy range of 1100-1600 keV, these limits in Fig. 5.4 are slightly better than the previous best upper limits, which were reported in Ref. [28] using sources of ^{22}Na and ^{27}Si.

The spectra for 3γ decay and its limits are shown in Figs. 5.5 and 5.6. The conditions for these are the same as for the 3γ coplanar data in subsection 5.2.1 but without the coplanarity requirement. There has been no previously reported search for resonances with mass in the range 1100-1350 keV decaying in flight into 3γ. Thus, the present results provide, for the first time, the upper limits for resonances decaying in flight to 3γ in the range 1100-1350 keV.

5.2.3 2γ and 3γ Invariant Masses

A search for photonium decaying in flight into 2γ and 3γ using the invariant mass formula was also made. From energy and momentum conservation, the invariant mass

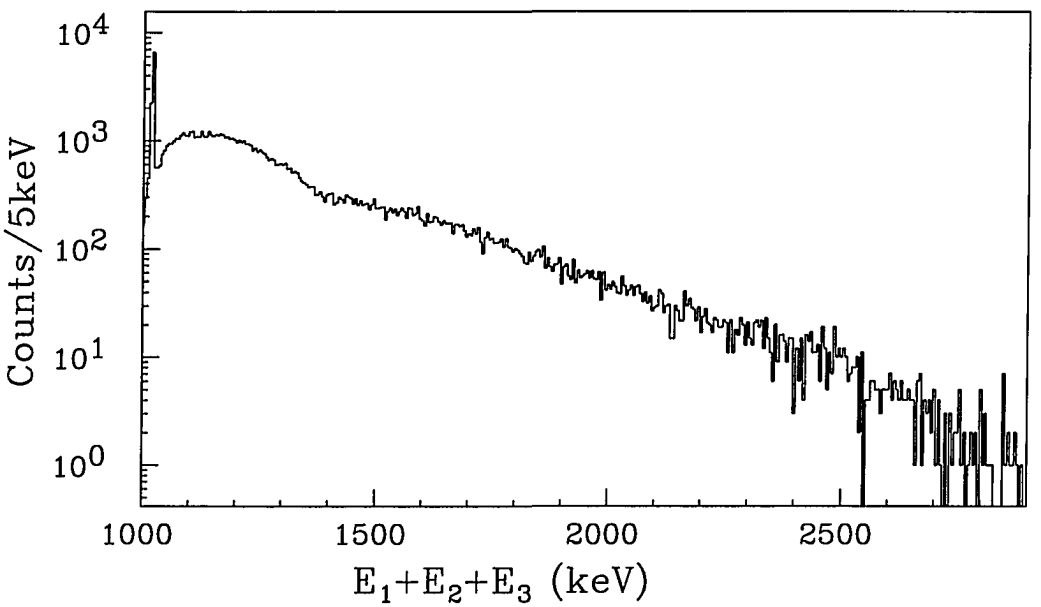

Figure 5.5: Energy-sum spectrum for 3 coincident γ rays

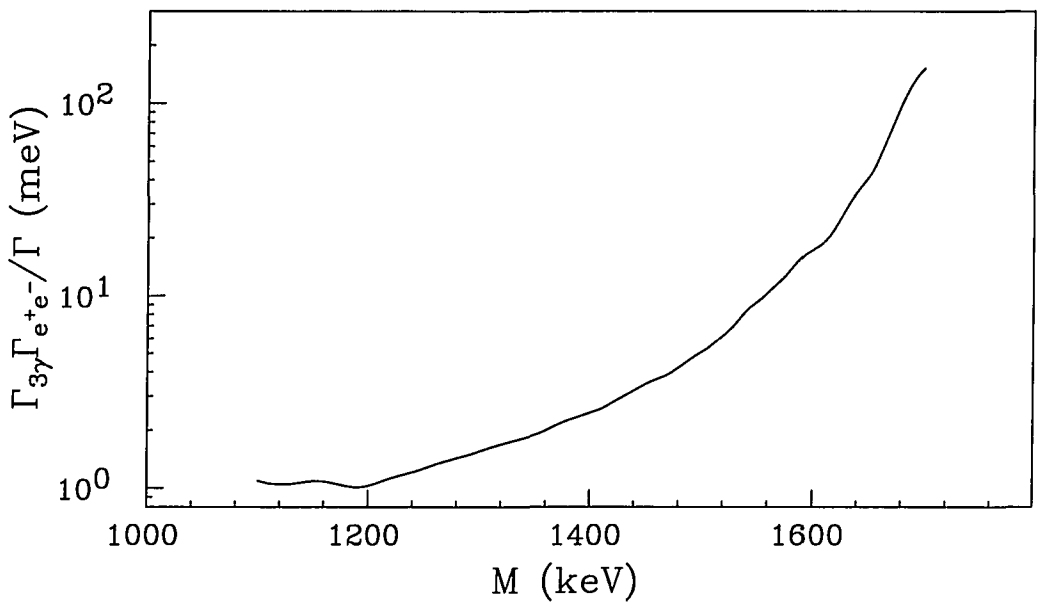

Figure 5.6: Upper limits (3σ) of the partial width for a resonance of mass M decaying into 3γ using the energy-sum formula in the range 1100-1700 keV

formula for photonium decaying into nγ is given by:

$$M = 2\sqrt{\sum_{j>i}^{n} E_i E_j \sin^2 \frac{\Theta_{ij}}{2}}, \tag{5.6}$$

where Θ_{ij} is the angle between detectors i and j and E_i is the energy of the $i^{th}\gamma$ ray. (c = 1 in Eq. 5.6.)

In principle, the invariant mass formula has an advantage over the energy-sum formula in that the motion of the target electrons does not affect the resolution of the peak. Therefore, there is no need to assume that the momentum of photonium is fixed. In addition, all of the electrons in the target can be used to calculate the cross-section of the resonant state. However, the measured line shape will have a large FWHM in mass due to the finite solid angle subtended by each detector because of the relatively large half-cone angle (8.25°). From the geometry of HERA, Monte Carlo techniques were used to simulate the distributions of FWHM(M) for each angle Θ_{ij} for 2γ decay. These results can be written as

$$\frac{\mathrm{FWHM}(M)}{M} \approx \frac{\frac{1}{2}\mathrm{FWHM}(\Theta_{ij})}{\tan(\Theta_{ij}/2)} \approx \frac{\sin 6.5°}{\tan(\Theta_{ij}/2)}. \tag{5.7}$$

The Monte Carlo distributions show that the values of FWHM(Θ_{ij}) are almost independent of Θ_{ij} and have an average value of about $2\sin 6.5°$. The value of FWHM(M)/M is about 2–9% for Θ_{ij} between 160° and 100° for the 2γ decay case.

The spectrum of the 2γ invariant mass is shown in Fig. 5.7a. This spectrum is the sum of the data of all pairs of detectors with angles from 103° to 157° (88 out of 190 possible combinations of two detectors). For each set of data at each angle, a search was made for photonium peaks assuming the FWHM of the peaks to have the values corresponding to Eq. 5.7 above. No photonium peak was found. The data sets were also summed into two subgroups with angles from 103°-123° and 152°-157°.

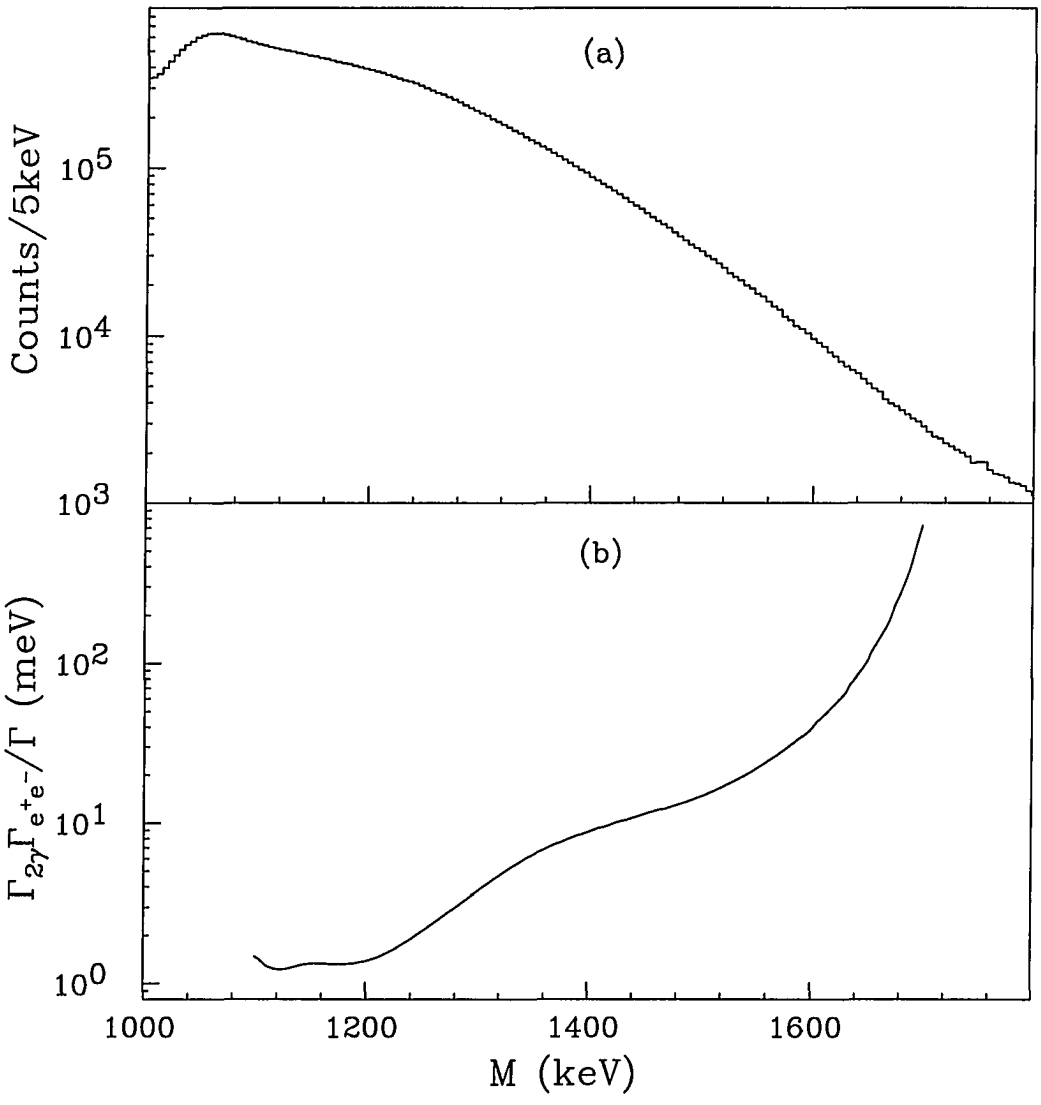

Figure 5.7: (a) Invariant mass spectrum for 2 coincident γ rays. (b) Upper limits (3σ) of the partial width for a resonance of mass M decaying into 2γ using the invariant mass formula in the range 1100-1700 keV

The search for photonium from these subgroups was also carried out (with width of about 2.5% of the hypothetical resonance energy for the 152°-157° subgroup and 7.5% for the 103°-123° subgroup) and no peak was found. All the data from all the angles from 103° to 157° were also summed (Fig. 5.7a). This would give a width of about 5% of the resonance energy. This search did not find any peak that could be attributed to the decay of photonium. The results of the upper limits of the partial width are shown in Fig. 5.7b. Upper limits were calculated for each angle. In no case were the limits significantly lower than those shown in Fig. 5.7b and, in most cases, were significantly higher.

For the 3γ decay case, a corresponding Monte Carlo study shows that the FWHM(M) are found to be $\approx$ 34 keV for a hypothetical resonance at 1100 keV and $\approx$ 130 keV at 1700 keV. The 3γ invariant mass spectrum is shown in Fig. 5.8a. The conditions for this are the same as for the energy-sum spectrum (Fig. 5.1), but without the momentum restriction and coplanarity requirement. This means that all 1140 3γ combinations were used. The width limits are shown in Fig. 5.8b.

As the preceding discussion shows, the broad width of a fast moving resonance indicates that invariant mass spectra are not well suited for searches for weak resonances unless the background is suitably suppressed. With the resolution of the present experiments, no resonance above the positron annihilation-in-flight background was observed. These results are presented here in this invariant mass form, as well as the energy-sum form, since it is important to know the upper limits for any potential phenomena related to the GSI experiments under as wide a set of conditions as possible.

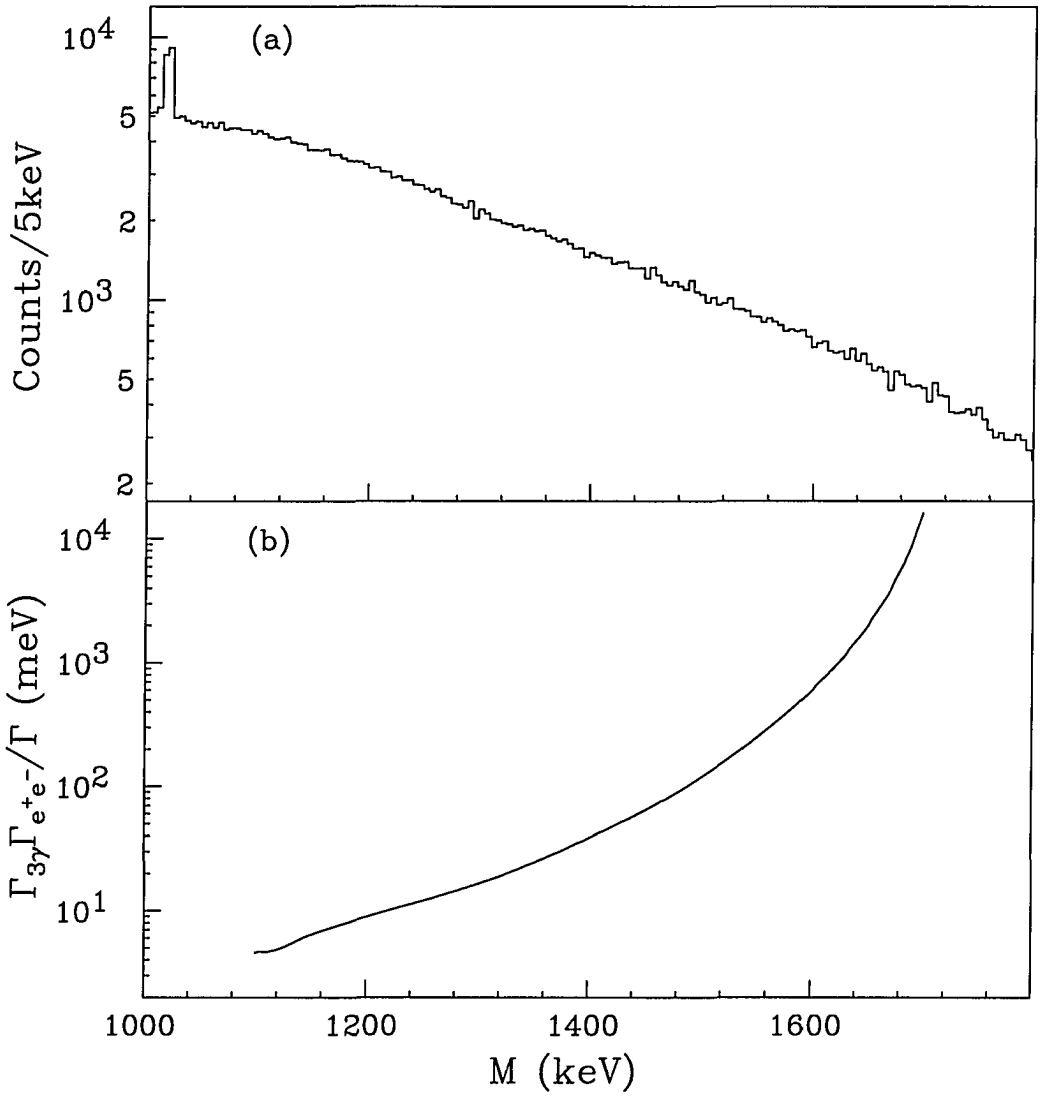

Figure 5.8: (a) Invariant mass spectrum for 3 coincident γ rays. (b) Upper limits (3σ) of the partial width for a resonance of mass M decaying into 3γ using the invariant mass formula in the range 1100-1700 keV

5.3 Summary

In summary, the large-acceptance angle feature of the multi-γ-ray detector HERA was used to search for evidence for photonium decay (at rest and in flight) produced from e^+e^- scattering using a Pb target, namely $e^+e^- \rightarrow X \rightarrow n\gamma$ where $n = 2$ or 3.

No evidence was seen for photonium (X) decay into 2γ or 3γ from the present experiments. The upper limits for both stopped and moving photonium are given here. For stopped photonium, the upper limits for the 3γ decay mode are lowered by more than an order of magnitude. For the case of photonium in motion, the upper limits for 2γ decay in the energy range 1100-1600 keV are improved. The present results provide, for the first time, upper limit results for 3γ decay in the energy range 1100-1350 keV.

BIBLIOGRAPHY

[1] U. Hagemann, K.H. Kaun, W. Neubert, W. Schulze, and F. Stary, Nucl. Phys. A197, 111 (1972).

[2] R.M. Latimer, G.E. Gordon, T.D. Thomas, J. Inorg. Nuclear Chem. 17, 1 (1961).

[3] R.W. Hoff, F. Asaro, I. Perlman, J. Inorg. Nuclear Chem. 25, 1303 (1963).

[4] G. Bastin, C.F. Liang, CSNSM, 1973-1975 Prog. Rept., p.35 (1975).

[5] R.V.F. Janssens and T.L. Khoo, Ann. Rev. Nucl. Part. Sci. 41, 321 (1991), and references therein.

[6] R.R. Chasman, Phys. Lett. B219, 227 (1989).

[7] S. J. Krieger, P. Bonche, M.S. Weiss, J. Meyer, H. Flocard, and P.H. Heenen, Nucl. Phys. A542, 43 (1992).

[8] T. Cowan, H. Blacke, K. Bethge, H. Bokemeyer, H. Folger, J.S. Greenberg, K. Sakaguchi, D. Schwalm, J. Schweppe, K.E. Stiebing, and P. Vincent, Phys. Rev. Lett. 56, 444 (1986); T. Cowan and J.S. Greenberg in *Physics of Strong Fields*, ed. by W. Greiner (Plenum Press, New York, 1987), p. 111.

[9] P. Salabura, H. Backe, K. Bethge, H. Bokemeyer, T.E. Cowan, H. Folger, J.S. Greenberg, K. Sakaguchi, D. Schwalm, J. Schweppe, and K.E. Stiebing, Phys. Lett. B245, 153 (1990).

[10] W. Koenig, E. Berdermann, F. Bosch, S. Huchler, P. Kienle, C. Kozhuharov, A. Schroter, S. Schuhbeck, and H. Tsertos, Phys. Lett. B218, 12 (1989).

[11] A. Scherdin, J. Reinhardt, W. Greiner, and B. Muller, Rep. Prog. Phys. 54, 1 (1991), and references therein.

[12] K.A. Erb, I.Y. Lee, and W.T. Milner, Phys. Lett. B181, 52 (1986).

[13] K. Maier, E. Widmann, W. Bauer, F. Bosch, J. Briggmann, H.D. Carstanjen, W. Decker, J. Diehl, R. Feldmann, B. Keyerleber, D. Maden, J. Major, H.E. Schaefer, A. Seeger, and H. Stoll, Zeit. Phys. A330, 173 (1988).

[14] Chr. Bargholtz, L. Holmberg, K.E. Johansson, D. Liljequist, P.E. Tegner, and D. Vojdani, Phys. Rev. C40, 1188 (1989).

[15] M. Sakai, Y. Fujita, M. Imamura, K. Omata, S. Ohya, and T. Miura, Phys. Rev. C38, 1971 (1988); M. Sakai, Y. Fujita, M. Imamura, K. Omata, S. Ohya, S. Muto, T. Miura, Y. Gono, and S. Chojnacki, Phys. Rev. C44, R944 (1991); M. Sakai, Y. Fujita, M. Imamura, K. Omata, Y. Gono, T. Miura, S. Shimizu, and S. Chojnacki, Phys. Rev. C47, 1595 (1993).

[16] R. Peckhaus, Th.W. Elze, and Th. Dresel, Phys. Rev. C36, 83 (1987).

[17] T.F. Wang, I. Ahmed, S.J. Freedman, R.V.F. Janssens, and J.P. Schiffer, Phys. Rev. C36, 2136 (1987);

[18] E. Lorenz, G. Mageras, U. Stiegler, and I. Huszar, Phys. Lett. B214, 10 (1988).

[19] S.M. Judge, B. Krusche, K. Schreckenbach, H. Tsertos, and P. Kienle, Phys. Rev. Lett. 65, 972 (1990).

[20] H. Tsertos, C. Kozhuharov, P. Armbruster, P. Kienle, B. Krusche, and K. Schreckenbach, Zeit. Phys. A331, 103 (1988), Phys. Rev. D40, 1397 (1989).

[21] H. Tsertos, P. Kienle, S.M. Judge, and K. Schreckenbach, Phys. Lett. B266, 259 (1991).

[22] S.H. Connell, R.W. Fearick, A. Hoernle, E. Sideras-Haddad, and J.P.F. Sellschop, Phys. Rev. Lett. 60, 2242 (1988).

[23] J.D. Fox, K.W. Kemper, P.D. Cottle, and R.A. Zingarelli, Phys. Rev. C39, 288 (1989).

[24] T.J. Radcliffe, T.K. Alexander, G.C. Ball, H.C. Evans, J.R. Leslie, H.B. Mak, W. McLatchie, P. Skensved, and A.T. Stewart, Phys. Rev. C42, R2275 (1990).

[25] W.H. Trzaska, H. Dejbakhsh, S.B. Dutta, Q. Li, and T.M. Cormier, Phys. Lett. B269, 54 (1991).

[26] M. Minowa, S. Orito, M. Tsuchiaki, and T. Tsukamoto, Phys. Rev. Lett. 62, 1091 (1989).

[27] E. Widmann, W. Bauer, S. Connell, L. Maier, A. Seeger, H. Stoll, and F. Bosch, Zeit. Phys. A340, 340 (1991).

[28] J. Kramp, Ph.D. Dissertation, Heidelberg (1989) (unpublished); J. Kramp, J. Gerl, D. Habs, D. Schwalm, and P. Thirolf, Proc. of the XXIVth Rencontre de Moriond, Les Arcs, Savoie, France, Jan 21-28, 1989.

[29] M. Skalsey and J.J. Kolata, Phys. Rev. Lett. 68, 456 (1992).

[30] J.R. Spence and J.P. Vary, Phys. Lett. B254, 1 (1991).

[31] C.J. Benesh, D.K. Ross and J.P. Vary, Zeit. Phys. A344, 67 (1992).

[32] D.K. Ross and J.P. Vary, Zeit. Phys. A344, 443 (1993).

[33] T. Yamazaki, Nucl. Data 3, 1 (1967).

[34] E. Der Mateosian and A.W. Sunyar, Atomic Data and Nucl. Data Tables 13, 391 (1974).

[35] K.S. Krane, R.M. Steffen, and R.M. Wheeler, Nucl. Data Tables 11, 351 (1973).

[36] J.E. Draper, Nucl. Instrum. Methods A247, 481 (1986).

[37] Nucl. Data Sheets 60, 543 (1990).

[38] M. Pautrat, G. Albouy, J.C. David, J.M. Lagrange, N. Poffé, C. Roulet, H. Sergolle, J. Vanhorenbeeck, and H. Abou-Leila, Nucl. Phys. A201, 449 (1973); G. Albouy, G. Auger, J.M. Lagrange, M. Pautrat, H. Richel, C. Roulet, H. Sergolle, and J. Vanhorenbeeck, Nucl. Phys. A303, 521 (1978).

[39] M. Pautrat, J.M. Lagrange, J.S. Dionisio, Ch. Vieu, and J. Vanhorenbeeck, J. Phys. (London) G12, 1285 (1986); M. Pautrat, J.M. Lagrange, J.S. Dionisio, Ch. Vieu, and J. Vanhorenbeeck, Nucl. Phys. A443, 172 (1985).

[40] T. Chapuran, K. Dybdal, D.B. Fossan, T. Lonnroth, W.F. Piel, Jr., D. Horn, and E.K. Warburton, Phys. Rev. C33,130 (1986).

[41] H. Helppi, S.K. Saha, P.J. Daly, S.R. Faber, T.L. Khoo, and F.M. Bernthal, Phys. Rev. C23, 1446 (1981).

[42] C. Stenzel, H. Grawe, H. Hass, H. E. Mahnke, and K.H. Maier, Z. Phys. A322, 83 (1985).

[43] S.K. Saha, H. Helppi, P.J. Daly, S.R. Faber, T.L. Khoo, and F.M. Bernthal, Phys. Rev. C16, 2159 (1977).

[44] C.G. Linden, I. Bergstrom, J. Blomqvist, K.G. Rensfelt, H.Sergolle, and K. Westerberg, Z. Phys. A277, 273 (1976).

[45] K.H. Kaun, W. Neubert, W. Schultze, F. Stary, L.K. Peker, and E.I. Volmyanski, Joint Institute for Nuclear Research, Dubna, USSR, Preprint E6-6808 (1972).

[46] B.V. Thirumala Rao, R. Broda, G. Gunther, A. Kleinrahm, and M. Ogawa, Nucl. Phys. 362, 71 (1981).

[47] T. Lonnroth, B. Fant, K. Fransson, A. Kallberg, and K.A. Pettersson, Phys. Scr. 233, 774 (1981).

[48] T. Lonnroth, L. Vegh, K. Wikstrom, and B. Fant, Z. Phys. A287, 307 (1978).

[49] N. Roy, J.A. Becker, E.A. Henry, M.J. Brinkman, M.A. Stoyer, J.A. Cizewski, R.M. Diamond, M.A. Deleplanque, F.S. Stephens, C.W. Beausang, and J.E. Draper, Phys. Rev. C47, R930 (1993).

[50] B. Cederwall, M.A. Deleplanque, F. Azaiez, R.M. Diamond, P. Fallon, W. Korten, I.Y. Lee, A.O. Macchiavelli, J.R.B. Oliveira, F.S. Stephens, W.H. Kelly, D.T. Vo, J.A. Becker, M.J. Brinkman, E.A. Henry, J.R. Hughes, A. Kuhnert, M.A. Stoyer, T.W. Wang, J.E. Draper, C. Duyar, E. Rubel, and J. deBoer, Phys. Rev. C47, R2443 (1993).

[51] B. Fant, R.J. Tanner, P.A. Butler, A.N. James, G.D. Jones, R.J. Poynter, C.A. White, K.L. Ying, D.J.G. Love, J. Simpson, and K.A. Connell, J. Phys. G17, 319 (1991).

[52] A. Kuhnert, M.A. Stoyer, J.A. Becker, E.A. Henry, M.J. Brinkman, S.W. Yates, T.W. Wang, J.A. Cizewski, F.S. Stephens, M.A. Deleplanque, R.M. Diamond, A.O. Macchiavelli, J.E. Draper, F. Azaiez, W.H. Kelly, and W. Korten, Phys. Rev. C46, 133 (1992).

[53] R.M. Kieder, A. Neskakis, M. Muller-Veggian, Y. Gono, C. Meyer-Boricke, S. Beshai, K. Fransson, C.G. Linden, and Th. Lindblad, Nucl. Phys. A299, 255 (1978).

[54] J.R. Hughes, Y. Liang, R.V.F. Janssens, A. Kuhnert, J.A. Becker, I. Ahmad, I.G. Bearden, M.J. Brinkman, J. Burde, M.P. Carpenter, J.A. Cizewski, P.J. Daly, M.A. Deleplanque, R.M. Diamond, J.E. Draper, C. Duyar, B. Fornal, U. Garg, Z.W. Grabowski, E.A. Henry, W. Hesselink, N. Kalantar-Nayestanaki, W.H. Kelly, T.L. Khoo, T. Lauritsen, R.H. Mayer, D. Nissius, J.R.B. Oliveira, A.J.M. Plompen, W. Revial, E. Rubel, F. Soramel, F.S. Stephens, M.A. Stoyer, D. Vo, and T.W. Wang, Phys. Rev. C47, R1337 (1993).

[55] R.M. Clark, R. Wadsworth, E.S. Paul, C.W. Beausang, I. Ali, A. Astier, D.M. Cullen, P.J. Dagnall, P. Fallon, M.J. Joyce, M. Meyer, N. Redon, P.H. Regan, J.F. Sharpey-Schafer, W. Nazarewicz, and R. Wyss, Z. Phys. A342, 371 (1992).

[56] R.M. Clark, R. Wadsworth, E.S. Paul, C.W. Beausang, I. Ali, A. Astier, D.M. Cullen, P.J. Dagnall, P. Fallon, M.J. Joyce, M. Meyer, N. Redon, P.H. Regan, W. Nazarewicz, and R. Wyss, Phys. Lett. B275, 247 (1992).

[57] G. Baldsiefen, H. Hubel, D. Mehta, B.V. Thirumala Rao, U. Birkental, G. Frohlingsdorf, M. Neffgen, N. Nenoff, S.C. Pancholi, N. Singh, W. Schmitz, K. Theine, P. Willsau, H. Grawe, J. Heese, H. Kluge, K.H. Maier, M. Schramm, R. Schubart, and H.J. Maier, Phys. Lett. B298, 54 (1993).

[58] G. Baldsiefen, H. Hubel, F. Azaiez, C. Bourgeois, D. Hojman, A. Korichi, N. Perrin, and H. Sergolle, Z. Phys. A342, 371 (1992).

[59] R.M. Clark, R. Wadsworth, F. Azaiez, C.W. Beausang, A.M. Bruce, P.J. Dagnall, P. Fallon, P.M. Jones, M.J. Joyce, A. Korichi, E.S. Paul, and J.F. Sharpey-Schafer, J. Phys. G19, L57 (1993).

[60] G. Baldsiefen, U. Birkental, H. Hubel, N. Nenoff, B.V. Thirumala Rao, P. Willsau, J. Heese, H. Kluge, K.H. Maier, R. Schubart, and S. Frauendorf, Phys. Lett. B298, 54 (1993).

[61] P. Ring and P. Schuck *The nuclear many-body problem* (Springer-Verlag, New York, 1980), p. 587–590.

[62] Y. Gono, R.M. Lieder, M. Muller-Veggian, A. Neskakis, and C. Mayer-Boricke, Phys. Rev. Lett. 37, 1123 (1976); Y. Gono, R.M Lieder, M. Muller-Veggian, and A. Neskakis, Nucl. Phys. A327, 269 (1979).

[63] M.P. Carpenter, R.V.F. Janssens, E.F. Moore, I. Ahmad, P.B. Fernandez, T.L. Khoo, F.L.H. Wolfs, D. Ye, K.B. Beard, U. Garg, M.W. Drigert, Ph. Benet, R. Wyss, W. Satula, W. Nazarewicz, and M.A. Riley, Phys. Lett. B240, 44 (1990).

[64] J.A. Becker, N. Roy, E.A. Henry, M.A. Deleplanque, C.W. Beausang, R.M. Diamond, J.R. Draper, F.S. Stephens, J.A. Cizewski, and M.J. Brinkman, Phys. Rev. C41, R9 (1990).

[65] D. Ye, R.V.F. Janssens, M.P. Carpenter, E.F. Moore, R.R. Chasman, I. Ahmad, K.B. Beard, Ph. Benet, M.W. Drigert, P.B. Fernandez, U. Garg, T.L. Khoo, S.L. Ridley, and F.L.H. Wolfs, Phys. Rev. C41, 13 (1990).

[66] R. Wyss, J. Nyberg, A. Johnson, R. Bengtsson, and W. Nazarewicz, Phys. Lett. B215, 211 (1988).

[67] W. Nazarewicz, J. Dudek, R. Bengtsson, T. Bengtsson, and I. Ragnarsson, Nucl. Phys. A435, 397 (1985).

[68] J.E. Draper, F.S. Stephens, M.A. Deleplanque, W. Korten, R.M. Diamond, W.H. Kelly, F. Azaiez, A.O. Macchiavelli, C.W. Beausang, E. Rubel, J.A. Becker, N. Roy, E.A. Henry, M.J. Brinkman, A. Kuhnert, and S.W. Yates, Phys. Rev. C42, R1791 (1990).

[69] J.A. Becker, E.A. Henry, A. Kuhnert, T.F. Wang, S.W. Yates, R.M. Diamond, F.S. Stephens, J.E. Draper, W. Korten, M.A. Deleplanque, A.O. Macchiavelli,

F. Azaiez, W.H. Kelly, J.A. Cizewski, and M.J. Brinkman, Phys. Rev. C46, 889 (1992).

[70] F.S. Stephens, M.A. Deleplanque, J.E. Draper, R.M. Diamond, A.O. Macchiavelli, C.W. Beausang, W. Korten, W.H. Kelly, F. Azaiez, J.A. Becker, E.A. Henry, S.W. Yates, M.J. Brinkman, A. Kuhnert, and J.A. Cizewski, Phys. Rev. Lett. 65, 301 (1990).

[71] A. Bohr, I. Hamamoto, and Ben R. Mottelson, Phys. Scr. 26, 267 (1982).

[72] E.F. Moore, R.V.F. Janssens, R.R. Chasman, I. Ahmad, T.L. Khoo, F.L.H. Wolfs, D. Ye, K.B. Beard, U. Garg, M.W. Drigert, Ph. Benet, Z.W. Grabowski, and J.A. Cizewski, Phys. Rev. Lett. 63, 360 (1989).

[73] D.T. Vo, W.H. Kelly, F.K. Wohn, J.C. Hill, M.A. Deleplanque, R.M. Diamond, F.S. Stephens, J.R.B. Oliveira, J. Burge, A.O. Macchiavelli, J. deBoer, B. Cederwall, I.Y. Lee, P. Fallon, J.A. Becker, E.A. Henry, M.J. Brinkman, A. Kuhnert, M.A. Stoyer, J.R. Hughes, J.E. Draper, C. Duyar, and E. Rubel, Phys. Rev. Lett. 71, 340 (1993).

[74] *Table of Isotopes*, 7th ed., edited by C. Lederer and V.S. Shirley (Wiley, New York, 1978), p. 216.

[75] L. Lyons, *Statistics for nuclear and particle physicists* (Cambridge Univ. Press, London, 1986), p. 78–80.

[76] H.K. Carter, J.H. Hamilton, A.V. Ramayya, and J.J. Pinajian, Phys. Rev. 174, 1329 (1968).

[77] K. Vaughan, A.H. Sher, and B.D. Pate, Nucl. Phys. A132 561 (1969).

[78] W.F. Slot, G.H. Dulfer, H. Van Der Molen, and H. Verheul, Nucl. Phys. A186 28 (1972).

[79] J. Lange, J.H. Hamilton, and P.E. Little, Phys. Rev. C7 177 (1973).

ACKNOWLEDGMENTS

The author has been inspired and encouraged by the support of many people for their assistance. The author wishes to express his sincere thanks to all members of the ISU/LBL/LLNL/UC-Davis high-spin nuclear physics collaboration for their assistance and encouragement leading to the completion of this project. Additional thanks and appreciation is expressed to the following individuals:

Dr. Fred K. Wohn, who, as thesis advisor, agreed to let the author work with other groups outside his field. His unselfishness was the primary reason this project was started and is being completed.

Dr. William H. Kelly for helping to start this project and for his guidance during the three years of these studies.

Dr. John C. Hill and Dr. James P. Vary for their helpful discussions and comments.

Also, appreciation is expressed to all the people who proofread and catched many spelling mistakes and grammatical errors.

The author acknowledges the support from the Iowa State University, the U.S. Department of Energy under Special Research Grant No. DE-FG02-92ER40692, and the GANN fellowship.

Finally, the author would like to express his thanks to his American family,

the Birks, especially his American mother and best friend, E. Joyce, for their love, support, encouragement, and understanding during these studies.

APPENDIX THE DECAY OF ^{68}Ga

The decay of ^{68}Ga to ^{68}Zn has been studied extensively using NaI and Ge(Li) detectors [76, 77, 78, 79]. This work is the awarded result from the extensive work on the e^+e^- resonances using the positrons from the ^{68}Ga. Six new very weak transitions were observed.

Fig. A.1 shows the decay scheme of ^{68}Ga based on the present work. The thicker arrows represent the newly found transitions. The γ-ray energies were measured using 20 Ge detectors of HERA. The two strongest γ rays, 511.00-keV from e^+e^- annihilations and the known 1077.40-keV from ^{68}Ga decay were used for the energy calibration. The γ-ray energies reported in this work have been corrected for the non-linearities of the analog-to-digital converter. The corrections for the energy calibration were also included assuming the 511.00-keV γ-ray has the unceratainty of zero and the 1077.36-keV transition has the uncertaintie of $\pm$0.05 keV.

An E_γ-E_γ coincidence matrix was constructed to analyze the coincident γ rays. A spectrum of the single data was also made from the chance coincident data (i.e. using the data at the tail of the timing spectrum where no true coincident events are present) for the purpose of analyzing the non-coincident γ rays. The intensities shown in Fig. A.1 were already corrected for the absorption by the lead encapsulating sphere, the detectors' efficiencies, and the internal conversion coefficients. The

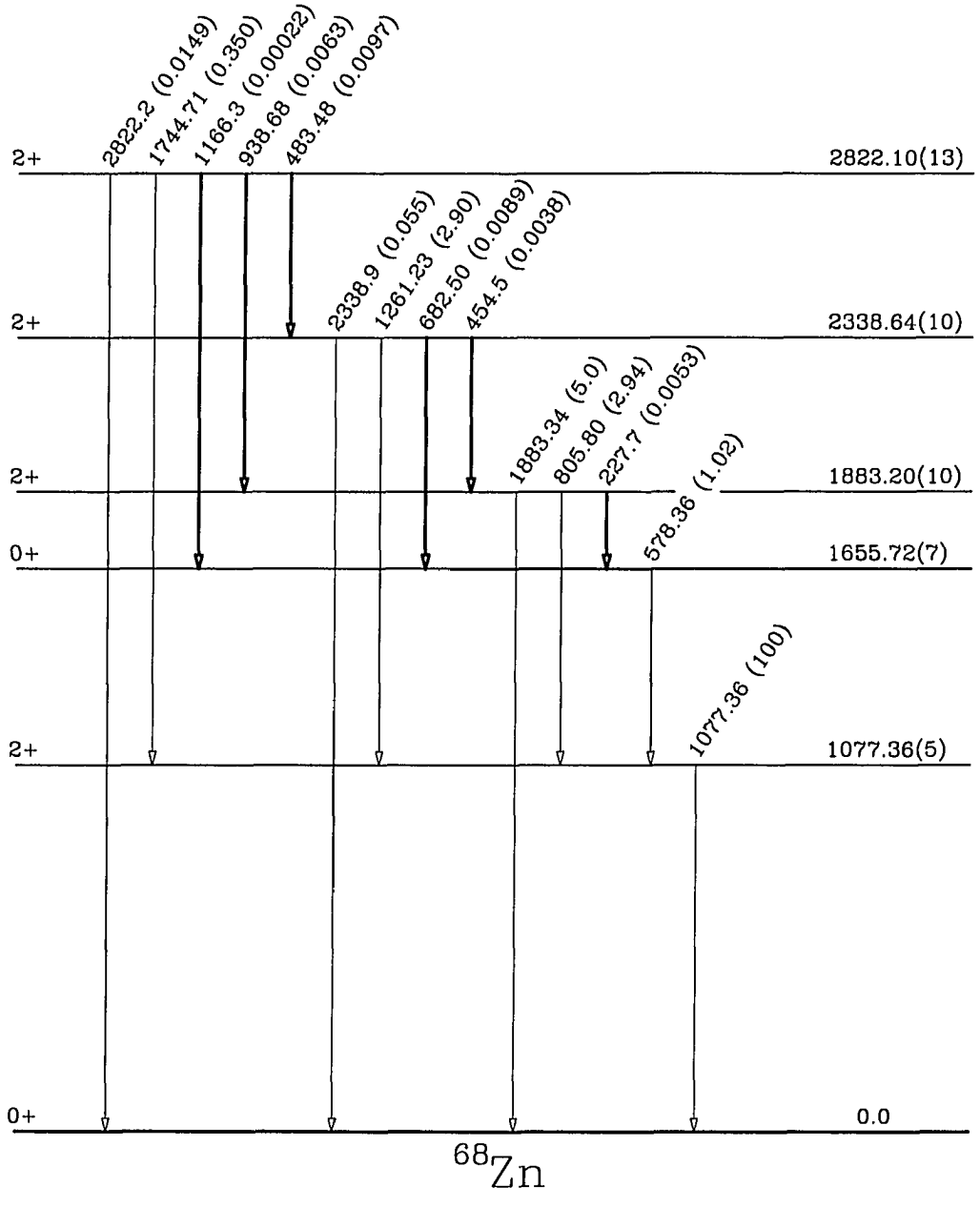

Figure A.1: Decay scheme of ^{68}Ga based on the present work

Table A.1: Energies and relative intensities form the decay of ^{68}Ga. The uncertainties of the least signigicant digits of energies and intensities are indicated in the parentheses

Present work	Relative intensity			
γ-ray energy (keV)	Vaughan *et al* (Ref. [77])	Carter *et al* (Ref. [76])	Lange *et al* (Ref. [79])	Present work
227.7(2)				0.0053(15)
454.5(4)				0.0038(15)
483.48(5)				0.0097(8)
578.36(5)	0.7(1)	1.1(2)	1.00(12)	1.02(5)
682.50(6)				0.0089(7)
805.80(5)	2.2(2)	2.8(2)	2.95(12)	2.94(15)
938.68(9)				0.0063(4)
1077.36(5)	100.	100.	100.	100.
1166.3(6)				0.00022(10)
1261.23(8)	3.1(2)	2.9(2)	3.00(7)	2.90(15)
1744.71(12)	0.5(1)	0.28(4)	0.30(4)	0.35(2)
1883.34(13)	4.8(3)	4.1(4)	4.33(12)	5.0 (3)
2338.9(2)	<0.1	0.04(2)	0.050(6)	0.055(4)
2822.2(3)			0.015(2)	0.0149(12)

relative intensities of the 1883-keV, 2339-keV, and 2822-keV were measured from the singles spectrum. The relative intensities of the 578-keV, 806-keV, 1077-keV, 1261-keV, and 1745-keV transitions were taken from both the coincidence spectra and the the singles spectrum. All other transitions were too weak to be seen in the singles spectrum. There intensities were determined from the double coincidence spectra.

The results of this analysis are summarized in Table A.1. Also given in Table A.1 are the previous results from Refs. [76, 77, 79].

In conclusion, the results of the work have confirmed the earlier works on the decay of ^{68}Ga. It has also added six new transitions to the level scheme. With those six new transitions, all the possible transitions between the energy levels of ^{68}Zn

populated in the ϵ/β^+ decays of ^{68}Ga have been observed.